RESONATOR FOR TIP-WEAR MONITORING ON THE ATOMIC FORCE MICROSCOPE

A Dissertation

Presented to the Faculty of the Graduate School

of Cornell University

In Partial Fulfillment of the Requirements for the Degree of

Doctor of Philosophy

by

Tiffany J. Cheng

May 2014

RESONATOR FOR TIP-WEAR MONITORING ON THE ATOMIC FORCE MICROSCOPE

Tiffany J. Cheng, Ph. D.

Cornell University 2014

This thesis presents a novel RF MEMS resonator composed of an aluminum nitride transducer placed on top of a silicon tip, such as those used for atomic force microscopy (AFM). The objective is to be able to sense tip wear as manifested as small dimensional changes at the tip apex. This thesis demonstrates proof-of-concept: frequency shifts in response to blunting of the tip at 6.39GHz. Furthermore, operation of the resonator up to 20GHz is shown, demonstrating the ability to resolve tip wear on the scale of nanometers.

This AFM resonator was designed with the intention of providing inline characterization of tip wear for use in the atomic force microscope, as well as other scanning probe microscopes. Such a real-time monitoring tool would potentially increase throughput of nanoscale measurements, which is invaluable both for the microtechnology industry as well as scientific research.

The AFM resonator has potential impact beyond increasing throughput of current metrology tools. One area of nanofabrication research focuses on using functionalized AFM probes to create nanostructres. Exact control over the tip dimensions is crucial for maintaining control over the growth of the nanostructure. Beyond application as a sensor, the AFM resonator can also be used to create a high frequency point source of acoustic energy.

BIOGRAPHICAL SKETCH

Tiffany Cheng was born on November 7, 1985 to I-Chung and Peggy Cheng in San Diego, CA. Tiffany graduated from San Marcos High School in San Marcos, CA in 2003. She obtained her Bachelor of Science degree in Electrical Engineering and Computer Sciences from the University of California, Berkeley in 2007. In August 2007, she joined the Ph.D program at Cornell University, working in the OxideMEMS group under the supervision of Professor Sunil Bhave. She worked on RF MEMS resonators, in particular piezoelectric transducers and sensors. Tiffany received her Doctor of Philosophy in Electrical and Computer Engineering in May 2014. She is currently an integration engineer at Avago Technologies in Fort Collins, CO, working on FBAR development.

To my family

ACKNOWLEDGMENTS

I am indebted to Professor Sunil Bhave, who has been an inspirational mentor and advisor. From having an infinite number of creative ideas to providing all the resources a graduate student could need, Sunil has been a wonderful advisor who truly cares about his students' professional and personal well-being. I have learned immensely not only from his technical knowledge, but also from his optimism and drive.

I am very grateful to Professor Chung Hoon Lee of Marquette University, who handled part of the AFM resonator fabrication and with whom I worked closely on developing the process. Professor Lee has been great resource for technical ideas and innovative engineering solutions. I am grateful for the many discussions we had about the device and his endless patience with my questions and concerns. I also thank his students Jun Hyun Han, Benyamin Daviji, and Michael Ziwiski for their work on the AFM resonator fabrication.

Professor Amit Lal originally came up with the idea of the AFM resonator, and I thank both him and Professor Clif Pollock for their guidance during the Tip-Based Nanofabrication DARPA program.

The staff of CNF, CCMR, and NBTC helped me tremendously. I especially want to thank Vince Genova for teaching me much about dry etch chemistry and characterization through the CNF Fellows program. I want to acknowledge Jon Shu and Steve Kriske for their assistance with various tools in Clark Hall I thank Mick Thomas for his training on the focused ion beam, Brian Bowman for help with evaporation and leak detection, and Noah Clay, Meredith Metzler, and Garry Bordonaro for their help with debugging fabrication issues.

The graduate student life could have been a very lonely and hard one if it had not been for the friends that I made at Cornell. It's been my privilege to work alongside the other members of OxideMEMS, who have been inspiring and supportive colleagues: Dana Weinstein, Hengky Chandrahalim, Eugene Hwang, Suresh Sridaran, Susmita Bhandari, Laura Fegely, Benjamin Tang, David Hutchinson, Siddharth Tallur, Tanay Gosavi, Ajay Bhat, Jon Puder and Matthew Storey. I also thank our sister clan – the SonicMEMS group – for their friendship and help, in

particular Serhan Ardanuc, Abhishek Ramkumar, Janet Shen, Yue Shi, Sarvani Piratla, Steven Tin, Norimasa Yoshimizu, Larry Lu, Kwame Amponsah, Po-Cheng Chen, Manoj Pandey, and Hadi Hosseinzadegan. I especially want to acknowledge Serhan for his invaluable help with the mathematical analysis of the AFM resonator. Outside of MEMS, I want to mention Christine Layton, Laura Bud and Andrei, Robin Elliott, Andrew Miller, Xiao Wang, Bo Xiang, Rasika and Harsha Jinadasa, Wei Min Chan, Elva Cha, and KK Yu. I would not have been able to make it without Leah Elliott, Warshi Dandeniya, Mahesh Kumara, and Meera Iyer, who have been with me through so many of the ups and downs of the last few years.

My deepest gratitude goes to my family: my parents, brother, and sister. I have been the recipient of their love and care all my life, yet I have only just started appreciating how much they have given me. To my Dad: I started on this path because of you. Thank you.

TABLE OF CONTENTS

LIST OF FIGURES

LIST OF TABLES

CHAPTER 1

INTRODUCTION

This thesis presents the AFM resonator: novel device composed of a high frequency piezoelectric transducer fabricated on top of a silicon tip that is similar to tips used in atomic force microscopy (AFM). The AFM resonator was motivated by the idea of providing a real-time, in-line characterization of tip wear at the nanoscale.

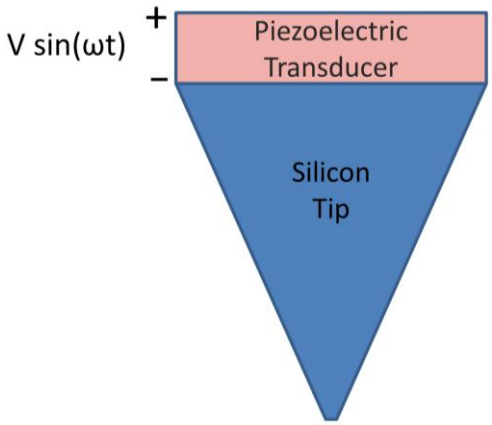

Figure 1-1. Cross-sectional view of AFM resonator

Very sharp tips feature prominently in measurements and manipulation at the nanoscale. AFM is part of the family of scanning probe microscopy (SPM) techniques that operate by raster scanning a sharp tip across a sample surface, achieving spatial resolution down to fractions of a nanometer. With such techniques, a wide range of information can be obtained at the nanoscale, including topography and surface material properties. Depending on the particular SPM technique, the response of the sample to different physical entities – such as indentation (atomic force microscopy), magnetic fields (magnetic force microscopy) and light (near field optical scanning microscopy) - can also be monitored. SPM has also been used to physically manipulate matter from the nanoscale down to individual atoms. Further endeavors into tip-based nanofabrication with precise control over the dimensions and spatial placement of nanostructures are currently being pursued. [1]

For SPM and nanofabrication applications, resolution is directly dependent on the sharpness and shape of the tip apex, with the limiting factor being the area of the probe tip-sample interaction. However, depending on its use, the tip can become worn down over time.

The AFM is generally operated in one of three modes: non-contact mode, contact mode, and tapping mode. In contact mode, the tip is dragged across the surface, with topography measured directly from deflections of the cantilever. Tapping-mode AFM is one of the most commonly used operation modes, and overcomes the problem of stiction of the tip to the sample surface in non-contact mode by tapping the sample intermittently. In both contact-mode and tapping-mode AFM, the tip inevitably becomes worn down over time due to repeated contact with the sample, and eventually the tip becomes unusable due to the loss of resolution. Current methods of characterizing tip shape include running the tip over a separate test structure. [2][3] Another method employed is 3D STM imaging of the tip. [4] Both methods have high accuracy, but are time-consuming. Such methods also do not scale well to large arrays of tips such as the IBM millipede, an extremely dense data storage system that uses an array of thousands of AFM probes to read, write, and erase data encoded in nanoscopic pits.

The AFM resonator provides for in-line, in-situ characterization of tip wear that is more efficient than current methods. A sinusoidal voltage is applied across the transducer, and at appropriate frequencies, the entire tip structure is excited at resonance. At high enough frequencies, nanometer changes at the tip end can be sensed through shifts in the resonant frequency.

Similar devices at 144MHz and 135MHz have been studied for the purposes of near field acoustic microscopy. [5] [6] The device in [6] is largely hand-assembled, with a bulk zinc oxide slab glued to one side of a glass carrier that was bonded to a silicon wafer containing the tip. This particular structure is not workable for the applications this thesis seeks to address. Bulk piezoelectric slabs are limited to frequencies that are far below what is required to resolve nanometer changes in the tip. Furthermore, the presence of a thick intermediate glass layer

between the tip and the zinc oxide introduces significant acoustic loss. The AFM resonator draws inspiration from this structure and utilizes microfabrication techniques to fabricate a thin film, high bandwidth aluminum nitride transducer directly on top of a single crystal silicon tip. FBAR resonators have large effective mass, rendering them poor absolute mass sensors. Instead, frequency shifts are measured in the acoustic standing wave that can be sustained inside the AFM tip itself.

The ultimate vision of the AFM system is presented in Figure 1-2. This thesis addresses the initial steps towards the vision by demonstrating fabrication and measurement of a proof-of-concept device (Figure 1-1).

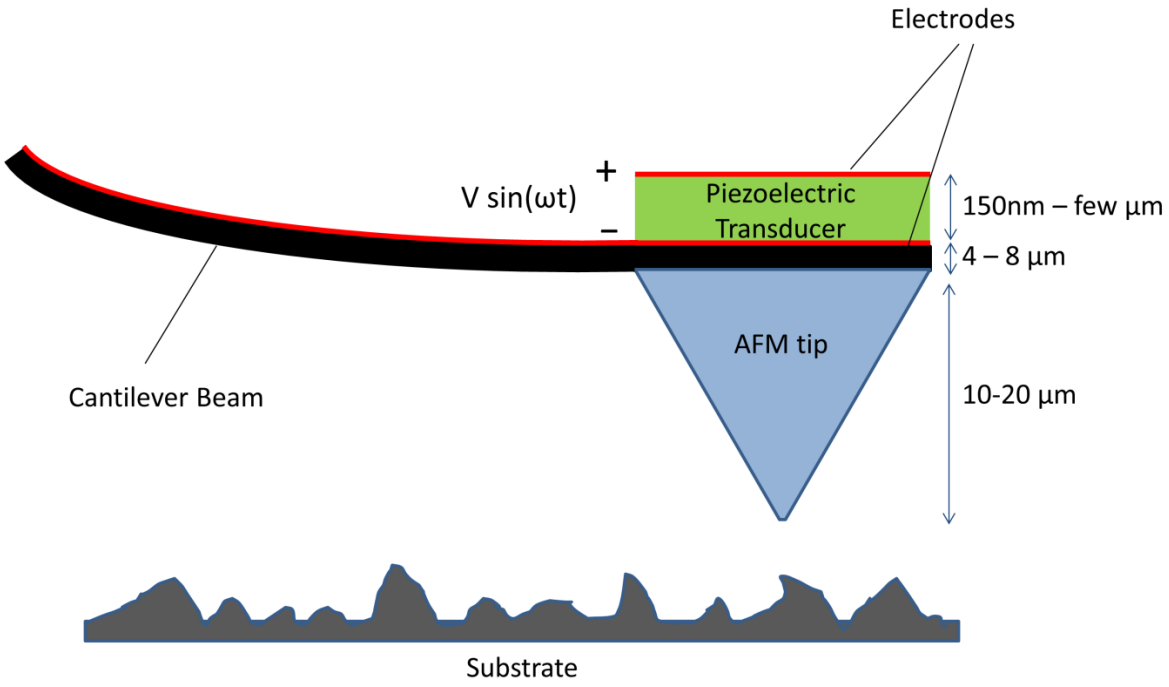

Figure 1-2. Vision of AFM system with integrated AFM resonator.

Chapter 2 describes the operation and design of the AFM resonator. Chapter 3 details the fabrication process for first generation devices and measurement results showing a minus 400kHz frequency shift at 6.4GHz due to blunting of the tip via focused ion beam. Second generation devices with improved process yield are presented in Chapter 4. Whereas first generation device tips were shortened by focused ion beam to simulate tip wear, second

generation device tips were degraded under real AFM tapping-mode conditions. A summary of findings and future directions for the AFM resonator are presented in Chapter 5.

CHAPTER 2

THEORY AND DESIGN OF THE AFM RESONATOR

2.1 Balance Laws and Constitutive Relations

This section provides an overview of the relevant balance laws and constitutive relations upon which subsequent mathematical analysis of tip vibrations is based. For more in-depth treatment of continuum mechanics and vibrational theory, the reader is referred to cited sources.

2.1.1 Notation

Analysis of vibrations in the tip structure requires the use of tensors. In this thesis, Einstein summation notation is used, in which summation over repeated indices is implied as shown in Equation 2.1. Equation 2.2 describes notation for spatial differentiation.

$$a_i b_i \equiv \sum_i^3 a_i b_i \qquad \textit{Equation 2.1}$$

$$\dot{(\,)} \equiv \frac{\partial(\,)}{\partial t} \qquad \textit{Equation 2.2}$$

Quantities in subsequent sections adhere to the following conventions for index notation. Lower-case indices *i,j* run over the integers [1,2,3] and are used to index the three-dimensional spatial components of electric field, electric displacement, and polarization. Upper-case indices *I, J* run over the integers [1,2,3,4,5,6] and are used to index the reduced-notation components of the tensors for stress, strain, and compliance.

List of Mathematical Symbols

- T_{IJ} – Stress coefficients [Pa]
- S_{IJ} – Strain coefficients [unitless]
- C_{IJ} – Compliance matrix [Pa]
- ε_{ij} – Dielectric coefficient [F/m]

e_{ij} – Piezoelectric strain-form coefficients [Coulombs/m^2]

D_i – Electric displacement [Coulombs/m^2]

$\mathcal{E}$ – Electric field [V/m]

ν – Poisson coefficient [unitless]

E – Isotropic Young's modulus [Pa]

ρ – Density [kg/m^3]

G – Isotropic shear modulus [Pa]

ω – Angular frequency [rad/s]

2.1.2 Balance of Linear Momentum

The balance of linear momentum gives the basic equation of motion.

$$\vec{\nabla} \cdot \vec{T} = \rho \ddot{u}_i \qquad \textit{Equation 2.3}$$

where external body forces are assumed to be zero.

2.1.3 Constitutive Relations for Linearly Elastic Continua

The second rank stress *T* and strain *S* tensors are related by the stiffness matric *C* as shown in Equation 2.4, in reduced notation.

$$T_I = C_{IJ} S_J \qquad \textit{Equation 2.4}$$

Equation 2.5 shows the constitutive relations for an isotropic material. [7]

$$\begin{bmatrix} S_1 \\ S_2 \\ S_3 \\ S_4 \\ S_5 \\ S_6 \end{bmatrix} = \begin{bmatrix} 1/E & -\nu/E & -\nu/E & 0 & 0 & 0 \\ -\nu/E & 1/E & -\nu/E & 0 & 0 & 0 \\ -\nu/E & -\nu/E & 1/E & 0 & 0 & 0 \\ 0 & 0 & 0 & 1/G & 0 & 0 \\ 0 & 0 & 0 & 0 & 1/G & 0 \\ 0 & 0 & 0 & 0 & 0 & 1/G \end{bmatrix} \begin{bmatrix} T_1 \\ T_2 \\ T_3 \\ T_4 \\ T_5 \\ T_6 \end{bmatrix} \qquad \textit{Equation 2.5}$$

2.1.4 Piezoelectric Materials and Constitutive Relations

Piezoelectricity is the creation of an internal electric polarization in response to stress. Piezoelectric materials can therefore be used as sensors, where a non-zero stress in the material

gives rise to an electrical signal. The reverse case is also true, in which an electric field applied across the material gives rise to a mechanical stress within the material. Piezoelectric materials can therefore be used as both sensors and actuators.

Constitutive equations for analyzing vibrations and waves in piezoelectric materials are given in Equation 2.6 and Equation 2.7.

$$T_I = \sum_J C_{IJ}^{\mathcal{E}} S_J + \sum_j \mathcal{E}_j e_{jI}^T \qquad \textit{Equation 2.6}$$

$$D_i = \sum_J e_{iJ} S_J + \sum_j \varepsilon_{ij}^S \mathcal{E}_j \qquad \textit{Equation 2.7}$$

The superscript on $C_{IJ}^{\mathcal{E}}$ means that the stiffness constants are to be measured at constant electric field, and the superscript on ε_{ij}^S means that the dielectric permittivity is to be measured at constant strain. Similarly, the piezoelectric coefficients e_{jI}^T are to be measured at constant stress.

2.1.5 Aluminum Nitride

Aluminum nitride (AlN) was chosen to be the piezoelectric material for the transducer. Resonators using AlN films that are strongly oriented along the c-axis can achieve $k_t^2 > 6\%$ and impedances <50Ω [8]. Thin film AlN can be sputter deposited with strong orientation in the (002) direction, which gives rise to a high e_{33} piezoelectric coefficient. Furthermore, AlN has a similar acoustic velocity (~10,500 m/s) to that of silicon (8500 m/s), which is advantageous for acoustic matching between the transducer and the silicon tip.

AlN is a material with hexagonal symmetry. The forms of the piezoelectric and stiffness tensors for hexagonal symmetric materials are shown in Equation 2.8 and Equation 2.9.

$$\begin{bmatrix} T_1 \\ T_2 \\ T_3 \\ T_4 \\ T_5 \\ T_6 \end{bmatrix} = \begin{bmatrix} c_{11} & c_{12} & c_{13} & 0 & 0 & 0 \\ & c_{11} & c_{12} & 0 & 0 & 0 \\ & & c_{33} & 0 & 0 & 0 \\ & & & c_{44} & 0 & 0 \\ & & & & c_{44} & 0 \\ & & & & & \frac{c_{11}-c_{12}}{2} \end{bmatrix} \begin{bmatrix} S_1 \\ S_2 \\ S_3 \\ S_4 \\ S_5 \\ S_6 \end{bmatrix} - \begin{bmatrix} 0 & 0 & e_{31} \\ 0 & 0 & e_{31} \\ 0 & 0 & e_{33} \\ 0 & e_{24} & 0 \\ e_{15} & 0 & 0 \\ 0 & 0 & 0 \end{bmatrix} \begin{bmatrix} \mathcal{E}_1 \\ \mathcal{E}_2 \\ \mathcal{E}_3 \end{bmatrix} \qquad \textit{Equation 2.8}$$

$$\begin{bmatrix} D_1 \\ D_2 \\ D_3 \end{bmatrix} = \begin{bmatrix} 0 & 0 & 0 & 0 & e_{15} & 0 \\ 0 & 0 & 0 & e_{15} & 0 & 0 \\ e_{31} & e_{31} & e_{33} & 0 & 0 & 0 \end{bmatrix} \begin{bmatrix} S_1 \\ S_2 \\ S_3 \\ S_4 \\ S_5 \\ S_6 \end{bmatrix} + \begin{bmatrix} \varepsilon_{11} & 0 & 0 \\ & \varepsilon_{11} & 0 \\ & & \varepsilon_{33} \end{bmatrix} \begin{bmatrix} \mathcal{E}_1 \\ \mathcal{E}_2 \\ \mathcal{E}_3 \end{bmatrix} \qquad \textit{Equation 2.9}$$

2.2 Modeling of Resonators

A resonator can in general be represented as a simple harmonic mass-spring-damper system. For MEMS devices, which convert energy between the electrical and mechanical domains, it is useful to represent their mechanical motion with lumped electrical parameters. The Butterworth van Dyke (BVD) model (Figure 2-1b) gives the equivalent electrical model of a mechanical resonator at one specific resonance; mechanical quantities map to electrical parameters as given in Table 2-1.

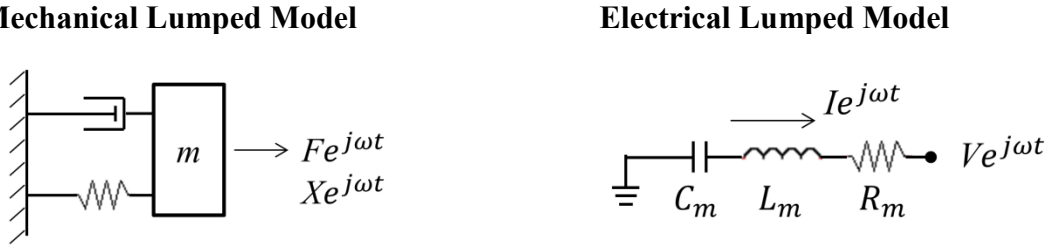

Figure 2-1. Mass-spring-damper mechanical model of a resonator (left). The equivalent lumped electrical parameter model of a resonator (right).

Table 2-1. Mapping Between Mechanical and Electrical Representations of a Resonator

Mechanical Domain	Electrical Domain
Mass m	Inductance $L_m = \frac{m}{\beta^2}$
Compliance $1/k$	Capacitance $C_m = \frac{\beta^2}{k}$
Damping b	Resistance $R_m = \frac{b}{\beta^2}$
Force F	Voltage V
Velocity $\dot{u}$	Current I
Resonant frequency $\omega = \sqrt{\frac{k}{m}}$	Resonant frequency $\omega = \sqrt{\frac{1}{L_m C_m}}$

The damping coefficient b is an aggregate representation of all viscous losses in the resonator. Mechanical parameters *m, k,* and *b* are related to their electrical analogues by the electromechanical transduction factor β, defined as

$$\beta \triangleq \frac{F}{V} = \frac{I}{\dot{u}} \qquad \textit{Equation 2.10}$$

2.2.1 Piezoelectric Transduction

The equivalent one-port electrical model of a piezoelectric bar resonator electrically excited across its thickness is shown in Figure 2-2, where C_0 is the static capacitance of the piezoelectric slab.

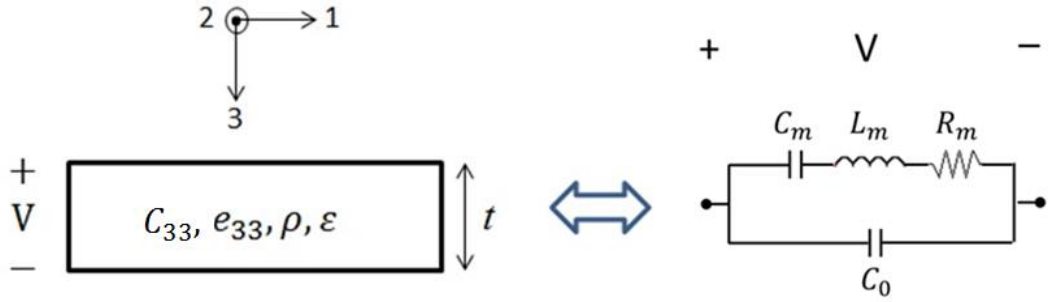

Figure 2-2. Cross-section of a piezoelectric resonator (left) and its equivalent electrical circuit (right).

Two resonances exist for the circuit in Figure 2-2. At the series resonance ω_s, L_m and C_m cancel each other out and admittance is maximum. At the parallel resonance ω_p, energy swaps between the C_0 and the RLC circuit branch, and admittance is at its minimum. Given C_0, ω_s and ω_p, C_m can be extracted by the relationship given in Equation 2.12.

$$\omega_s = \frac{1}{L_m C_m} = \frac{\pi}{t}\sqrt{\frac{C_{33}}{\rho}} \qquad \textit{Equation 2.11}$$

$$\left(\frac{\omega_p}{\omega_s}\right)^2 = \frac{C_m}{C_0} + 1 \qquad \textit{Equation 2.12}$$

For a particular mode of a MEMS resonator, the electromechanical coupling coefficient k_t^2 is a measure of how efficiently energy is transduced between the electrical and mechanical domains. The mode of interest for the AFM tip resonator is the thickness extensional mode, where the electric field is applied across the thickness t and acts upon the e_{33} piezoelectric component. The electromechanical coefficient for the thickness extensional mode is given by

$$k_t^2 = \frac{\pi^2}{8}\frac{C_m}{C_0} = \frac{e_{33}^2}{\varepsilon_{33}\mathcal{E}} \qquad \textit{Equation 2.13}$$

2.3 Theory and Simulation in 1D

This section presents a one-dimensional analysis of a tip structure excited into vibration by a

piezoelectric transducer (Figure 2-3a). All analyses and simulations in this thesis omit the cantilever. Actual fabricated devices also do not have a cantilever, which facilitates demonstration of concept, i.e., the ability to measure dimensional changes at the tip end.

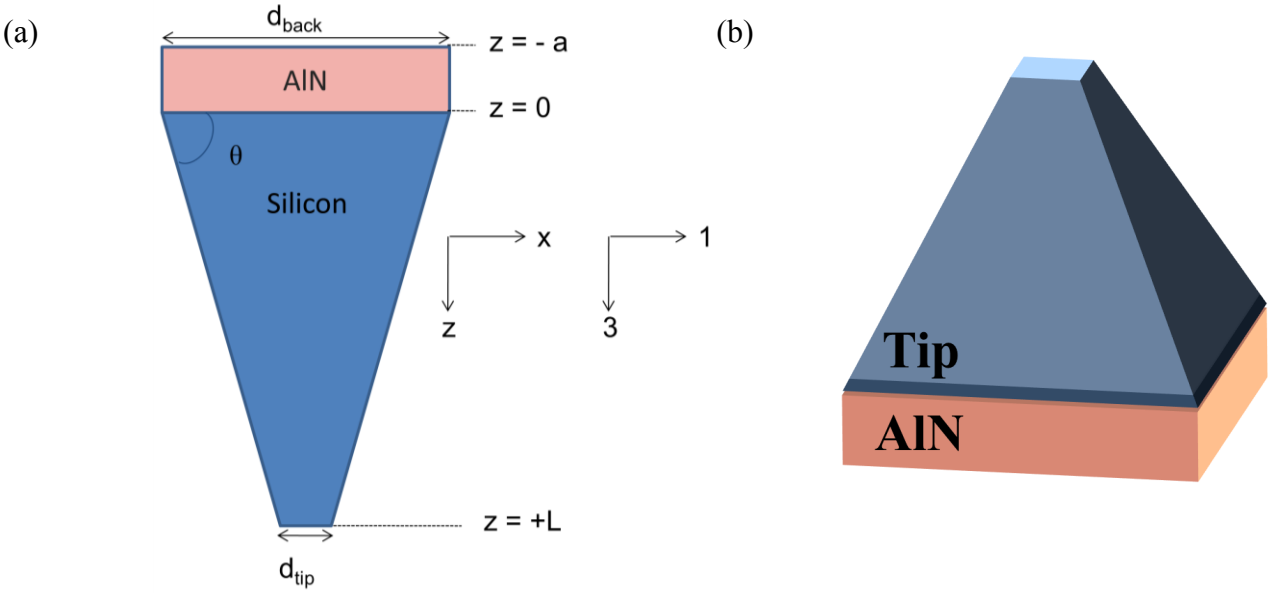

Figure 2-3. (a) Cross-section of the tip structure actuated by a piezoelectric transducer. (b) The tip is assumed to be prismatic, which can be a pyramidal geometry (depicted) as well as conical

2.3.1 Notation

The spatial coordinates x, y, z map to the indices 1, 2, 3 respectively for quantities in the following analysis. Subscripts *p* and *t* refer to quantities for the piezoelectric transducer and the tip, respectively.

Definitions of mathematical symbols and notation in Sections 2.1 and 2.2 are retained in this section. Below are the definitions of additional symbols used in the subsequent analysis.

η	damping factor [kg/(m^{2}s)]
ζ	damping ratio [unitless]
u_z	z-displacement [m]
Q	quality factor [unitless]

2.3.2 1D Analysis of AFM Resonator

The tip material is assumed to be isotropic silicon, and the piezoelectric material is assumed to be AlN. The piezoelectric coefficients for AlN hexagonal symmetric structure are given in Section 2.1.5.

The thickness of the piezoelectric layer is much smaller than its lateral dimensions. From this, the assumption of plane strain in the piezoelectric layer can be made (Equation 2.13). Furthermore, the piezoelectric layer is assumed to be under quasistatic conditions and with zero net free charge (Equation 2.14).

$$S_1 = S_2 = S_4 = S_5 = S_6 = 0\,, \qquad -a < z\ < 0 \qquad \textit{Equation 2.14}$$

$$\nabla \times E = 0\ and\ \nabla \cdot D = 0, \qquad -a < z < 0 \qquad \textit{Equation 2.15}$$

The form of the solutions for z-displacement and electric potential across the transducer are given by Equations 2.15 and 2.16 respectively.

$$u_z = \begin{cases} \psi_p(z)e^{j\omega t}, & z < 0 \\ \psi_t(z)e^{j\omega t}, & z > 0 \end{cases} \qquad \textit{Equation 2.16}$$

$$\phi = V(z)e^{j\omega t}, \qquad z < 0 \qquad \textit{Equation 2.17}$$

For the piezoelectric layer ($z < 0$), the equation of motion is given by

$$\frac{\partial T_3}{\partial z} = \rho_p \frac{\partial^2 u_z}{\partial t^2} \qquad \textit{Equation 2.18}$$

From the constitutive relations for a piezoelectric material (Equation 2.6) and substituting the relation between electric field and potential $\vec{\mathcal{E}} = -\nabla\phi$,

$$T_3 = C_{33,p}^{E} S_3 + e_{33} \frac{d\phi}{dz}\ , \qquad z < 0 \qquad \textit{Equation 2.19}$$

Substituting Equation 2.19 into Equation 2.18, the equation of motion becomes

$$\frac{\partial}{\partial z}\left(C_{33,p}^{E} S_3 + e_{33}\frac{d\phi}{dz}\right) = \rho_p \frac{\partial^2 u_z}{\partial t^2} \qquad \textit{Equation 2.20}$$

From the constitutive relations for a piezoelectric material (Equation 2.7) and the assumption of zero net free charge in the piezoelectric layer,

$$\frac{\partial D_z}{\partial z} = \frac{\partial}{\partial z}(e_{33} S_3) - \varepsilon_{33}^{S}\frac{\partial^2 \phi}{\partial z} = 0 \qquad \textit{Equation 2.21}$$

Using Equation 2.21, Equation 2.20 can be written in terms of the variable u_z only,

$$C_{33,p}^{D}\frac{\partial^2 u_z}{\partial z^2} = \rho_p \frac{\partial^2 u_z}{\partial t^2}, \qquad \text{where} \quad C_{33,p}^{D} = C_{33,p}^{E}\left(1 + \frac{e_{33}^2}{\varepsilon_{33}^{S} C_{33,p}^{E}}\right) \qquad \textit{Equation 2.22}$$

Viscous damping in the structure is treated as a simple resistive force and is denoted by the the variable η, where quality factor Q and damping ratio ζ are related at a given frequency ω by

$$Q = \frac{\rho\omega}{\eta} = \frac{1}{2\zeta} \qquad \textit{Equation 2.23}$$

Including damping, Equation 2.22 becomes

$$C_{33,p}^{D}\frac{\partial^2 u_z}{\partial z^2} - \eta_p \frac{\partial u_z}{\partial t} = \rho_p \frac{\partial^2 u_z}{\partial t^2} \qquad \textit{Equation 2.24}$$

Finally, substituting the full form of $u_z = \psi(z)e^{j\omega t}$ and carrying out the time derivatives, the equation of motion for $z < 0$ is

$$\frac{d^2\psi_p}{dz^2} + \gamma_p^2 \psi_p = 0 \;\; for\; z < 0, \qquad where\;\; \gamma_p = \sqrt{\frac{\omega^2\rho_p + j\omega\eta_p}{C_{33,p}^{D}}} \qquad \textit{Equation 2.25}$$

From Equation 2.21, the electric potential across the transducer is given by

$$\phi = \frac{e_{33}}{\varepsilon_{33}} \frac{d\psi_p}{dz} + B_1 z + B_2, \qquad \textit{Equation 2.26}$$

$$where\ \ B_1\ and\ B_2\ are\ constants$$

For $z > 0$, the tip is treated as a linearly tapered horn [9]. The cross-sectional area $A(z)$ is given by

$$A(z) = A_0 \left[\frac{d_{back}}{d_{tip}} + \frac{z}{L} \left(1 - \frac{d_{back}}{d_{tip}} \right) \right]^P, \ \ where\ A_0 = A(z = 0) \qquad \textit{Equation 2.27}$$

The power $P = 1$ represents a uniform extension of the cross-section into the page, whereas $P = 2$ represents a prismatic or conical three-dimensional shape (Figure 2-3b). The equation of motion of the tip is given by

$$T_3 \frac{dA(z)}{dz} + \frac{\partial T_3}{\partial z} A(z) = \rho_t A(z) \frac{\partial^2 u_z}{\partial t^2} \qquad \textit{Equation 2.28}$$

Expanding $A(z)$ and plugging in $T_3 = E_t \frac{\partial u_z}{\partial z}$, Equation 2.28 becomes

$$\frac{\partial^2 u_z}{\partial \tilde{z}^2} + \frac{P}{\tilde{z}} \frac{\partial u_z}{\partial \tilde{z}} = \frac{\rho_t}{E_t} \frac{\partial^2 u_z}{\partial t^2}, \qquad \textit{Equation 2.29}$$

$$where\ \ \tilde{z} = z - z_0, \ \ z_0 = \frac{d_{back} L}{d_{back} - d_{tip}}$$

Note that the variable z has been transformed to $\tilde{z}$, where $d\tilde{z} = dz$. Following the treatment for the piezoelectric layer, viscous damping is added and the time derivatives are evaluated. The equation of motion then becomes

$$\frac{d^2 \psi_t}{d\tilde{z}^2} + \frac{P}{\tilde{z}} \frac{d\psi_t}{d\tilde{z}} + \gamma_t^2 \psi_t = 0 \quad for\ \tilde{z} > -z_0, \qquad \textit{Equation 2.30}$$

$$where\ \gamma_t = \sqrt{\frac{j\omega\eta_t + \omega^2 \rho_t}{E_t}}$$

Equation 2.31 – 2.25 summarize the boundary conditions on the structure. The piezoelectric

layer is assumed to be air-backed (free surface), whereas the tip of the structure is assumed to be terminated with an acoustic impedance Z_a. Continuity of displacement and stress is assumed at the boundary between the piezoelectric layer and the tip. A voltage V_0 is applied across the transducer, assuming the terminal at $z = 0$ is ground.

$$T_3|_{z=-a} = 0 \qquad \textit{Equation 2.31}$$

$$\frac{stress}{velocity} = \left.\frac{E_t \frac{d\psi_t}{d\tilde{z}}}{-j\omega\psi_t}\right|_{\tilde{z}=L-z_0} = Z_a \qquad \textit{Equation 2.32}$$

$$\psi_p|_{z=0} = \psi_t|_{\tilde{z}=-z_0} \qquad \textit{Equation 2.33}$$

$$T_3|_{z=0} = T_3|_{\tilde{z}=-z_0} \qquad \textit{Equation 2.34}$$

$$\phi|_{z=-a} = V_0 \qquad \textit{Equation 2.35}$$

$$\phi|_{z=0} = 0 \qquad \textit{Equation 2.36}$$

Solutions can be obtained with the system of partial differential equations provided by Equations Equation 2.25, Equation 2.26, and Equation 2.30, and boundary conditions in Equation 2.31 – 2.25.

2.3.3 Solution for Prismatic Tip

This section presents the solution for the P=2 case (Equation 2.27), where the tip is pyramidal or conical.

Solutions to Equation 2.25 and Equation 2.26 have the following forms:

$$\psi_p(z) = C_1 \sin(\gamma_p z) + C_2 \cos(\gamma_p z) \qquad \textit{Equation 2.37}$$

$$\psi_t(\tilde{z}) = \frac{C_3 J_{0.5}(\gamma_t \tilde{z}) + C_4 Y_{0.5}(\gamma_t \tilde{z})}{\sqrt{\tilde{z}}} \qquad \textit{Equation 2.38}$$

C_1 , C_2, C_3, and C_4 are constants. J_n and Y_n are Bessel functions of the first and second kind, respectively, and are of order n. The constants $C_1$to C_4 and $B_1$to B_2 from Equation 2.26 total 6 unknowns. The boundary conditions Equation 2.31 – 2.25 provide 6 equations to solve for all unknowns.

Equation 2.38 and 2.39 give expressions for $B_1$and B_2 as functions of C_1 and C_2.

$$B_1 = -\frac{C_{33,p}^D}{e_{z3}} \gamma_p \left[C_1 \cos(\gamma_p a) + C_2 \sin(\gamma_p a) \right] \qquad \textit{Equation 2.39}$$

$$B_2 = -\frac{e_{33}}{\varepsilon_{33}^S} C_2 \qquad \textit{Equation 2.40}$$

Applying the remaining boundary conditions yields the following system of equations to solve for C_1 to C_4.

$$\Gamma \boldsymbol{C} = \begin{bmatrix} V_0 \\ 0 \\ 0 \\ 0 \end{bmatrix}, \qquad \Gamma = \begin{bmatrix} \Gamma_{11} & \Gamma_{12} & \Gamma_{13} & \Gamma_{14} \\ \Gamma_{21} & \Gamma_{22} & \Gamma_{23} & \Gamma_{24} \\ \Gamma_{31} & \Gamma_{32} & \Gamma_{33} & \Gamma_{34} \\ \Gamma_{41} & \Gamma_{42} & \Gamma_{43} & \Gamma_{44} \end{bmatrix}, \qquad \boldsymbol{C} = \begin{bmatrix} C_1 \\ C_2 \\ C_3 \\ C_4 \end{bmatrix} \qquad \textit{Equation 2.41}$$

$$\Gamma_{13} = \Gamma_{14} = \Gamma_{21} = \Gamma_{41} = \Gamma_{42} = 0$$

$$\Gamma_{11} = -\frac{e_{z3}}{\varepsilon_{33}^S} \sin(\gamma_p a) + \cos(\gamma_p a) \gamma_p a \frac{C_{33}^D}{e_{z3}}$$

$$\Gamma_{12} = \frac{e_{z3}}{\varepsilon_{33}^S} [\cos(\gamma_p a) - 1] + \sin(\gamma_p a) \gamma_p a \frac{C_{33}^D}{e_{z3}}$$

$$\Gamma_{22} = \sqrt{-z_0}$$

$$\Gamma_{23} = J_{0.5}(-\gamma_t z_0)$$

$$\Gamma_{24} = Y_{0.5}(-\gamma_t z_0)$$

$$\Gamma_{31} = \frac{C_{33}^D}{E_t} \gamma_p [1 - \cos(\gamma_p t_p)]$$

$$\Gamma_{32} = -\frac{C_{33}^{D}}{E_t}\gamma_p \sin(\gamma_p t_p)$$

$$\Gamma_{33} = \frac{1}{2\sqrt{-z_0}}\left[\frac{1}{z_0}Y_{0.5}(-\gamma_t z_0) + \gamma_t\left(Y_{-0.5}(\gamma_t z_0) - Y_{1.5}(-\gamma_t z_0)\right)\right]$$

$$\Gamma_{43} = \left(-\frac{1}{z_1} + \frac{2j\omega Z_a}{E_t}\right) J_{0.5}(\gamma_t z_1) + \gamma_t\left(J_{-0.5}(\gamma_t z_1) - J_{1.5}(\gamma_t z_1)\right)$$

$$\Gamma_{44} = \left(-\frac{1}{z_1} + \frac{2j\omega Z_a}{E_t}\right) Y_{0.5}(\gamma_t z_1) + \gamma_t\left(Y_{-0.5}(\gamma_t z_1) - Y_{1.5}(\gamma_t z_1)\right)$$

$where\ z_1 = L - z_0$

Electrical admittance is the measured quantity that will be monitored for spectral changes due to tip wear. Admittance is defined as current out of the device divided by the voltage applied across the transducer. The current across the terminals of the transducer is

$$I = j\omega A_p D_z|_{z=-a} \qquad \textit{Equation 2.42}$$

where A_p is the cross-sectional area of the transducer in the *x-y* plane. Electrical displacement in terms of electric potential and z-displacement is given by

$$D_z = \varepsilon_{33}^{S}\left(-\frac{dV(z)}{dz}e^{-j\omega t} + e_{33}\frac{d\psi_p}{dz}e^{j\omega t}\right) \qquad \textit{Equation 2.43}$$

Electrical admittance is therefore given by

$$Y_p = \frac{I}{V_0 e^{j\omega t}} = -j\omega\frac{\varepsilon_{33}^{S}B_1 A_p}{V_0} \qquad \textit{Equation 2.44}$$

For a given frequency, Equations 2.40 and 2.43 can be solved numerically for displacement and admittance.

The transducer thickness is designed to be at λ/2 of the target operating frequency to obtain maximum transduction at that frequency. AFM tips are typically 10-20μm long. In order to detect nanometer changes at the tip end, the device would necessarily be operating at a high-order harmonic resonance such that multiple wavelengths would reside in the tip. As the tip is

blunted, i.e., the tip length L is shortened, the resonance frequency of one particular harmonic mode shifts upward (Figure 2-4). From a sensor standpoint, the local frequency range about the target resonance is of utmost interest. In Figure 2-4, the n^{th} mode starts at f_0 =21.46GHz. Considering a $\pm$100MHz window around f_0, the resonance frequency as the tip is blunted at first increases and then appears to suddenly decrease at a blunt amount of -λ/2 when the *n-1* mode shifts into the frequency window of interest. Therefore, when monitoring the local region about one resonance, frequency shifts due to blunting of the tip can be positive, negative, or even zero, depending on the blunt amount. This is an important point, given that the measurements of devices were performed in open-loop.

(a)

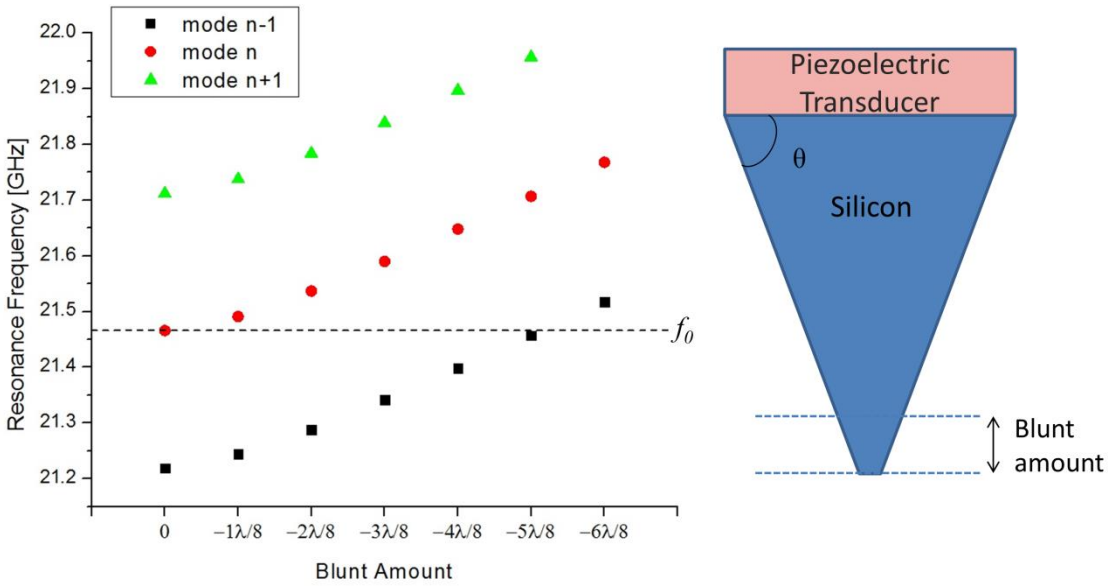

(b)

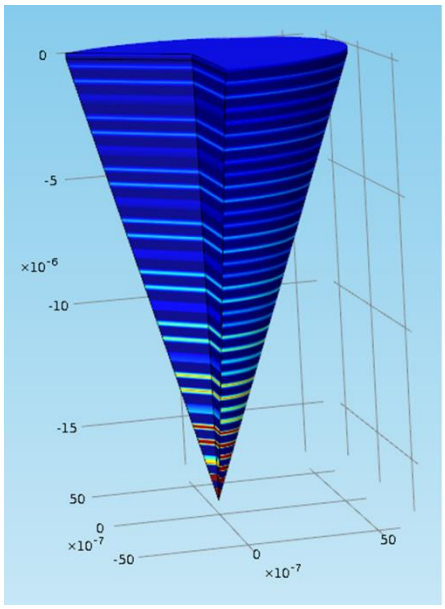

Figure 2-4. Comsol simulation of a resonator assuming 1D motion in z-direction. Tip length is 17μm, transducer thickness is 224nm, and θ is 71°. (a) Frequency progression of modes as tip is blunted in fractions of λ corresponding to f_0. (b) Contour plot of z-displacement for the mode at 21.46GHz

The 1D model lends an intuitive understanding that positive and negative frequency shifts can be observed in response to changes at the tip end. However, the 1D model is inaccurate in predicting the mode shapes and frequencies of the tip structure; motion in the x- and y- directions affect the tip's harmonic response significantly, necessitating a full 3D model to accurately predict the device frequency spectrum. Using finite element software, 2D and 3D simulations with symmetry constraints were performed to get a sense of the sensitivity of the device when accounting for the loading of electrodes, acoustic loss in the material, and misalignment in the actual fabricated structures. However, due to the irregular shape of the actual tip and the fact that every fabricated tip is unique, the simulated and measured frequency responses are different. A full 3D finite element analysis at GHz frequencies requires a prohibitively large number of elements. The accurate prediction of the frequency behavior of these devices was not resolved in this thesis, but is nevertheless something that will need to be addressed for the eventual implementation of this idea.

2.4 Design

For the initial demonstration of concept, the goal was to see a clear, open-loop frequency shift due to blunting of the tip. Therefore, the decision was made to eliminate the cantilever and simply have a membrane between the transducer and the tip (Figure 2-5). With this configuration, RF GSG probes can be directly landed close to the device without having the signal pass through long metal traces along the cantilever. The signal can be calibrated up to the RF probe tips using a standard on-wafer calibration substrate.

The tip material was chosen to be single-crystal silicon, which is commonly used in commercial scanning probe microscopy probes because of its hardness, micro-machinability, and cost-effective production. As described in Section 2.1.5, the transducer piezoelectric material was chosen to be AlN. The tip is formed by wet etching silicon in potassium hydroxide (KOH) solution; the resultant planes of the tip are shown in Figure 2-6. θ of the horizontal cross-section through the tip apex is approximately 76^o. Unless otherwise indicated, θ=76^o is assumed for all 1D simulations. The tip length is fixed by the process to be 15-20μm.

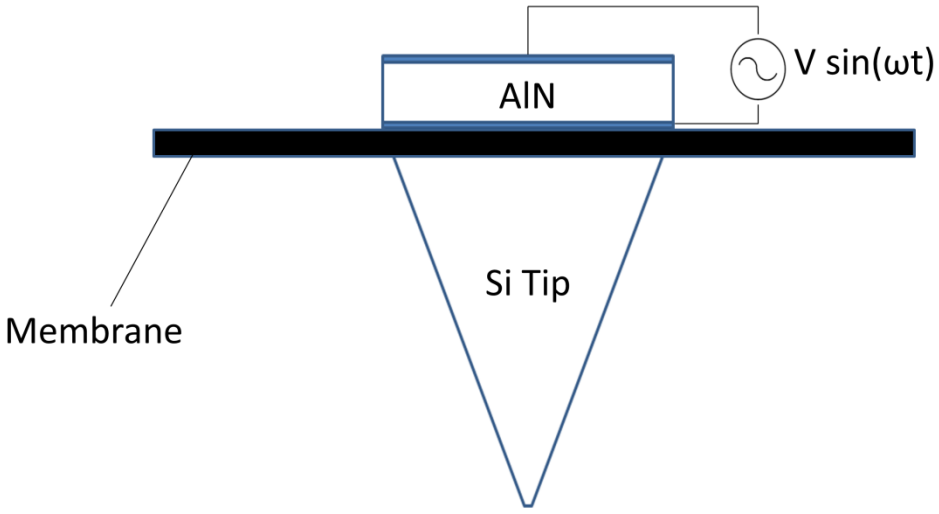

Figure 2-5. Proof-of-concept device with no cantilever

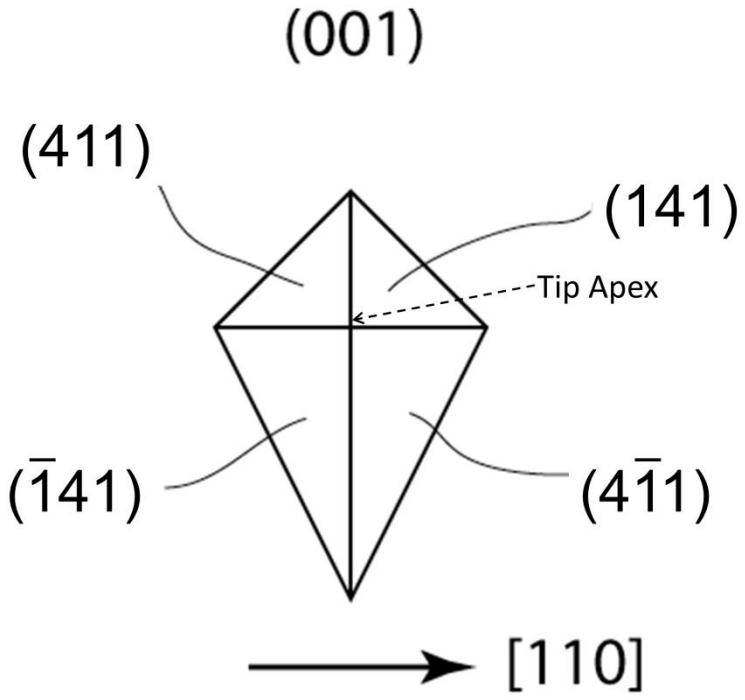

Figure 2-6. Planes of the tip. The [001] plane is out of the page.

The target of the first experiment was to be able to resolve 50nm of change in diameter of the tip end, corresponding to roughly 100nm change in length of the tip. To determine a ballpark operating frequency, 100nm of length change is equated to the blunt amount that elicits the maximum absolute frequency shift in Figure 2-7, i.e., $\lambda_{Si}/4$, where λ_{Si} is the wavelength in silicon. The operating frequency is therefore 21GHz. To get maximum transduction, the piezoelectric layer is designed to be at a thickness of $\lambda_{AlN}/2$, which is 224nm.

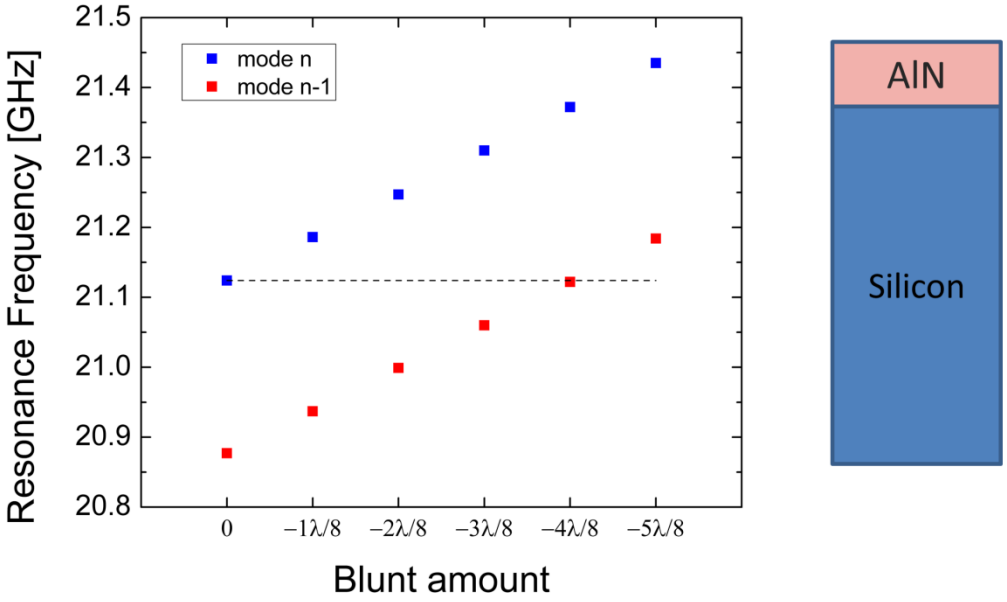

Figure 2-7. Mode progression for a bar resonator

Note that Figure 2-7 is the mode progression for a bar structure rather than a tip. The bar exhibits a perfectly cyclical mode progression, reducing the extraction of operating frequency to a simple calculation for any blunt amount at any frequency. Near the operating frequency, a tip device with same piezoelectric layer thickness has a similar mode progression (Figure 2-4a) to that of the bar structure. Derivation of frequency for the bar structure gives fair accuracy, while being much easier than simulating the tip structure and tracking its mode progression for different blunt amounts.

The effect of damping on resonator sensitivity at 21GHz was investigated using the 1D equations presented Section 2.3. The simulated structure has an AlN thickness of λ_{AlN}=224nm and assumes a tip length of 17µm (Figure 2-8). Damping was implemented by specifying loss factors for the AlN and silicon regions. Loss factors were calculated from measured fQ products of AlN and silicon resonators reported in literature. fQ product – defined as the product of resonance frequency f and quality factor at f – is commonly used as a metric for how well losses in a resonator have been minimized. Theoretical maximum fQ products for a given resonator material and mode have been calculated. [13][14] For the simulation in Figure 2-8,

values that are in the mid- to high range of reported *measured* fQ for AlN and Si resonators were chosen: 2.5 x 10^{11} for AlN [10] [11]; and 5 x 10^{13} for Si [12]. With the assumption that fQ is constant for each material, Q was calculated for the desired operating frequency and loss factor was determined using Equation 2.23. The wideband response (Figure 2-9) shows the highest amplitude occurs around 21GHz, as expected. For Δd_{tip}=50nm and ΔL=100nm, the resolved shift in the 21GHz resonance is 60MHz (Figure 2-10). It should be noted that while constant fQ product has been a common perception [13], it has been demonstrated that the theoretical maximum fQ product may in fact linearly increase with frequency for the frequency range in which the AFM resonator operates [14].

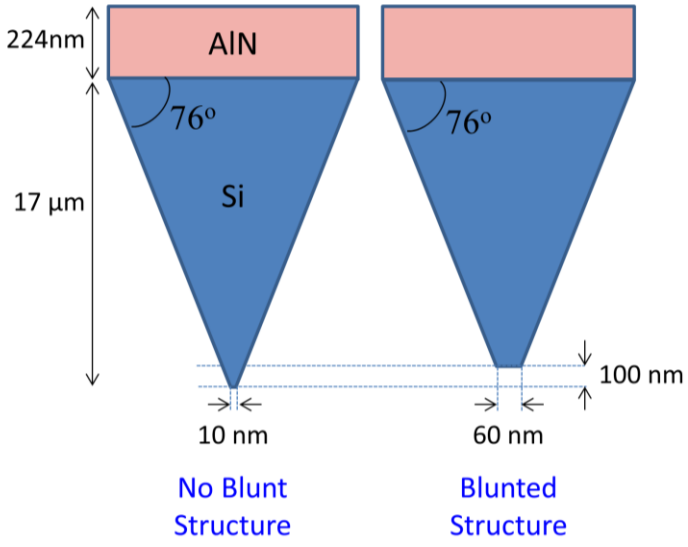

Figure 2-8. Original and blunted structure simulated in Matlab

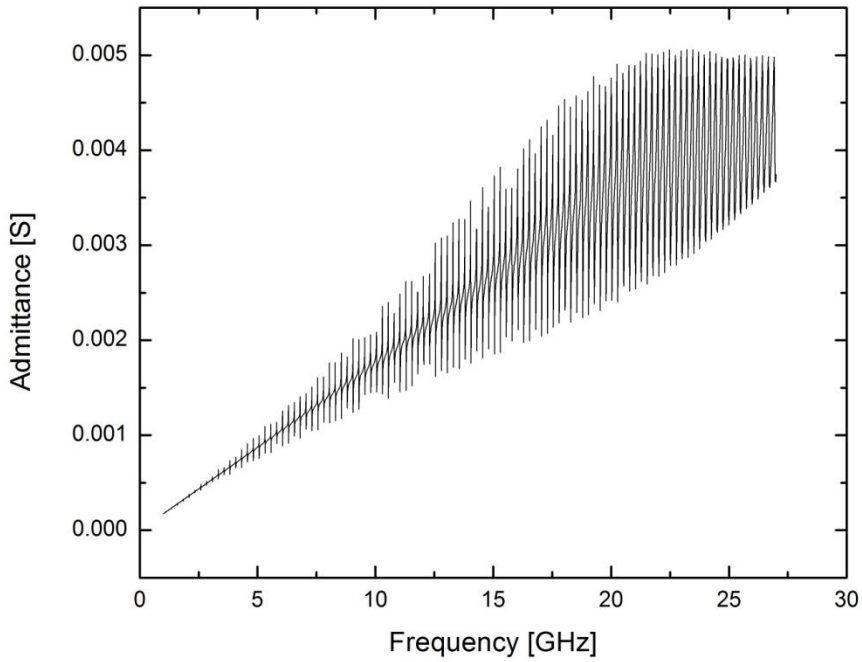

Figure 2-9. 1D simulation of AFM resonator with 21GHz operating frequency: wideband response

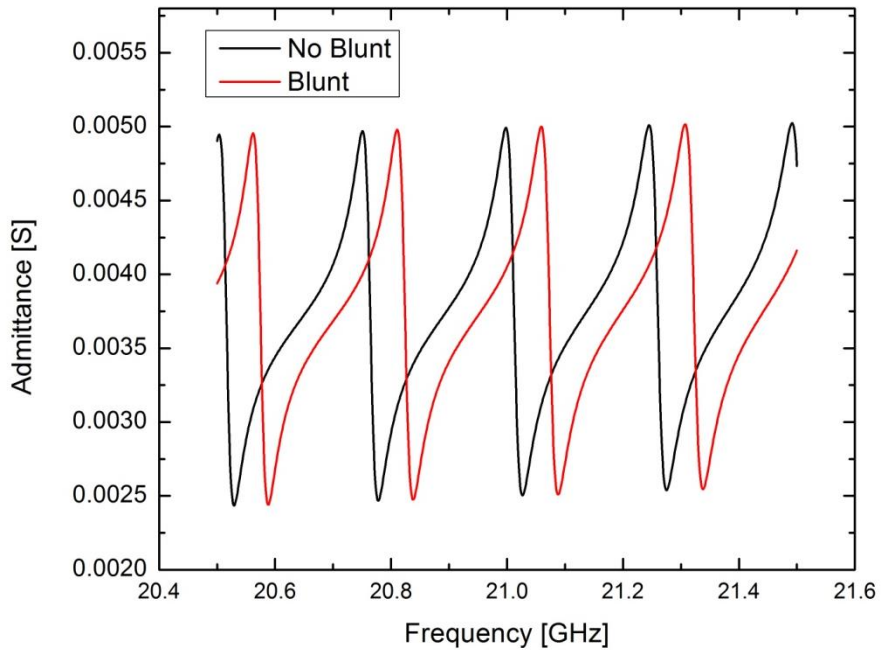

Figure 2-10. 1D simulation of AFM resonator with 21GHz operating frequency: before and after blunting

CHAPTER 3

FIRST GENERATION DEVICES

3.1 Process Flow

Figure 3-1 is the top view layout of the device. Each die and Table 3-1 shows the fabrication process, which is described in more detail in the following sections. All steps were performed with contact lithography. Exact process parameters for each step are given in Appendix A.

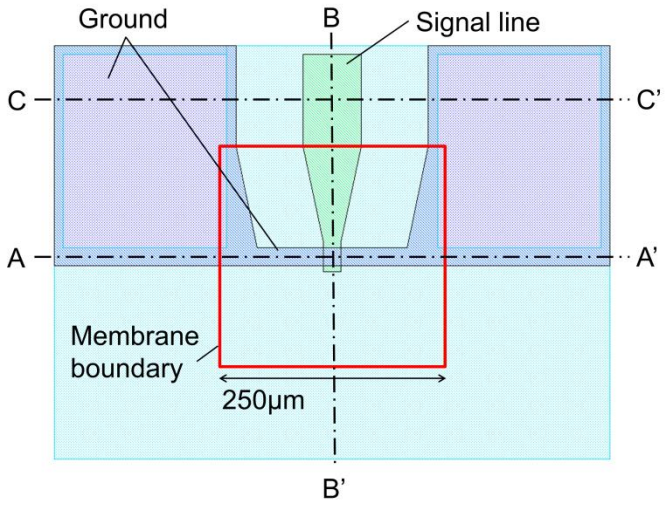

Figure 3-1. Top view of device layout

Table 3-1. Process Flow

Cross-section A-A' (see Figure 3-1) unless otherwise indicated	Si SiO_2 Si_3N_4 Glass Pt AlN Al
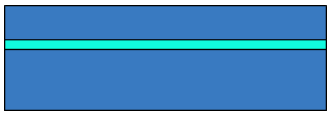	4" SOI wafer. Device layer: 25µm. BOX: 0.5µm Handle: 600µm.
	200nm thermal oxidation
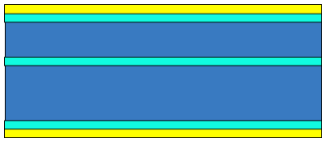	500nm LPCVD low-stress silicon nitride
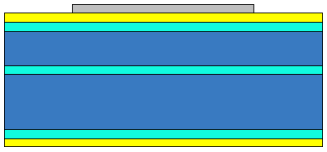	Sputter 25nm/200nm Ti/Pt. Pattern by liftoff.
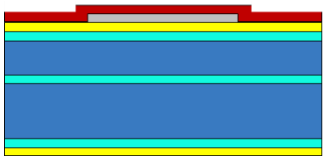	Sputter 224nm of AlN
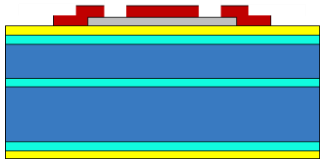	Wet etch AlN in AZ 300MIF
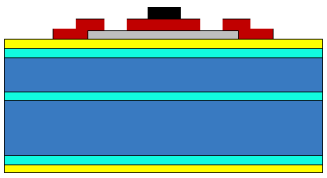	Evaporate 200nm Al. Pattern by liftoff.

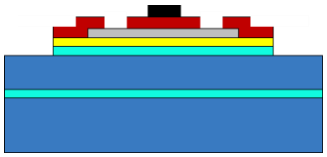	RIE silicon nitride using CHF_3/O_2 Wet etch silicon dioxide in BOE 5:1
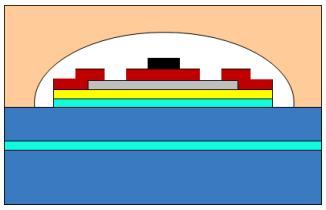	Anodically bond glass carrier wafer
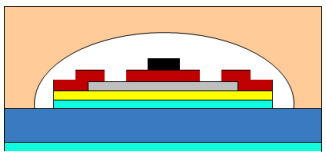	KOH etch SOI handle
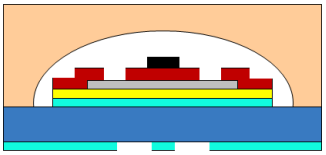	Pattern BOX by wet etching in BOE 5:1
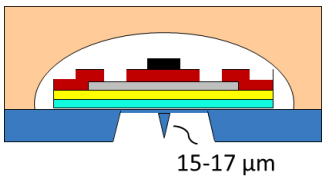	KOH etch tip
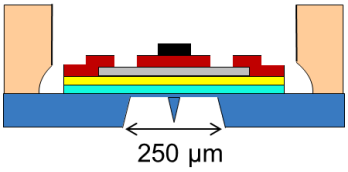 ---------- Cross-section B – B’ 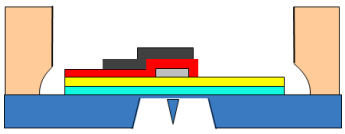	Break glass cavities to access electrodes

3.1.1 Deposit Dielectric

Starting with an SOI wafer, 200nm of thermal oxide is grown followed by 500nm of LPCVD silicon nitride. These layers serve as a chemical etch stop for the KOH etching that comes later. The thicknesses of the nitride and oxide were chosen so that the tensile stress of nitride and the compressive stress of the oxide are balanced out. This becomes important for later in the process, when the entire handle layer is removed. For a wafer with these two layers on one side, the bow is < 1μm. The two dielectrics also provide electrical isolation between the transducer and the silicon, which is slightly doped.

3.1.2 Pattern Ground Electrode

200nm of platinum (Pt) with a 25nm titanium (Ti) adhesion layer is sputtered in a magnetron argon sputtering system. The metal stack is patterned by liftoff to form the bottom electrodes on the device layer of the SOI wafer. From a resonator design perspective, the Pt was patterned to reduce the static capacitance of the device. The platinum has to be well-oriented in the <111> direction to ensure that the aluminum nitride is highly oriented along the c-axis, i.e. a high d_{33} piezoelectric coupling coefficient. The orientation of platinum was determined by measuring its rocking curve using X-ray diffraction. For sputtered platinum, rocking curves were found to be 12-13 degrees. (Figure 3-2) In contrast, the rocking curves were much worse for evaporated platinum. A dummy sample of sputtered platinum was sent to OEM Group for AlN deposition, where the rocking curve of AlN was measured to be 2-4 degrees, indicating a strong c-axis orientation.

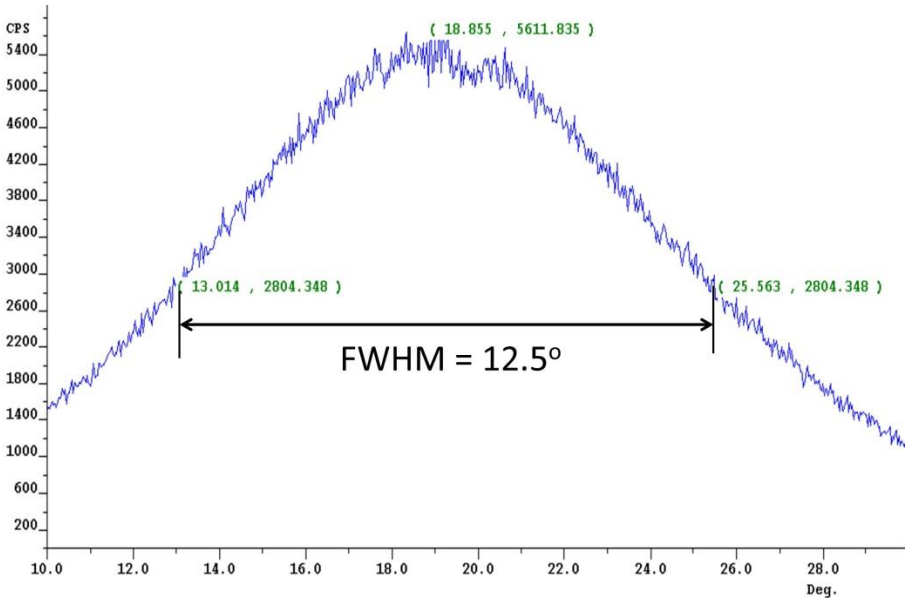

Figure 3-2. Sputtered Pt rocking curve

3.1.3 Deposit and Pattern AlN

Following Pt deposition, 224nm of AlN is deposited in an RF magnetron sputtering tool by OEM Group. AlN is removed from the regions between each die and from the Pt ground electrodes by wet etching in TMAH-containing developer: AZ 300MIF or AZ 726MIF, which is the same as 300MIF except for an additional surfactant. The etch is masked by hard-baked S1818 resist. The approximate etch rate of AlN in either of these solutions is 8nm/min, resulting in a total etch time of 27-30 minutes. At this point, some small hillocks of AlN are still visible in the etched regions of the Pt electrodes. It should be noted that the resist mask starts to erode if the etch is continued for a few minutes beyond 30 minutes. To prevent the AlN from being attacked prior to the etch, a non-TMAH-containing developer was used: Shipley Microposit Developer Concentrate, diluted in water 1:1. Some minimal etching of the AlN does still occur when using this solution. In addition, it was observed that if not mixed well, the developer solution can cause visible roughening of the AlN surface.

3.1.4 Pattern Top Electrode

200nm of aluminum is evaporated and patterned by liftoff to form the top electrode. Negative

resist nLOF2020 was used, which has sloped sidewalls that give reliable liftoff with no fences. Prior to deposition of nLOF2020, XHRi C-16 antireflective coating (ARC) was spun on. The ARC does not dissolve in developer and therefore protects the AlN from the TMAH-containing developer used for nLOF2020. The ARC is later removed in oxygen plasma.

3.1.5 Anodic Bonding of Glass Carrier Wafer

The silicon nitride is removed from the regions between each die by CHF3/O2 RIE, followed by a silicon dioxide etch in BOE 5:1 to expose the silicon surface for the subsequent anodic bonding step. The same steps are repeated for the backside silicon nitride and silicon dioxide to expose the silicon for later KOH etching.

The most challenging part of the process is protecting the AlN during the hours-long KOH etch to remove the SOI handle. The silicon nitride and silicon dioxide layers protect the transducer from below. The transducer-side is protected by a glass wafer that is anodically bonded to the SOI wafer. The glass wafer serves the dual purpose of acting as a KOH etch mask as well as a carrier wafer for the membrane that is left after the SOI handle is removed. 500µm-thick borofloat glass wafers were sent to Alpha Precision, where cavities 400-450µm deep were microdrilled into one side. A KS-7100 dicing saw was used to partially dice 300µm-deep grooves into the glass wafer. The wafer will eventually be broken along these grooves to release individual die in the final step of the process. The glass wafer is cleaned in solvent and then anodically bonded to the transducer-side of the SOI wafer, with the cavities aligned to the dice. Anodic bonding is performed by placing the aligned glass and silicon wafers on an aluminum piece on a hot plate, with a metal probe contacting the top of the glass wafer. 1000V were applied across the wafers via the metal probe, while the hot plate was set at a temperature close to 600ºC.

3.1.6 Etch SOI Handle

The handle of the SOI wafer is removed by wet etching in 30% potassium hydroxide solution (KOH) at 60ºC for roughly 30+ hours. From Figure 3-3, one can see that the edges of the wafer

have been attacked during the KOH etch. Some attack from the sides was expected due to the sides of the silicon being exposed to the KOH. However, the level of attack was much more aggressive than expected, and it suspected that this was due to poor quality of the anodic bond. Openings in between the glass and silicon surface allow the KOH to propagate to other areas of the wafer much faster.

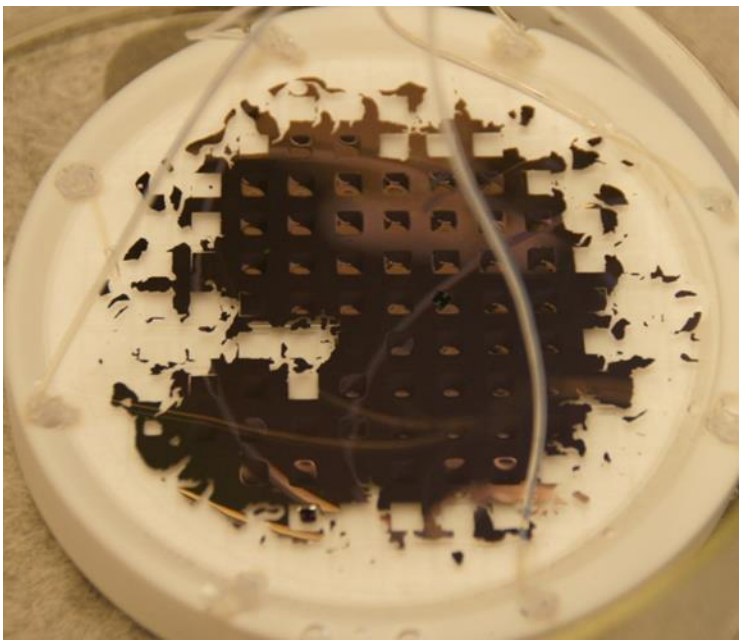

Figure 3-3. Wafer-level view of the tip side after KOH etch of the handle.

3.1.7 Tip Formation

After the SOI handle is removed, the buried oxide layer is patterned by wet etch in BOE 5:1 and then used as an etch mask for the subsequent KOH etch to form the tip in the device layer. The tip is etched in 30% KOH solution at 60ºC for approximately 1 hour, until the silicon dioxide cap pops off. This process yields tips that are 15-17μm tall.

3.1.8 Access Electrodes

After the tip etch, the wafer is broken into individual dice along the dicing grooves of the glass. The transducer-side electrodes are accessed by breaking the glass cavities enclosing each

die by carefully tapping on the glass, yielding the final structure shown in Table 3-1.

Each die was roughly 7mm x 7mm in area and contained one AFM resonator and one reference device located in the center, separated by ~1mm. The area was made large to ensure that angled GSG probes could land without being obstructed by the 500μm-thick glass edge.

3.1.9 Yield and Process Challenges

The final yield was 10 out of 97 devices. The low yield can be attributed mostly to the two KOH etches to remove the handle and form the tip.

As mentioned in Section 3.1.6, the loss of many die after the handle etch is most likely attributed to the poor quality of the anodic bond. Other observations indicate problems with the anodic bond, including the inordinately long time required for the bond to propagate over the entire wafer. Furthermore, the color in certain regions of the wafer was light gray instead of the uniform dark gray that indicates a strong bond. The most likely cause of the poor anodic bond is insufficient cleanliness of the silicon surface. Any particles on the surface will prevent the bond from forming in that localized region. In addition, as mentioned in Section 3.1.3, some hillocks of AlN are left behind after the AlN etch. These hillocks could have masked the silicon nitride and silicon oxide etches, thus leaving an imperfectly clear silicon surface.

Another unexpected process challenge was misalignment of the tip with the transducer. The high temperature at which the anodic bond is performed caused the hollowed cavities to pressurize, causing the die membrane to deform after the handle is removed by KOH. Subsequently, photolithography on the curved membrane surface resulted in slight misalignment of the tip from the metal-AlN-metal stack. (Figure 3-4) In addition, it was determined that systematic alignment error of the contact aligner was also a contributing factor. However, the AlN film still extends over the misaligned tip, and FEM simulation confirms that RF energy still couples into the tip. (Figure 3-12)

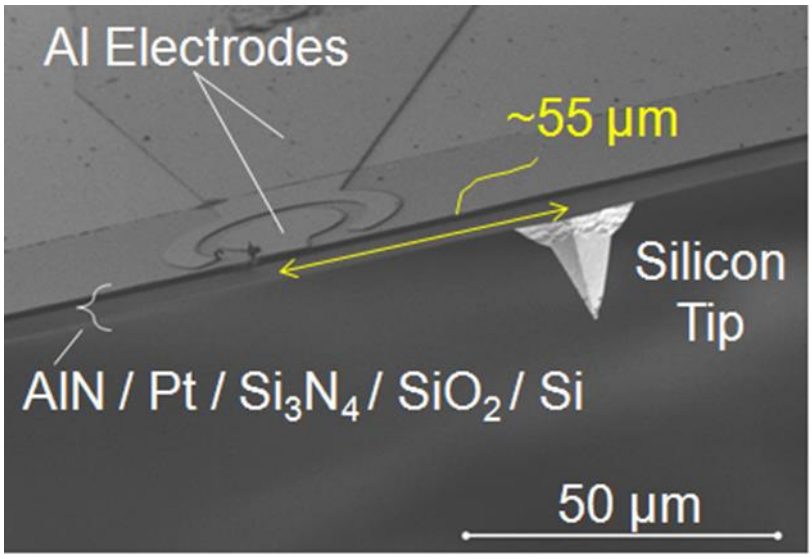

Figure 3-4. Cross-sectional SEM of AFM tip with FBAR fabricated on top

3.2 Experimental Results

The tip was blunted using focused ion beam, which enables precise control over the tip apex removal. The structure was first angled perpendicular to the ion beam, and then tilted θ degrees until the tip end emerged over the surrounding silicon walls (Figure 3-5).

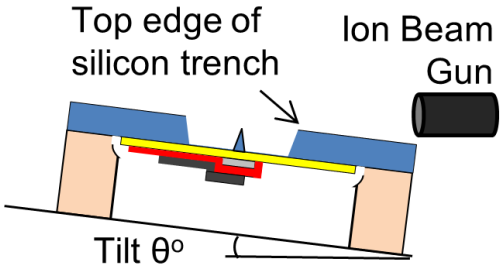

Figure 3-5. Orientation of sample when blunting the tip using focused ion beam.

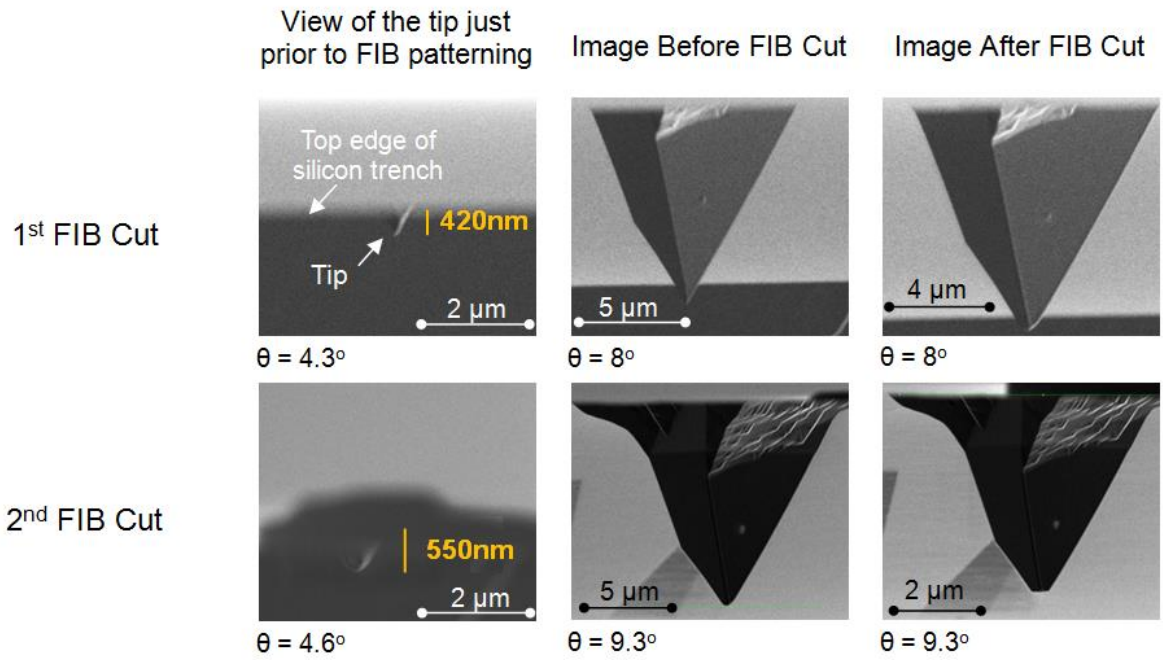

Figure 3-6. Focused ion beam (FIB) images taken of the same tip for 2 cuts.

Figure 3-6 shows SEMs of the tip before and after two FIB cuts. The amount cut off (measured at angle θ) is labeled in the first column of images and is measured from the end of the tip to the top of the silicon trench. The first column shows how FIB patterning took place with the tip end just visible over silicon trench wall. The last two columns show the blunt amount in relation to an expanded vertical view of the tip.

The admittance spectrum was measured in air before and after tip blunting using Cascade Microtech I40 Infinity GSG probes on a Cascade Summit 11K probe station. The resonance spectrum was taken by an Agilent E8364B network analyzer. On-wafer calibration was performed up to the tips of the GSG probes. In the measurement setup, the chips were placed with the tip facing down, while RF probes were landed on top. To protect the tip from hitting the chuck, the die was placed on piece of sticky Gel-Pak with a hole roughly 4mm x 4mm cut out of the center. The die was oriented such that the tip was aligned with the hole in the Gel-Pak.

Figure 3-7 shows the resonance spectrum from 1GHz to 25GHz of a 1-port device. Note that there is a particularly strong peak at 19.9GHz. Due to the difficulty in obtaining a consistent calibration at frequencies above 10GHz, one of the lower frequency peaks at 6.4GHz was chosen

to be analyzed first.

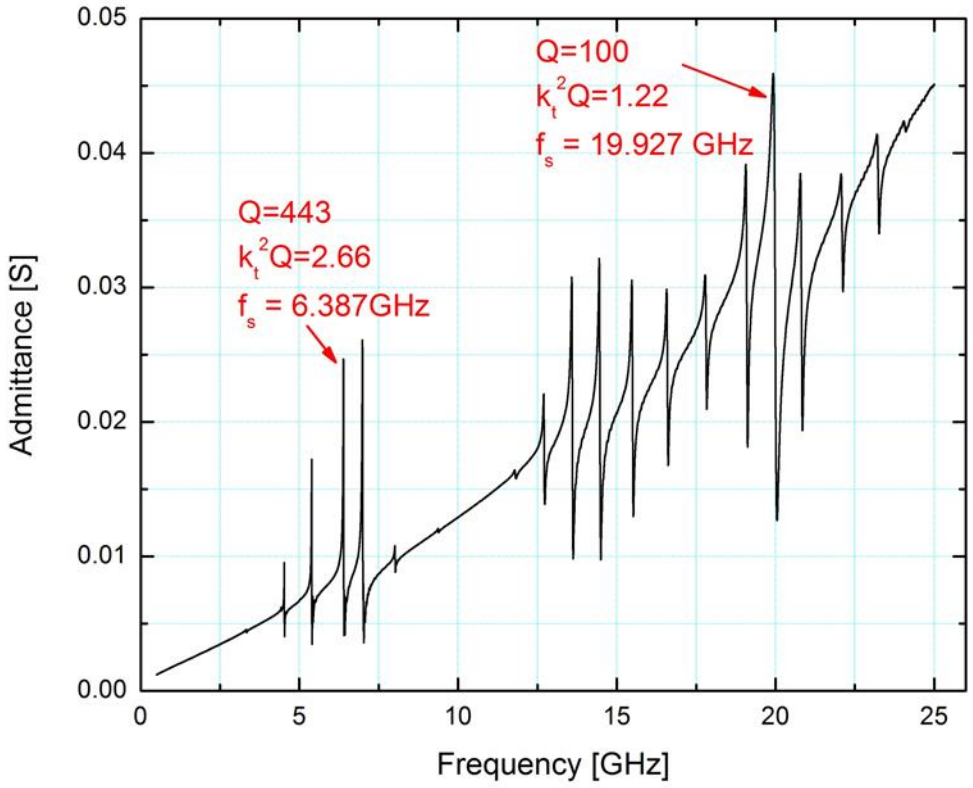

Figure 3-7. Wide sweep frequency measurement of a 1-port device

It is difficult to determine the frequency shift directly from the admittance plots because the change is very small. As shown in Figure 3-9, the difference in amplitude of the peaks before and after blunting further complicates determination of the frequency shift. Moreover, the relatively low k_t^2 results in some frequency pulling of the series resonance peak, which may cause the actual resonance to be slightly off of the very peak of the admittance curve. Therefore, the resonance frequency was more accurately determined by fitting the entire admittance curve to the BVD model (Figure 3-8 and Section 2.2.1). Ballpark values for the BVD model were first determined as follows: C_0 was calculated from the thickness and area of the transducer; C_x was determined from the separation of the series and parallel resonances, corresponding to the maximum and minimum of the admittance, respectively; and L_x was calculated from the series resonance frequency and from C_x. For each curve, C_0 was then tuned to fit the capacitive floor

of the curve; this accounts for parasitic capacitances and results in a more accurate value of C_x. BVD values were further tuned until the fit to the topmost 20% of the series resonance curve had a residual error of <5%.

Several precautions were taken to eliminate other factors that could cause a resonance frequency shift. RF calibration on the network analyzer is generally considered stable for a few hours before it begins to drift. Therefore, before and after FIB measurements all were taken within a 2-3 hour time span. To account for drift of the device over time, measurements were taken on a reference device at the same time as the device being blunted. The reference device is an FBAR with no tip and is physically located next to the device being blunted. Both devices experience the same environmental conditions, with the exception of tip blunting. During measurement, stress may be induced in the edge-supported 25μm-thick membrane from landing RF probes. To minimize large variations in this stress, care was taken to land the probes in the same location before and after tip blunting. Furthermore, several measurements were taken on the same device each time the tip was blunted. The mean of the extracted resonance frequencies was used to determine frequency shifts due to the tip blunting.

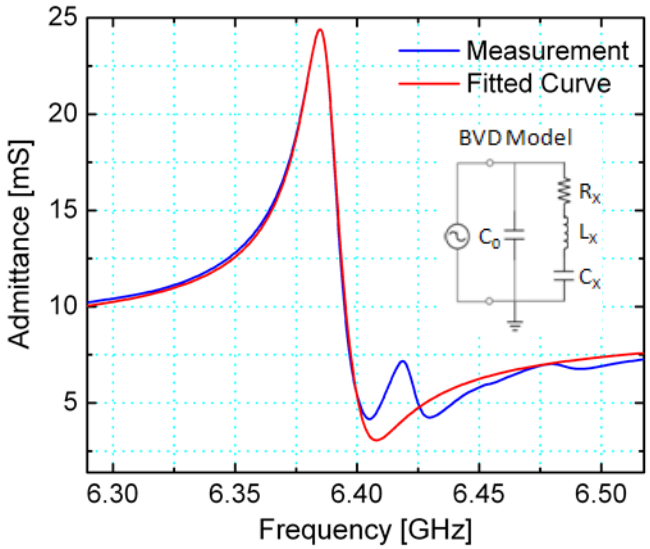

Figure 3-8. Resonance response taken on the device before any blunting. At 6.39GHz, the extracted coupling coefficient kt^2 is 0.6% and quality factor is 443.

Table 3-1 details the resonance frequency progression of the 1-port device in Figure 3-6 and a reference device. Measurements were taken before any cut and after the second cut. (Figure 3-9. Comparison of admittance measurements taken before and after blunting for the device (a) and reference (b). Plots are zoomed to the very apex of the resonance peak.) The blunt amounts in Table 3-2 have been corrected for the angle at which they were measured. After subtracting the frequency shift of the reference device, the net frequency change experienced by the blunted device after blunting 0.98 μm is – 439,141 Hz at 6.387 GHz. The negative sign of the frequency shift is consistent with the theory presented in Figure 1. Assuming a Young's modulus of silicon to be 170GPa and the density to be 2.33 g/cm^3, the wavelength in silicon at 6.387GHz is 1.34μm. The total blunt of 0.98μm shortens the tip by 0.73λ.

(a)

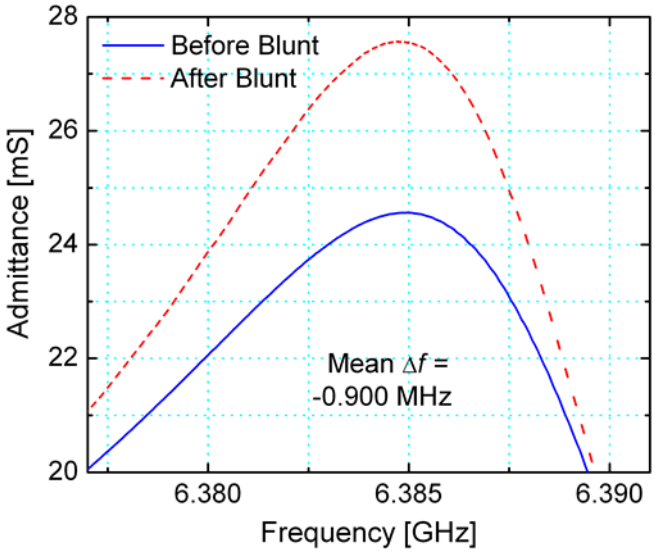

(b)

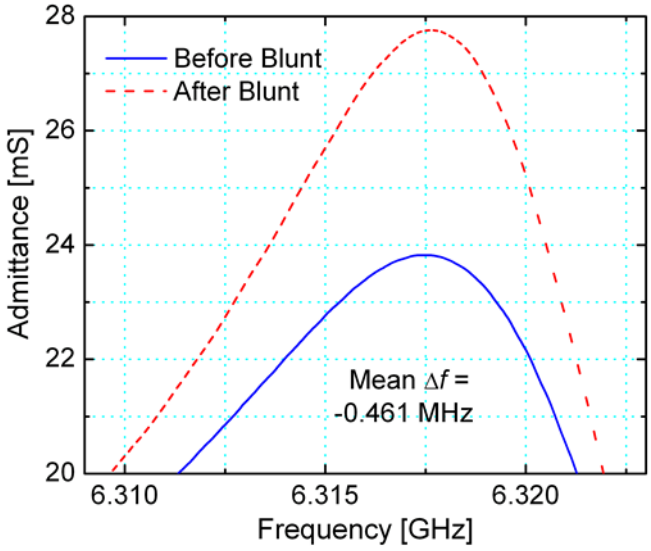

Figure 3-9. Comparison of admittance measurements taken before and after blunting for the device (a) and reference (b). Plots are zoomed to the very apex of the resonance peak.

(a)

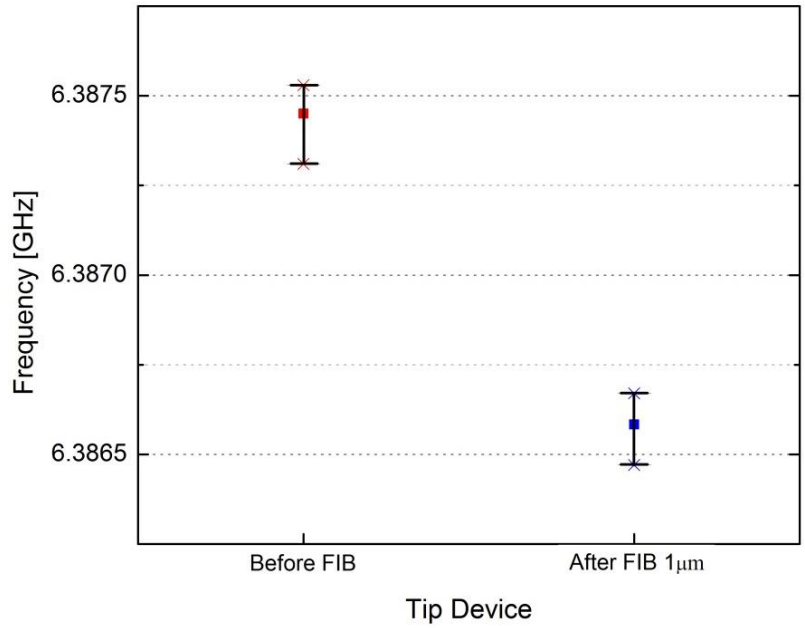

(b)

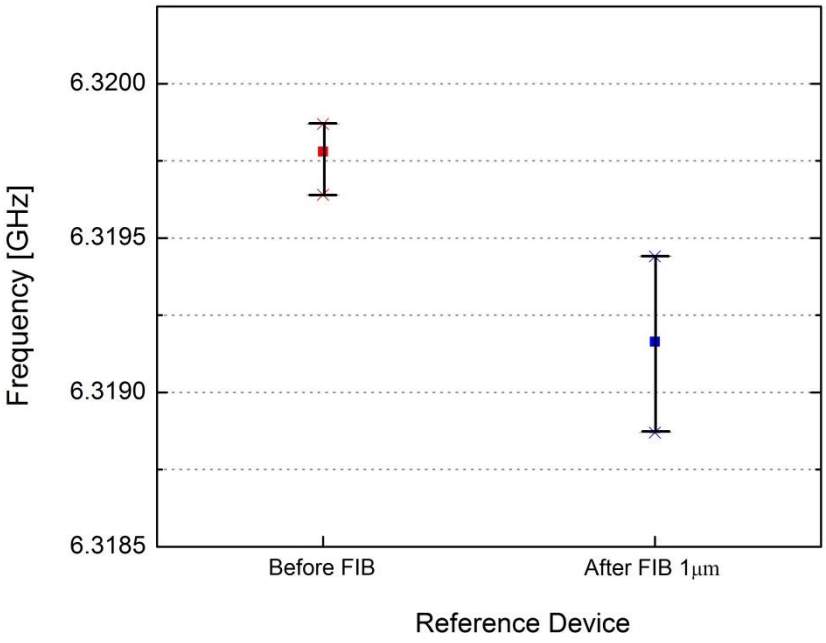

Figure 3-10. Spread of measurements, with the mean indicated by squares, for the tip device (a) and reference (b)

Table 3-2. Extracted Resonance Frequencies

Tip Blunting	**Blunted Tip Device**		**Reference Device**	
	Mean Resonance Frequency (GHz)	# of Data Points	Mean Resonance Frequency (GHz)	# of Data Points
0 μm	6.38745	6	6.31978	3
0.98 μm	6.38655	5	6.31932	5

Several measurement challenges arose from the fact that most of the die is suspended in air. RF probes had to be landed gently to ensure that the 25μm membrane would not break. In fact, several devices did break from landing probes with too much pressure. The limitation on sliding the RF probes forward meant that good contact was often not achieved, and probes had to be landed several times. The capacitive floor of the measurement was monitored to ensure consistent contact. Devices where the probes had to land directly on the thin membrane with the tip were extremely difficult to measure due their even more fragile structure. For this reason, a solid support was placed underneath the probe pads, which is covered in the Section 3.4.

3.3 Simulation of Device

Comsol simulation of the misaligned tip to transducer structure was performed. Half of the 250μm membrane was simulated, with a symmetry boundary condition placed in the center. (Figure 3-11) The simplified structure includes the AlN layer, the silicon tip, and the Pt layer from the electrode to the tip. The Pt layer was included while neglecting silicon nitride and silicon dioxide layers because the dense metal provides the most significant contribution to mass loading. The simulation shows that there exist resonant modes at which there is acoustic coupling into the tip, such as one mode at 6.5GHz, where the tip apex is clearly moving. (Figure 3-12)

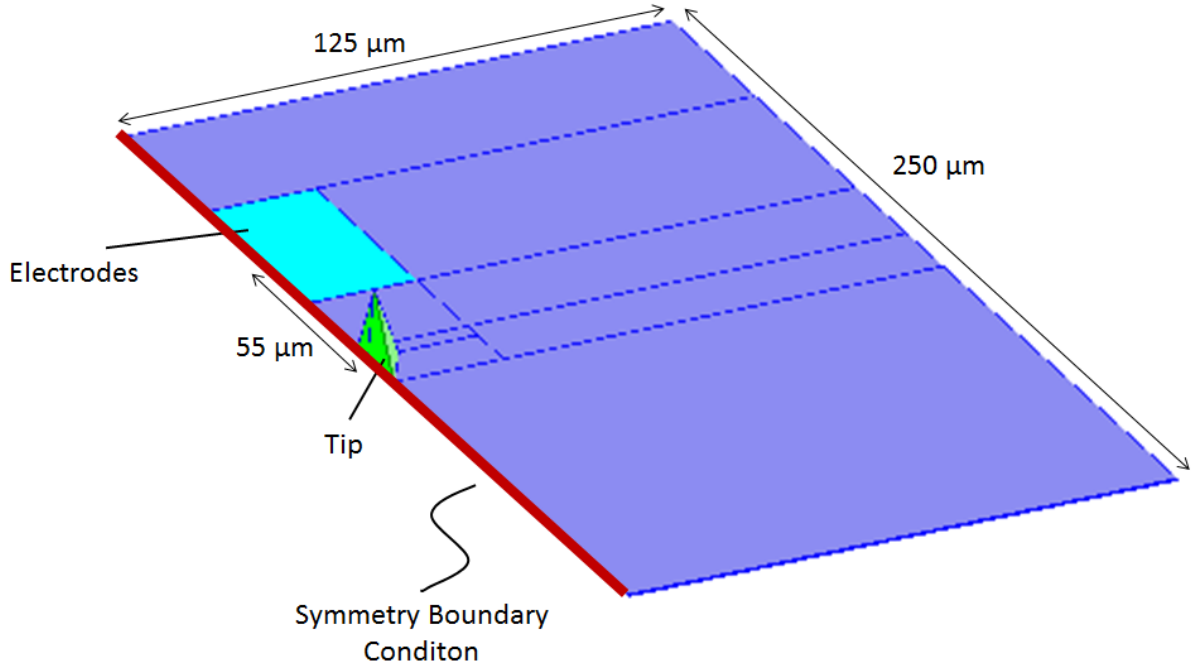

Figure 3-11. Structure used for 3D Comsol simulation of the tip misaligned 55µm from the transducer

a)

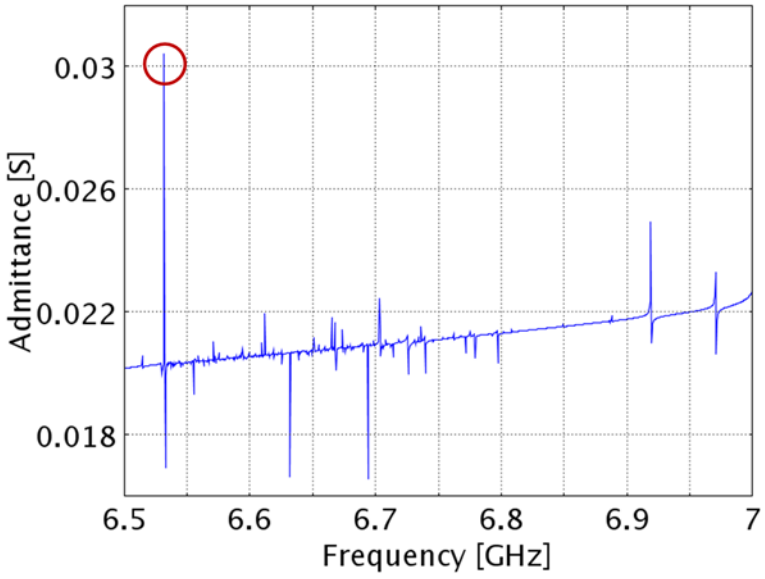

(b)

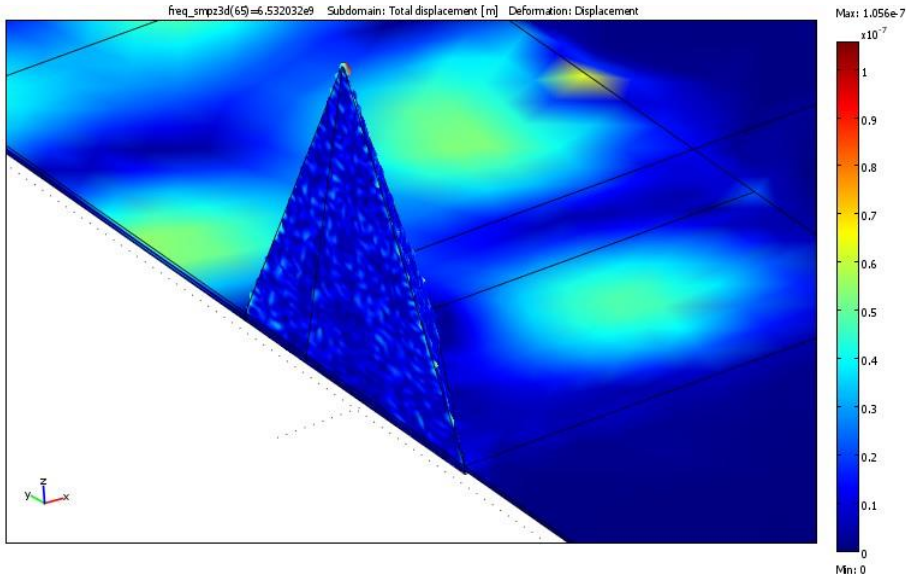

Figure 3-12. 3D Comsol simulation of misaligned tip and transducer. The circled resonance peak at 6.5GHz (a) corresponds to a mode in which acoustic energy is coupled into the tip (b), where the color bar represents total displacement: red corresponds to maximum displacement and blue corresponds to minimal displacement.

3.4 Bonding Membrane Support

As mentioned in Section 3.2, the goal for bonding a support to the die is to provide a solid surface for the landing of RF probes.

3.4.1 Process Flow for Support

The support is fabricated out of a 500µm thick silicon wafer. 500nm of silicon nitride is deposited by LPCVD as a mask for the silicon etch. Silicon nitride on one side of the wafer is patterned by RIE. The silicon is then etched through the wafer in KOH (30% at 60ºC). The wafer is finally diced into supports for individual die.

3.4.2 Bonding of Die and Support

The support is placed on top of the tip-side of die. The die is placed on a Gel-Pak to cushion the glass side of the die and prevent the die from breaking when the support and die are clamped together. (Figure 3-10) Openings in the support are aligned to the tip by using a probe tip

mounted to a micromanipulator. The support and die are then clamped down to minimize spacing between the two. Epoxy (Miller-Stephenson Epoxy 907 Adhesive System) was then applied to the sides of the die and left to sit at room temperature for at least 12 hours. At this point, the device can be removed from the clamps; full curing of the epoxy occurs after 24 hours at room temperature.

(a)

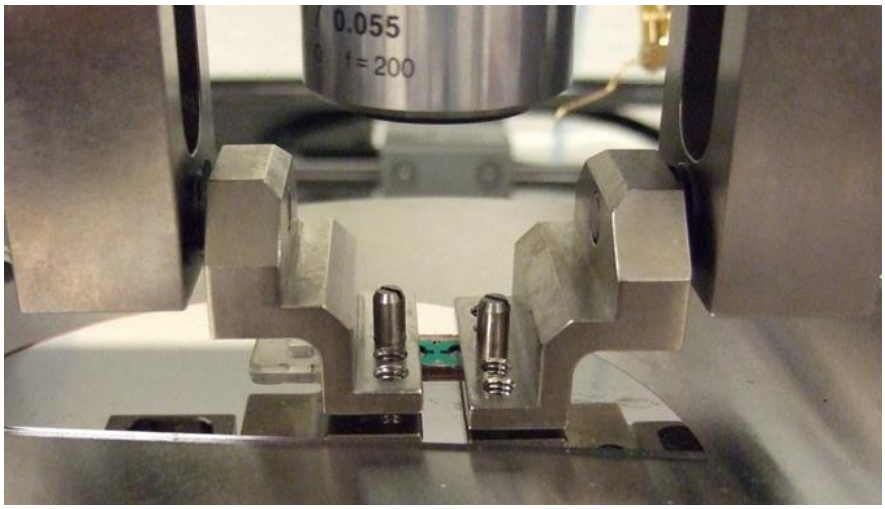

(b)

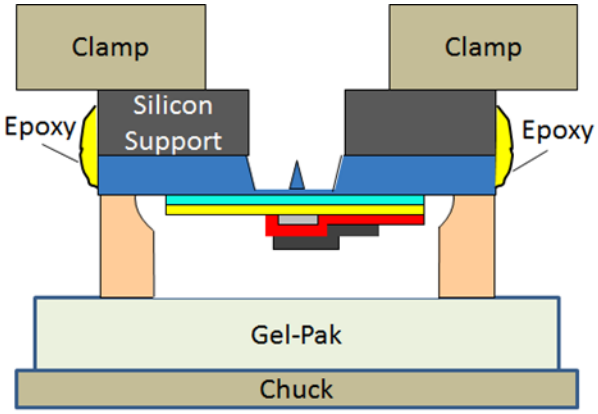

Figure 3-13. Bonding setup picture (top) and cross-sectional B-B' sketch (bottom). Silicon support is aligned to be underneath the probe pads.

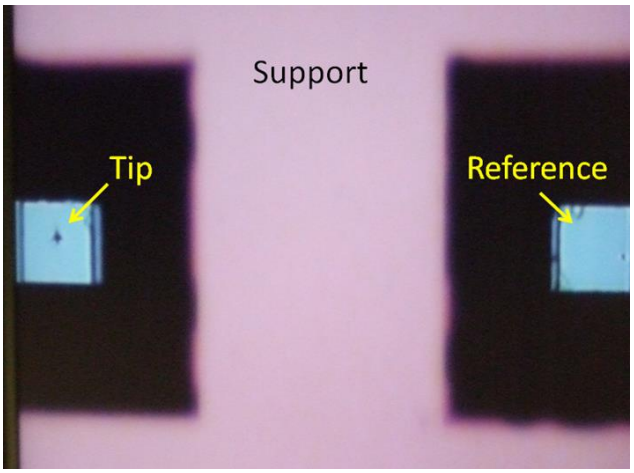

Figure 3-14. Tip-side of device with bonded support aligned to tip openings.

3.5 Measurements at 18.8GHz

With a solid support bonded underneath the probe pads, higher frequency measurements could be undertaken.

Figure 3-19 shows the wide band spectrum of a 1-port device with a bonded support. The device underwent two separate FIB cuts. After the first FIB, rounding of the tip is clear, both from the side view and top view SEMs. (Figure 3-17 and Figure 3-18) However, before and after images of the tip at two different tilt angle show the measured height difference to actually be positive 130 – 180nm. (Figure 3-15 and Figure 3-16) There may be some error in the height measurement due to material on the edge of the trench partially obstructing the view of the tip. It is also quite possible that material sputtered back on to the tip, resulting in an overall positive height difference. The second FIB cut removed an estimated 200 – 300nm of material, including material removed from simply imaging the device. Although the amount of material removed is recorded lengthwise for the tip, material is also removed from the sides of the tip due to imaging (Figure 3-24)

The zero-phase crossing of the 18.8GHz (λ_{Si} = 450nm) series resonance was recorded before and after each FIB cut. Multiple measurements – with RF probes lifted and landed multiple times - were taken for each FIB cut. All measurements are summarized in Figure 3-21 and

Figure 3-25. Due the wide spread of the measured resonances, the data are inconclusive on whether frequency shifts actually occurred.

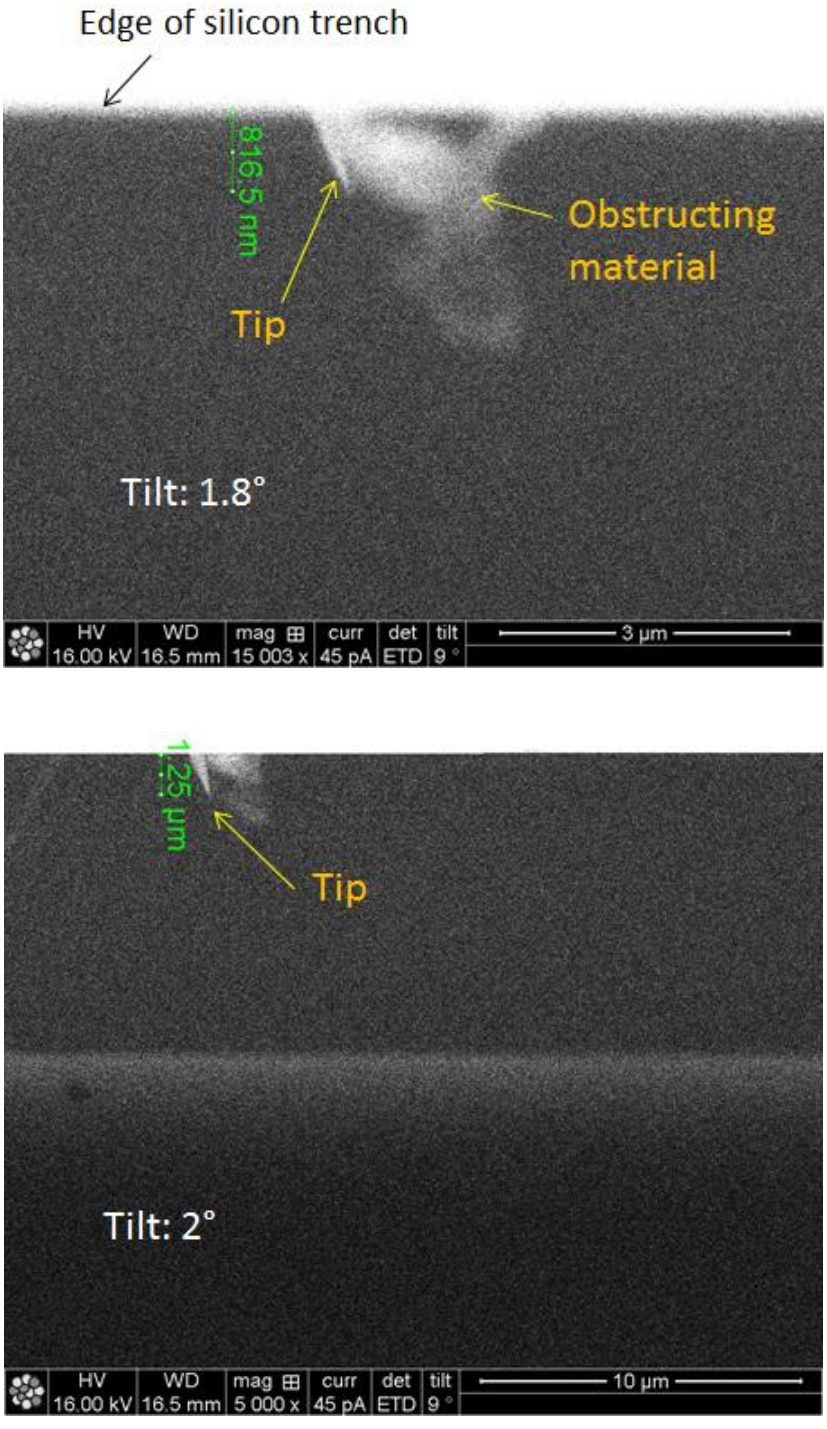

Figure 3-15.Images of the tip right before the first FIB cut . The tip just appears over the edge of the silicon trench. The degree tilt is the angle the tip is tilted into the ion. (Note that the tilt number diplayed at the bottom of the image gives the tilt into the ion beam +7°).

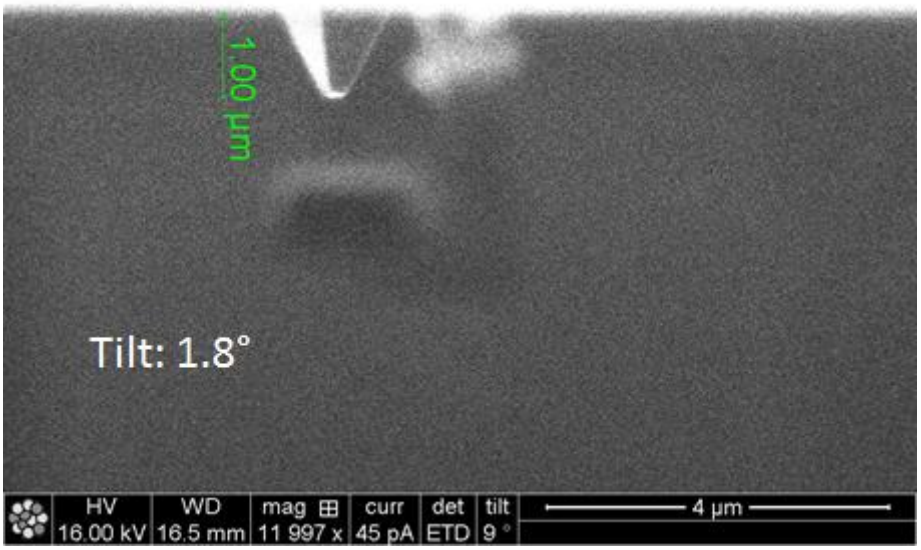

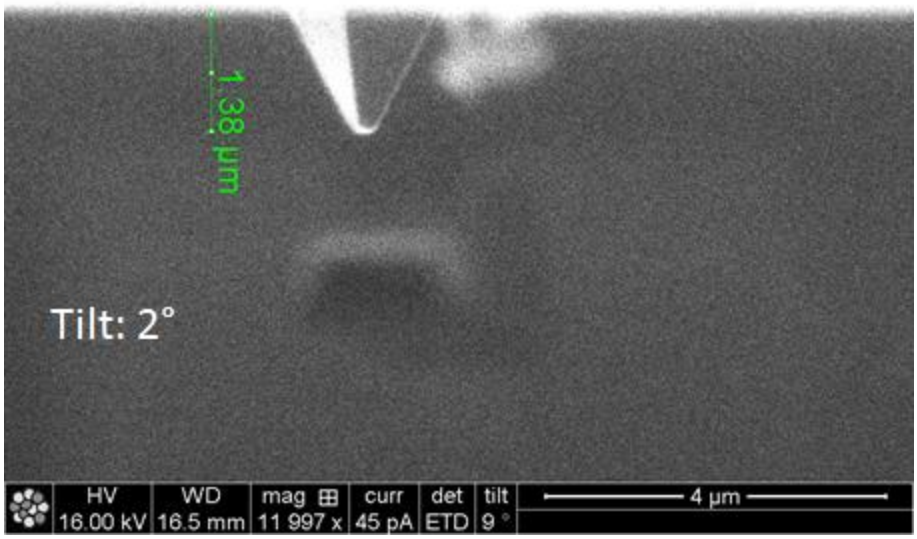

Figure 3-16. Images of the tip after the first FIB cut.

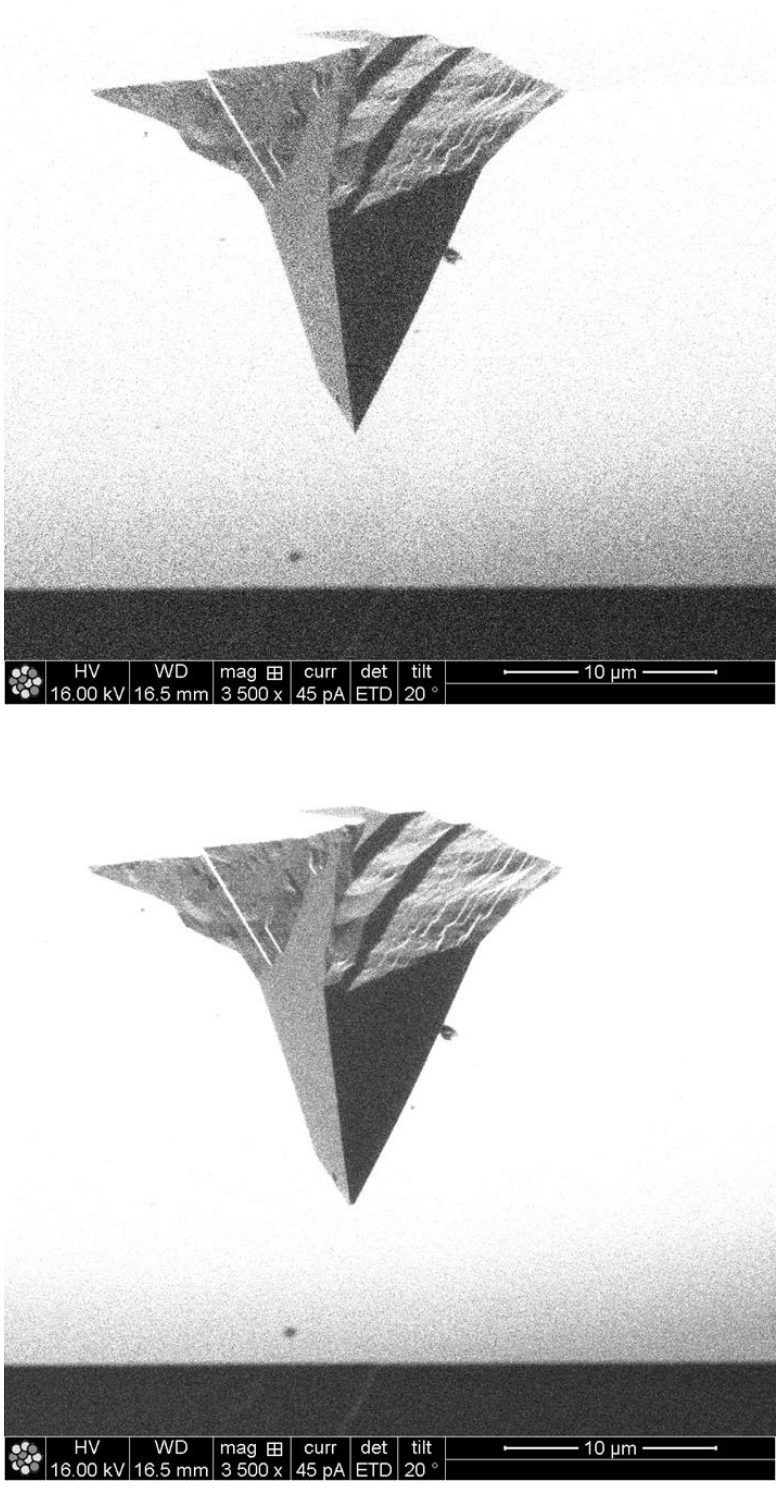

Figure 3-17.Full view of the tip before (top) and after (bottom) the first FIB cut. Slight rounding of the tip apex is evident.

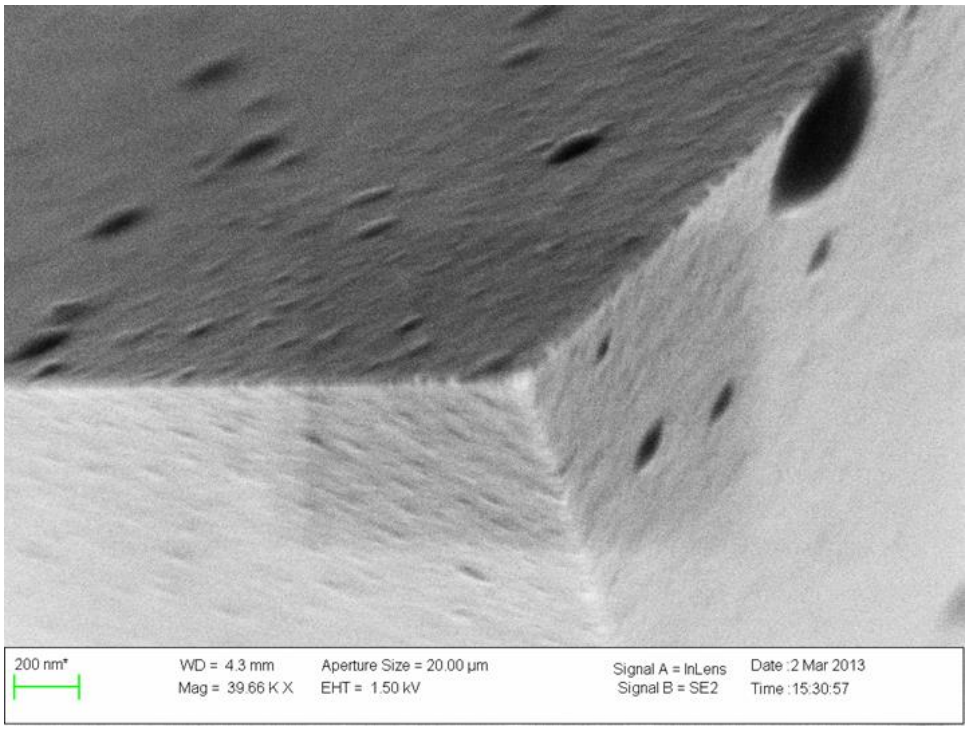

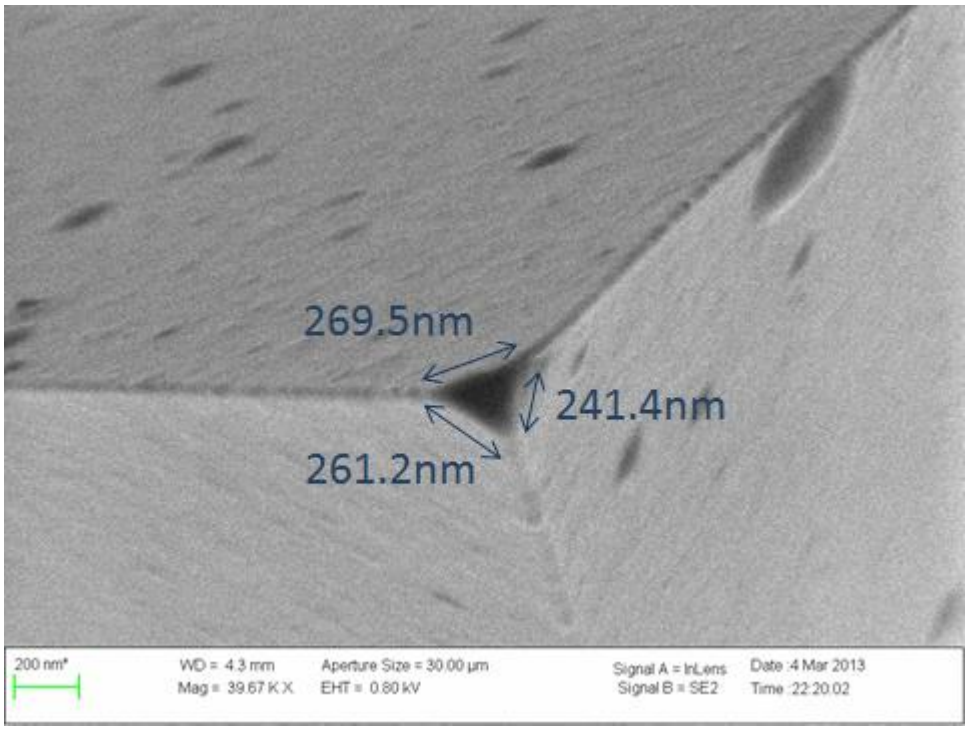

Figure 3-18.Top-view SEM of the tip apex before (top) and after (bottom) the first FIB cut.

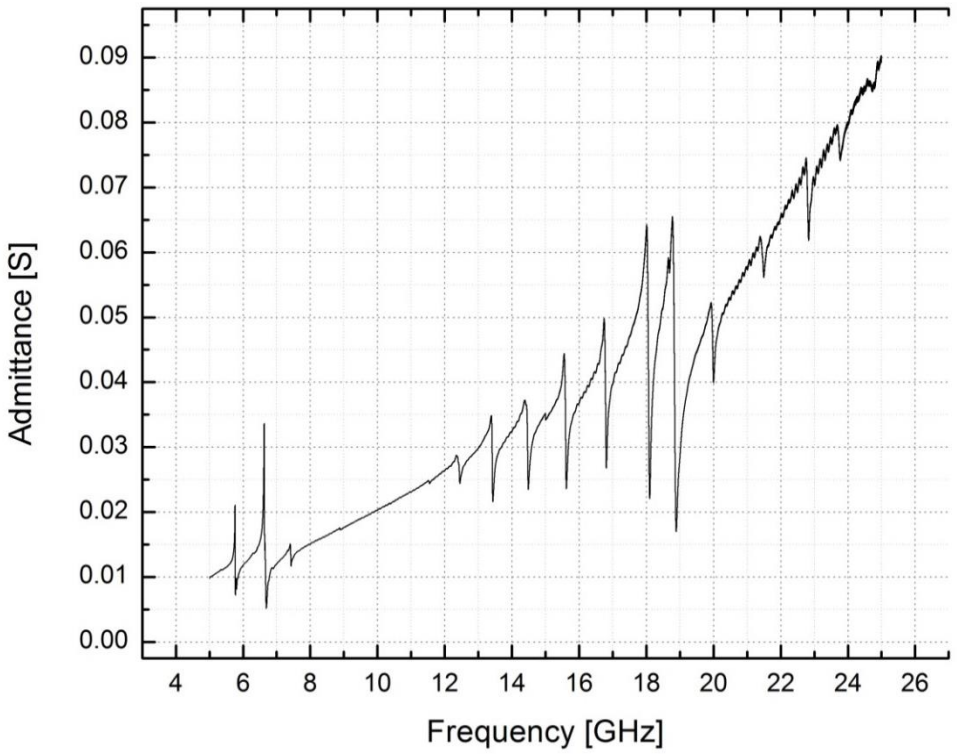

Figure 3-19. Wide sweep of device with bonded support

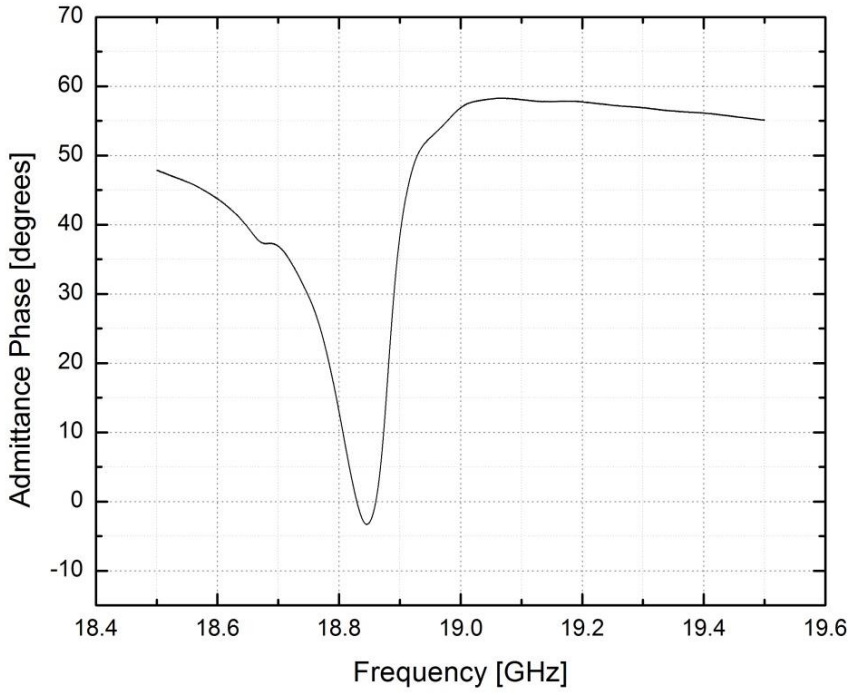

Figure 3-20.Phase zero-crossing at 18.8GHz series resonance

(a)

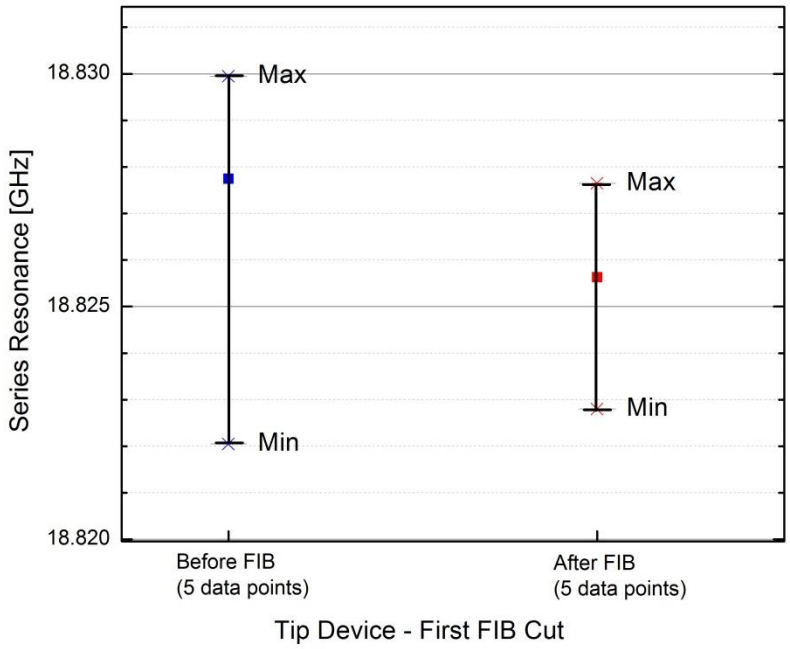

(b)

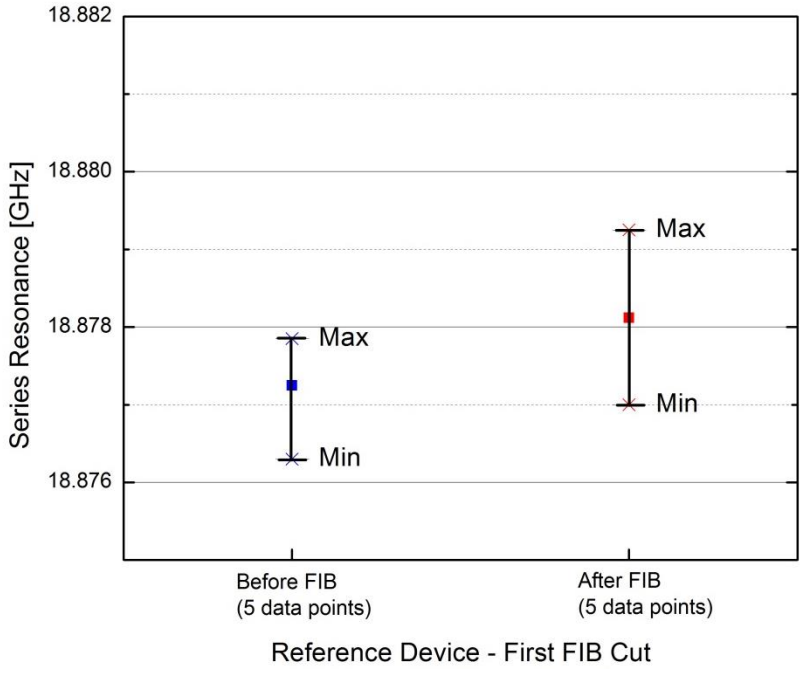

Figure 3-21.Spread of measurements of the series resonance zero-phase crossing before and after the first FIB cut for the tip device (a) and the reference (b)

(a)

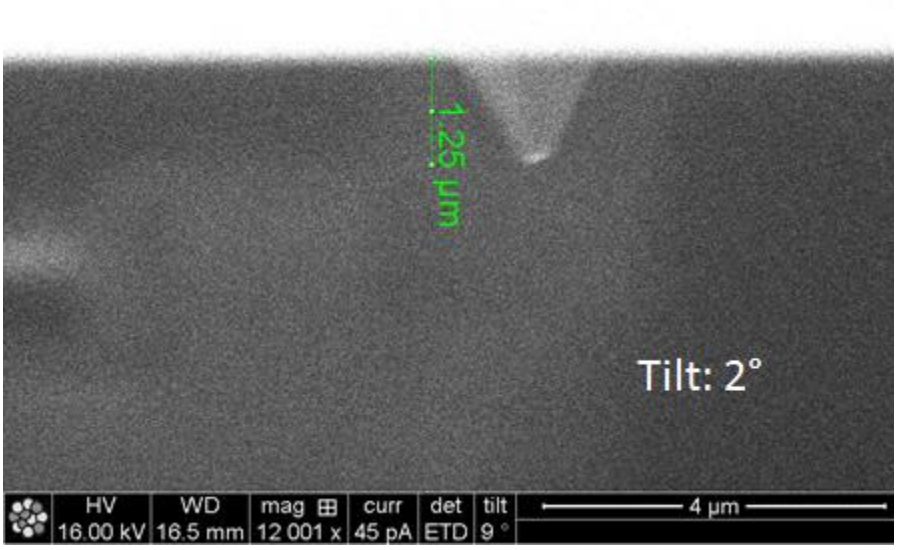

(b)

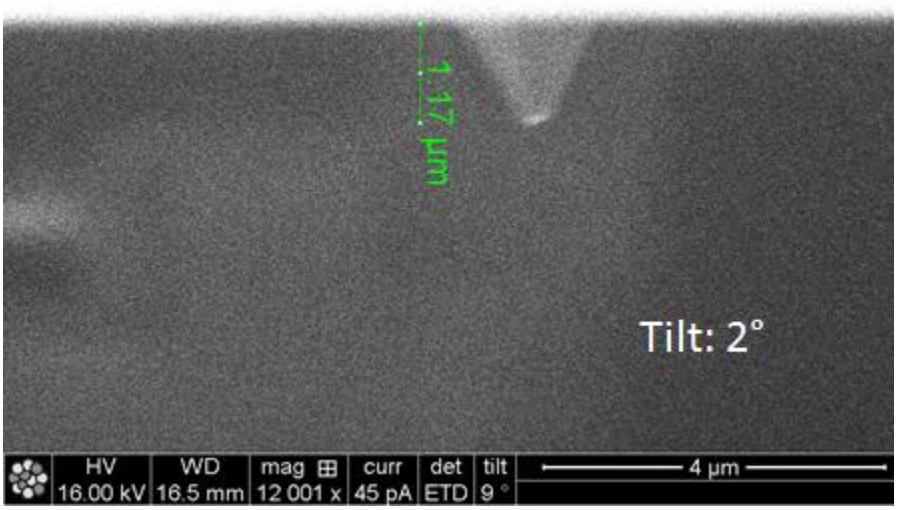

Figure 3-22. Tip some time before the second FIB cut (a) was imaged several minutes later, right before the FIB cut (b). Comparison of the tip height shows that 80nm was removed just from imaging.

(a)

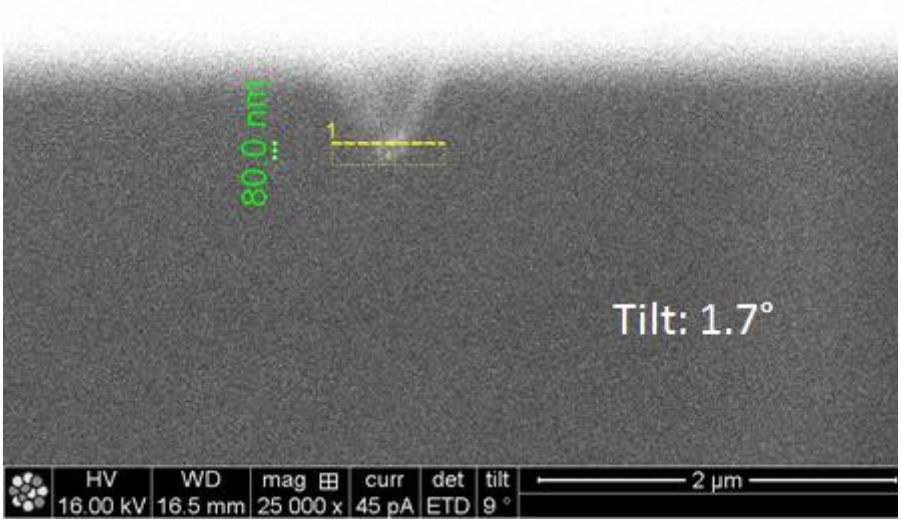

(b)

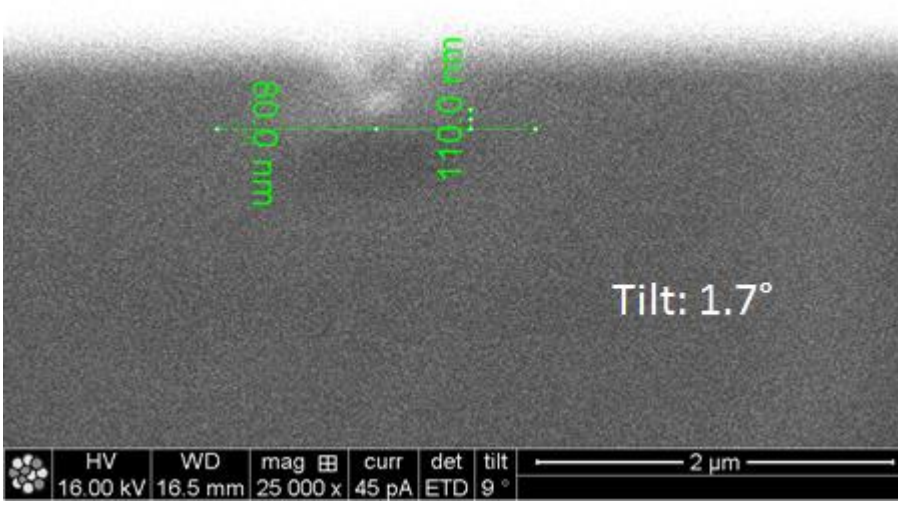

Figure 3-23.Image of the tip tilted 1.7° into the beam immediately before the second FIB cut (a) and immediately after the cut (b). 110nm was removed in addition to the targeted 80nm.

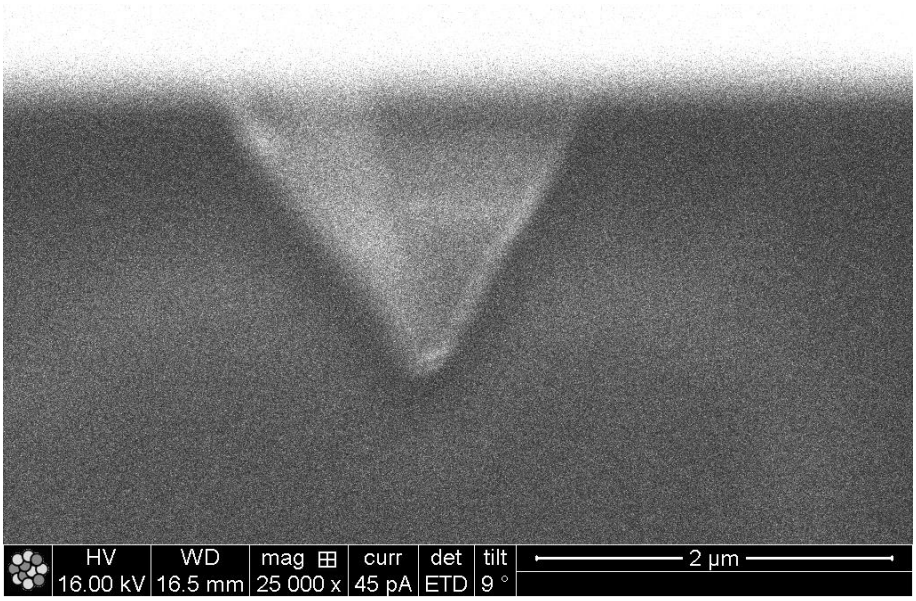

Figure 3-24. Tip at 2.2° tilt into the beam after the second FIB cut. The wavy outline of the tip shows material removed from the apex due to imaging.

(a)

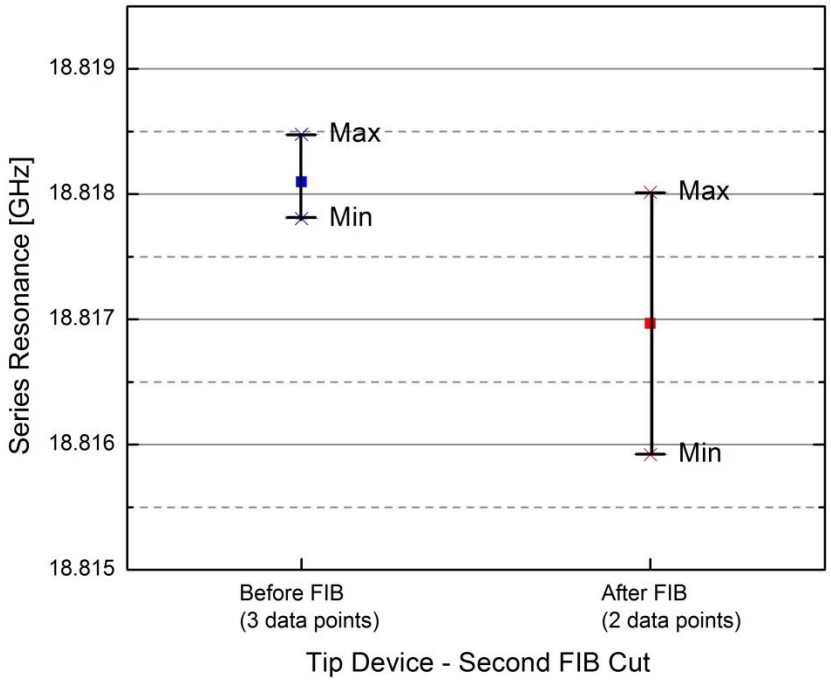

(b)

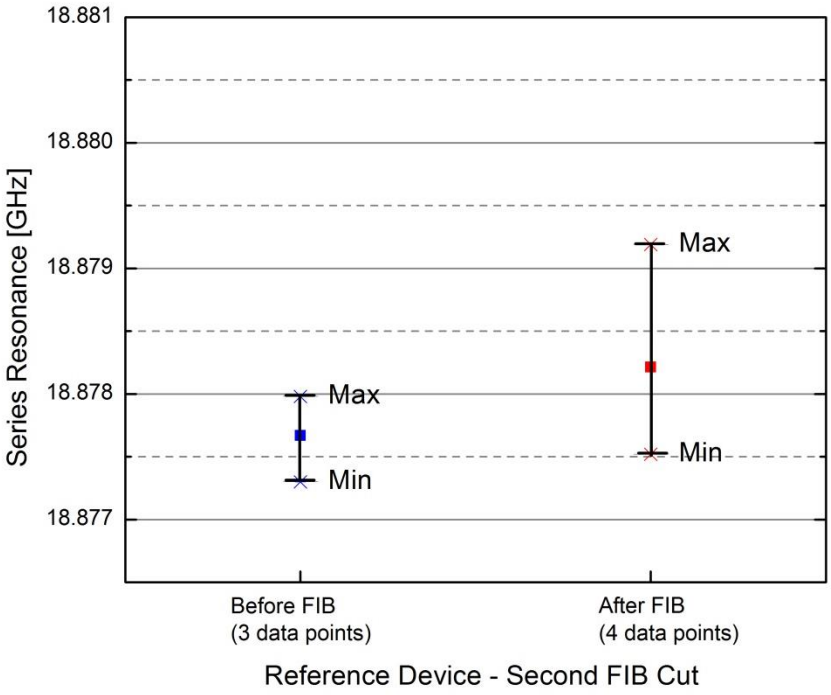

Figure 3-25.Spread of measurements of the series zero-phase crossing before and after the second FIB cut for the tip device (a) and the reference (b)

3.6 Summary

Proof-of-concept AFM resonator devices were fabricated, and a shift at 6.4GHz due to blunting of the tip was demonstrated. The open-loop measurements presented thus far point to many factors that can cause the frequency of the AFM resonator to shift. The solution that will provide a stable frequency source is to put the resonator into an oscillator loop and measure the beat frequency with a reference frequency source, which is discussed further in Chapter 5.

CHAPTER 4

SECOND GENERATION DEVICES

For first generation devices, challenges in the fabrication process resulted in a yield of 10% and misalignment between the tip and the transducer. This chapter details process changes that resulted in a yield of over 50% and close alignment between the tip and transducer.

In Chapter 3, resonance frequency shifts were monitored in response to shortened tip length from focused ion beam cuts. In an actual AFM measurement, the probe tip is not damaged in such a discrete way. Rather, damage can occur at different angles and with different physical manifestations, depending on the scan settings and the sample being imaged. With second generation devices, first steps were taken towards characterizing the resonator under actual AFM measurement conditions. The device was placed into an AFM as the sample, while a tip-less AFM probe "imaged" the sample in tapping-mode, thus inducing damage in the resonator tip. Furthermore, the eventual goal is to take continuous, real-time measurements with the AFM resonator while it is in the AFM system. Towards this goal, devices that were wirebonded out to a PC board were measured in addition to directly probing devices with GSG probes.

4.1 Design

Devices that were to be wirebonded out to a PC board were added to the wafer layout. These devices had bond pads of 240um x 240um. The bond pads were placed just beyond the boundary of the tip membrane. In this way, the bond pad is supported during wirebonding, while giving sufficient distance from the die edge for the wirebond to jump over the 500μm glass border. The layout also included device designs from the first run for probing. To improve the reliability of the probe contact over many probe landings, an additional layer of metallization was added to the probe pads.

In the first run of devices, AlN was left everywhere except for vias to the ground electrodes. In this run, the AlN was patterned such that AlN only remained under the signal electrode. This confines the contribution of excitations to the AlN to the region local to the tip. In addition,

700nm AlN was deposited to target the 6-7GHz frequency range, in which shifts were measured previously.

4.2 Fabrication

In Table 4-1. Process Flow, the full fabrication process flow is shown, with changed or additional steps indicated with an asterisk. These changed steps are detailed in the following sub-sections. Cross-sections are defined in Figure 3-1.

4.2.1 Process Improvement: Protection of the Transducer

One of the main process challenges of the first run was protection of the transducer during the KOH etching steps. In the second generation process, the starting SOI wafer has a thinner handle of 380μm to reduce the etch time needed to remove the handle. Furthermore, additional cleaning steps were introduced prior to anodic bonding to improve the cleanliness of the surface for bonding. The wet etchant used to pattern AlN was changed from TMAH-containing developer to hot phosphoric acid masked by hard-baked photoresist, which is a process taken from [15]. The hot phosphoric acid process left in a very clean surface in the etched areas with minimal erosion of the mask. This was an improvement over the hillocks left behind when using developer as the etchant.

Table 4-1. Process Flow

Cross-section A-A' (see Figure 3-1) unless otherwise indicated *denotes a step that differs from the first generation process	Si SiO_2 Si_3N_4 Glass Au AlN
* 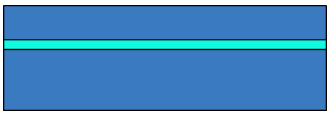	4" SOI wafer. Device layer: 25µm. BOX: 0.5µm Handle: 300µm.
	200nm thermal oxidation
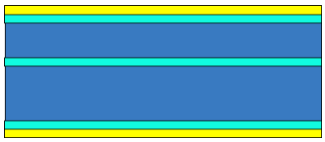	500nm LPCVD low-stress silicon nitride
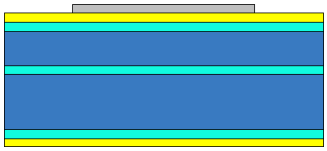	Sputter 25nm/200nm Ti/Pt. Pattern by liftoff.
* 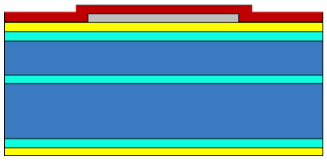	Sputter 700nm of AlN
* 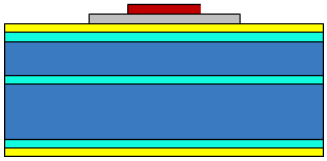	Wet etch AlN in hot phosphoric acid. AlN is patterned everywhere except the transducer.

* 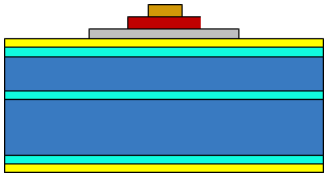	Evaporate 10nm Cr/100nm Au top electrode. Pattern by liftoff.
* Cross-section C – C’ 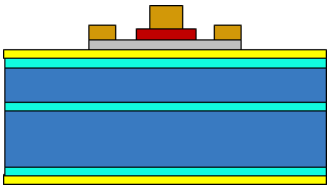	Evaporate 15nm Cr/380nm Au bond pads. Pattern by liftoff.
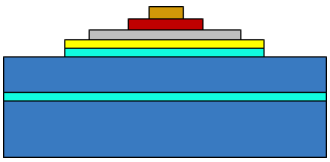	RIE silicon nitride using CHF_3/O_2 Wet etch silicon dioxide in BOE 5:1
* 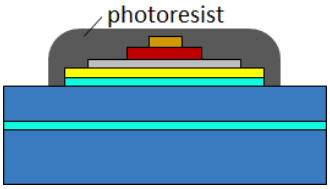	Wet etch residual Cr andAu with photoresist mask
* 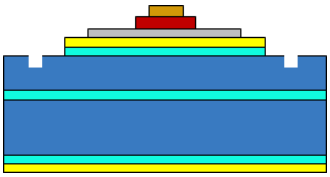	Etch alignment marks for tip mask using CF_6
* 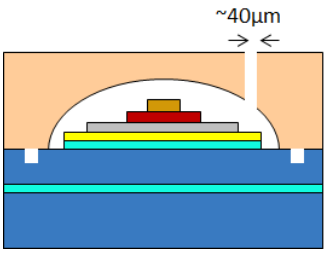	Anodically bond glass carrier wafer. Glass wafer has holes laser drilled into the cavity.

* 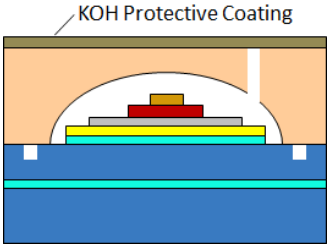	Spin coat ProTEK KOH protective coating over the holes in the glass carrier wafer.
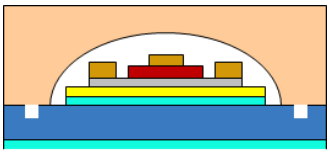	KOH etch SOI handle
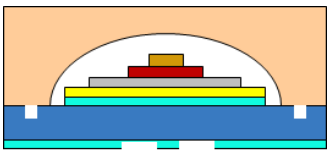	Pattern BOX by wet etching in BOE 5:1
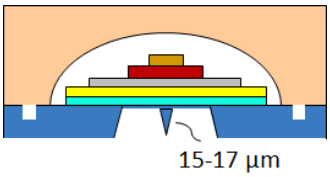	KOH etch tip
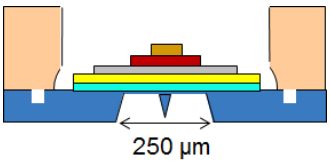 ---------- Cross-section B – B’ 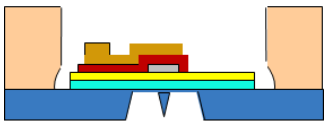	Laser cut glass cavities to access electrodes
See Figure 3-13	Epoxy bond to support for wirebonding and probing

4.2.2 Process Improvement: Alignment of Tip and Transducer

First generation devices were severely misaligned due to a combination of pressurization of the membrane after KOH handle was removed and systematic error of the contact alignment tool during front to backside alignment. The pressurization of the membranes was addressed by puncturing holes in the cavities of the glass carrier wafer prior to anodic bonding. Misalignment error of the tool was corrected by checking front-to-backside alignment using an infrared camera. Holes 30-40μm in diameter were laser cut into the glass cavities using the Universal Laser Systems VersaLaser VLS3.50 (40W CO_2 laser focused at the top surface of the glass cavity with 0.4% power and 1.4% speed). The holes enable pressure to equilibrate between the interior of the cavity and atmosphere after the anodic bond is formed. The complete puncture of the hole was confirmed by profilometer measurements and the ability to focus on a surface on the other side of the hole.

Several layers of a KOH resistant coating, ProTEK B3, were spun to cover the glass holes in preparation for subsequent KOH etching. ProTEK B3 Primer, which is crucial for adhesion of ProTEK B3, was spun first, followed by several layers of ProTEK B3. The glass topography includes 300μm-deep dicing lanes. To ensure that the ProTEK coating covers the top corners and edges of the glass, the coating was spun at a very slow spin speed of 300-400 rpm. At these spin speeds, the ProTEK B3 layer thickness was expected to be >9μm, and two or three layers of ProTEK were expected to be sufficient to cover the holes. The process for multiple coatings of ProTEK B3 was modified from the Brewer Science recommended process for double-coating, which omits the 205ºC bake for the first layer. It was observed that prior to the 205ºC bake, the ProTEK coating appeared to cover all holes. However, after baking at 205ºC, many holes were uncovered, suggesting that the ProTEK coating had shrunk. Hence, several layers were spun in order to improve coverage.

The decision was made to remove the ProTEK coating prior to the tip lithography step. The ProTEK coating posed a problem for tip lithography because of the non-uniform thickness of the coating and the visual distortion of the transducer, to which the tip pattern is aligned. In

addition, some pressurization of the membrane after removal of the SOI handle was observed, although to a lesser extent than for first generation devices. The suspected cause is again pressurization due to sealing of the cavity at high temperature – this time because of baking ProTEK B3 resist at 205°C. After tip lithography, Kapton tape is placed over the glass holes to prevent the wet etchants of subsequent steps from entering the glass cavity and attacking the transducer. The KOH etch of the tip was performed die by die, with various layers of protection over the glass holes – Kapton tape, epoxy, and Apiezon W100 wax.

4.2.3 Other Process Changes

The glass cap was opened using the Versalaser 40W CO_2 laser at a power of 1.8%, with the laser focused 0.1mm above the glass top surface. Four cuts were made along the border of the square cavity top. After making the cuts, tape was placed over the glass surface. Gentle pressure or tapping was applied to the laser cuts to make the final break. The tape was then peeled away, removing the glass cavity top.

4.3 Fabrication Results

The changes implemented in the second generation process flow lead to an improved yield of >50%, as well as better alignment between the tip and the transducer (Figure 4-2). Misalignment was improved from 55µm to 10µm.

The anodic bonding proceeded much faster than in previous runs, which suggests that the surface was cleaner and had fewer particles to obstruct the propagation of the bond. Figure 4-1 shows the state of the wafer after the SOI handle was etched. The yield is vastly improved from the first run. The loss of some die was possibly due to a localized weak anodic bond and/or insufficient coverage of ProTEK over some holes.

The tips from this run have jagged facets (Table 4-3). The suspected cause is impurities in the KOH solution due to the presence of epoxy and wax as protective layers on the glass.

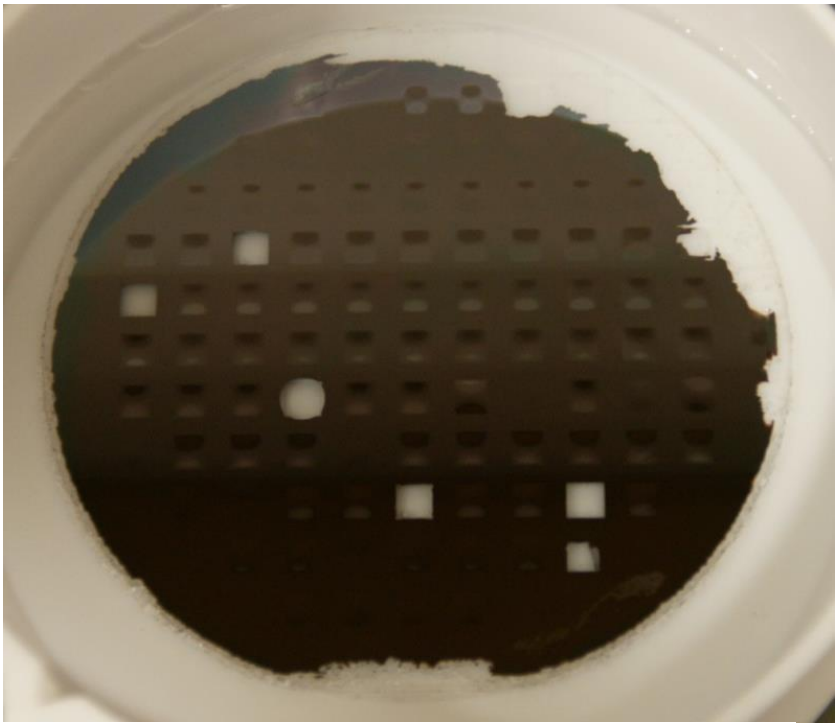

Figure 4-1. Top view of wafer after KOH etch of SOI handle

(a)

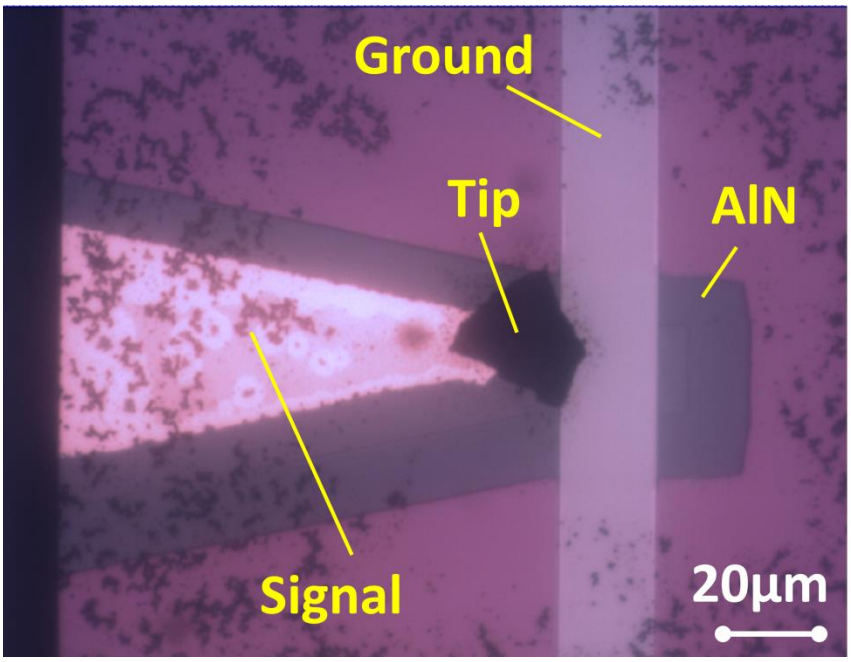

(b)

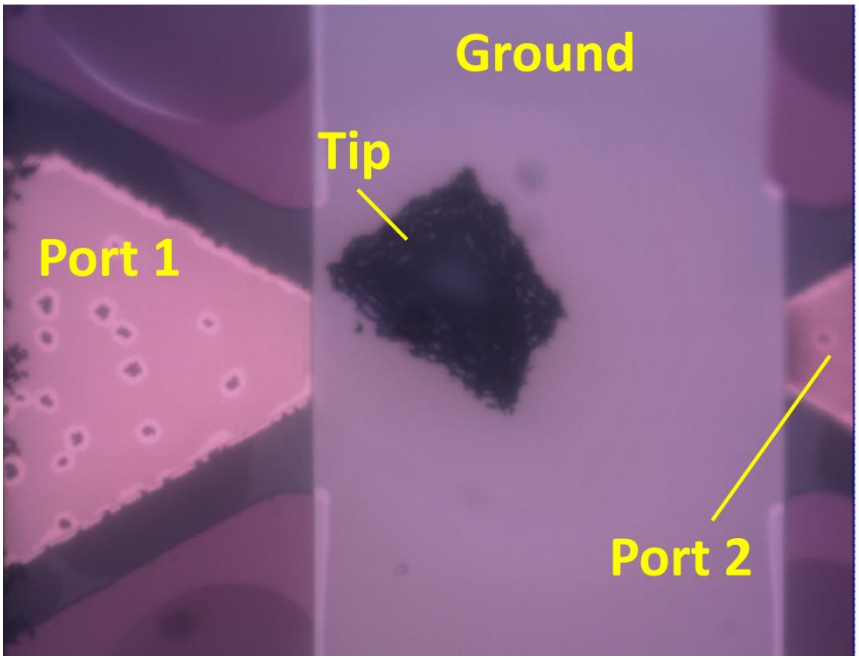

Figure 4-2.Top view of devices. (a) Tip is misaligned from transducer by 10µm (b) On a larger transducer area, the tip is misaligned, but still underneath the transducer

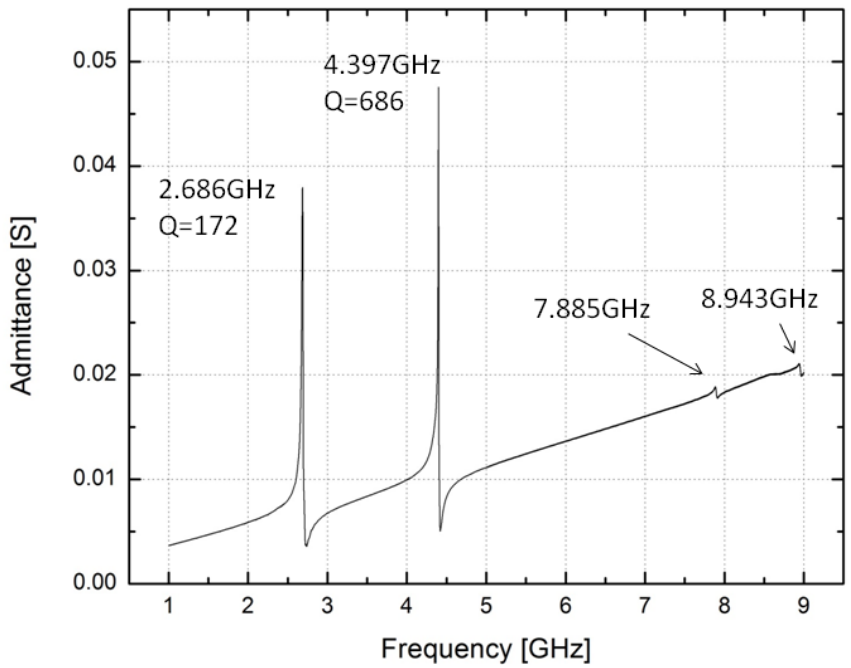

Figure 4-3. Frequency response of 50 μm diameter device measured on-wafer with GSG probes

(a)

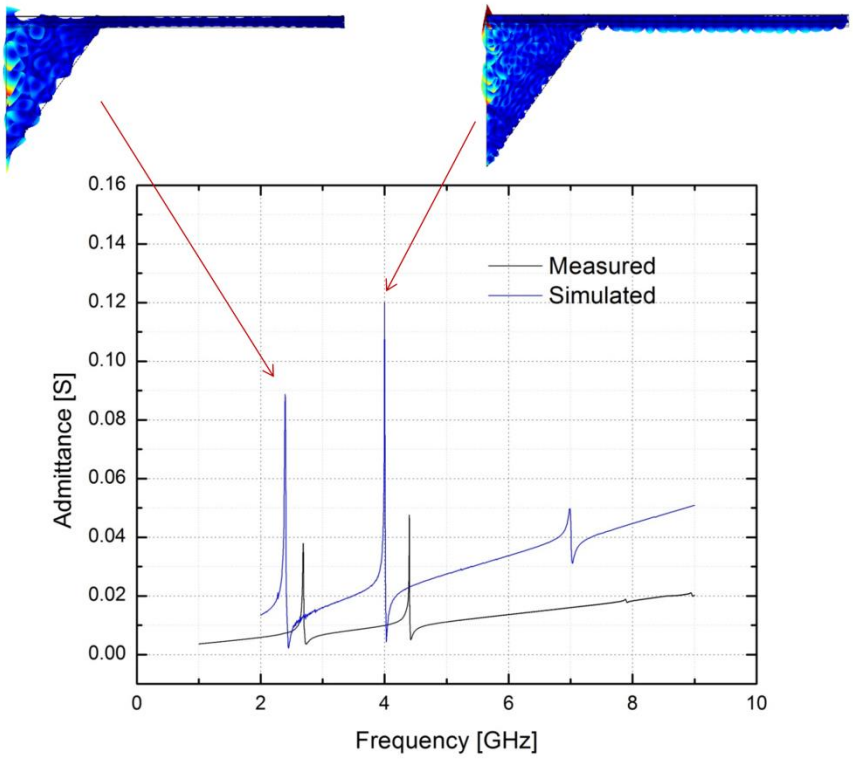

(b)

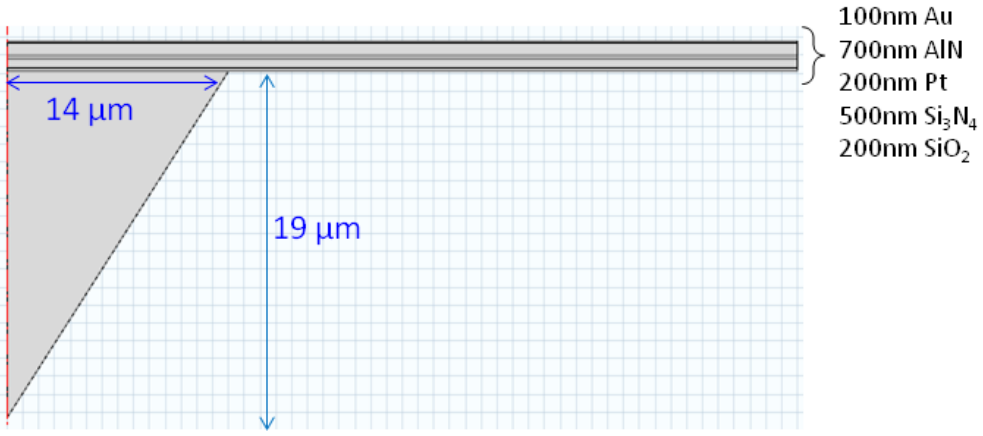

Figure 4-4. (a) Comparison between simulated and measured frequency response. (b) Structure and parameters used for simulated structure

4.4 Measurements

Figure 4-3 shows the spectrum of a device with a 50µm-diameter circular transducer that was measured by landing Picoprobe 40A GSG probes directly on the transducer electrodes. On-wafer calibration using a CS-5 Picoprobe calibration substrate was performed up to the probe

tips. Comparison with Comsol simulation (Figure 4-4) shows a reasonable match of resonant modes at 2.69GHz and 4.4GHz. Half of the structure was simulated in 2D, with an axisymmetric boundary condition on the left boundary and free boundary conditions everywhere else. The actual asymmetric tip is therefore approximated to be a symmetric cone. Dimensions of the simulated tip were determined from SEMs of the fabricated tips. The discrepancy between the capacitive floors of the simulated and measured responses is due to differing transducer areas. This has no effect on the location of the series resonance peak.

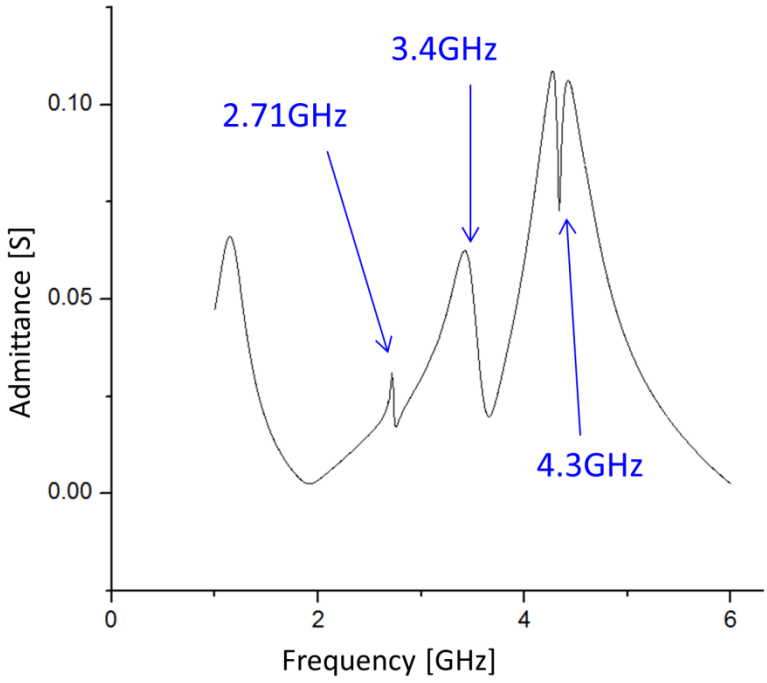

Figure 4-5. Frequency response of a 100 μm – diameter wirebonded device.

The admittance spectrums for wirebonded devices were measured in air by connecting the device via SMA to an Agilent N5230A PNA-L network analyzer. A DC block was placed between the device and the port of the network analyzer. Calibration up to the device SMA connector was performed using the Agilent 85053C calibration kit. RF power applied to the device was -5dBm.

Given that the transducer is the same thickness and the tips are of similar heights, the mechanical modes of the probed and wirebonded devices are expected to be at similar frequencies. The spectrum of a wirebonded device with a 100μm-diameter circular transducer (Figure 4-5) shows evidence of significant electrical parasitic effects. The resonance peak at 2.71GHz coincides with the resonance at 2.68GHz from on-wafer probe measurements, but is lower in Q and amplitude. This can be attributed to an impedance mismatch, and further work needs to be done to improve the design of the PC board as well as the wirebond. Other peaks at 1.2GHz, 3.4GHz, 4.2GHz, and 4.4GHz are of noticeably lower Q. These resonances are also absent from the spectrum in Figure 4-3, suggesting that they may be electrical. The sharpness of the dip at 4.3GHz and its coincidence with the 4.4GHz peak in Figure 4-3 suggest that the dip could be the parallel resonance of the same mechanical mode. The electrical parasitics are most likely due to the long and curved wirebonds, which are described in the following section.

4.4.1 Measurement Setup on the AFM

The section describes the setup of the damaging the tip in the AFM. The mounted AFM probe had a tip-less cantilever 225 μm long, with a force constant of 48 N/m and resonance frequency of 190 kHz (NanosensorsTM model TL-NCL). The AFM resonator with tip facing up was used as the sample. In tapping-mode, the tip-less cantilever was brought into contact with the tip and tapped across the tip to induce damage.

Figure 4-6 shows a side view sketch of the setup and picture of the actual setup. Two wirebonds per bond pad were made from the die to the PC board. The die and PC board were arranged at the same height to minimize the wirebond length. However, the presence of the glass perimeter of the die means that the wirebond is a minimum of 6mm. Combined with the fact that the signal trace on the PC board is set back from the edge, the wirebonds were 7 to 9mm in length. In addition, the bonds were curved, in order to clear the 500μm thick glass enclosure. All three components – die, PC board, and soldered SMA mount – were stuck with double-sided tape to one holder so as to minimize movement between the three components. The tip-side of

the die is exposed such that it can be hit by the cantilever.

(a)

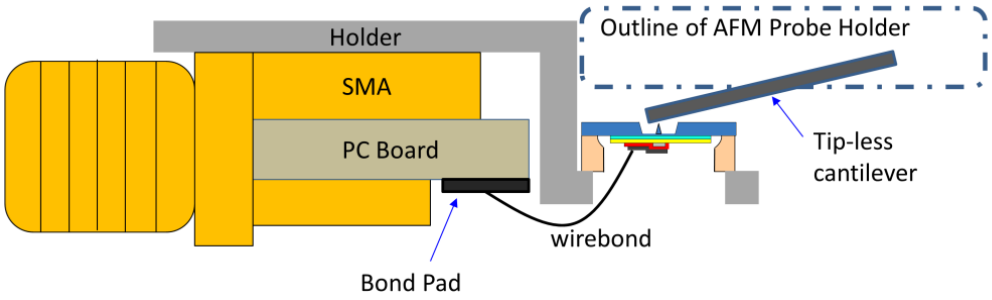

(b)

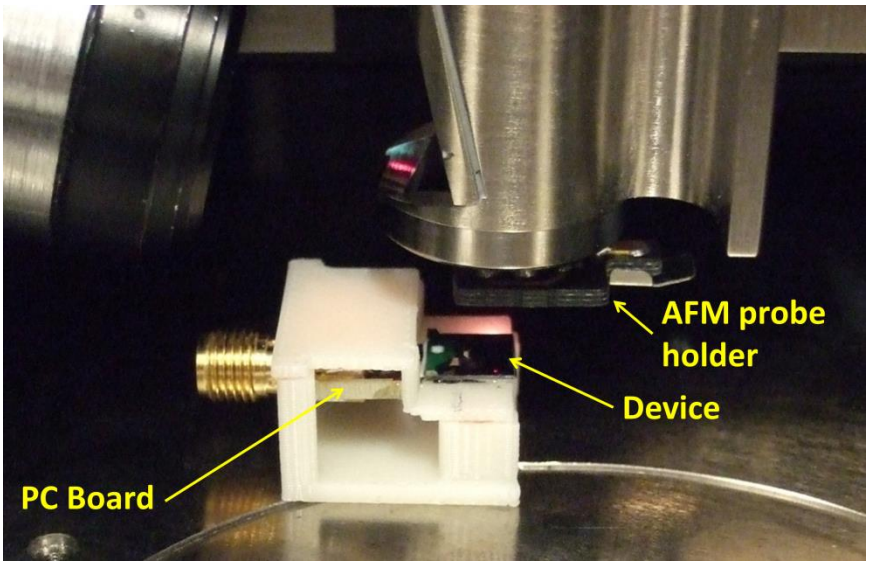

(c)

(d)

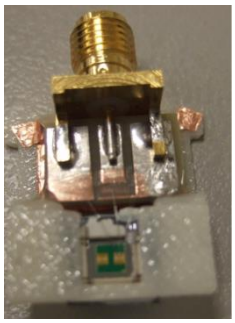

(e)

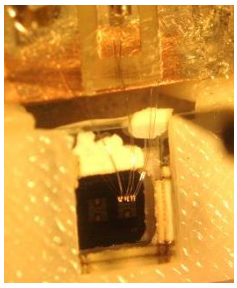

Figure 4-6. Schematic (a) and side view picture (b) of measurement setup in AFM. View of tip-side (c) and transducer-side (d) of the die. (e) shows the wirebonds from the device to the PC board.

The silicon support is bonded to just one half of the die (where the bond pads are located) to

allow the cantilever access to hit the tip. Sufficient room must be given for the holder for the AFM probe (Figure 4-6a, dotted outline), which extends beyond the end of the cantilever. Figure 4-6c to 4-6e show pictures of an actual device.

4.4.2 Damaging the Tip

The tipless cantilever was engaged on the tip apex, and several tapping-mode measurements were performed. The procedure for a typical AFM measurement was followed: after the cantilever was engaged, scan settings were adjusted until trace and retrace curves followed each other closely. Table 4-2 refers the sequence of taps to which the tip was subjected; tap number 1 refers to the first tap, tap number 2 refers to the second tap, etc. Table 4-2 also details the AFM scan area, how many passes were made over the entire scan area and/or the time spent on each tap in minutes. "N/A" indicates that the information was not available for that particular tap. RF measurements were taken before and after each tap.

After the third tap, the drive amplitude was decreased considerably in order to increase the force of the cantilever against the tip. While no damage was seen after the first and second taps, the third tap resulted in the removal of a chunk of the tip apex (Table 4-3). No damage was noticeable after the fourth and fifth taps, while tap 6 resulted in some surface damage.

The series resonance frequency at 2.71GHz was extracted from the peak of the admittance vs. frequency plot and recorded after each tap. Figure 4-7 shows the relative frequency shifts between each tap and the preceding tap. The point Δf_s for the n^{th} tap is the frequency shift between tap n and tap n-1. Δf_s for the 1^{st} Tap corresponds to the frequency shift between Tap 1 and the undamaged device. Blue circles indicate when visible damage was observed on SEMs of the tip, i.e., after the 3^{rd} tap and the 6^{th} tap. A large frequency shift can be seen from Tap 2 and to Tap 3, which corresponds to significant damage to the tip. This preliminary data suggests that the sensor is sensitive to changes at the tip end.

Table 4-2. Sequence of Taps to Damage the Tip

Tap Number	Scan Area	Number of Passes	Time
1	1. 120nm x 120nm 2. 100nm x 100nm	N/A	1. 2 min. 2. 5 min.
2	100-120nm x 100-120nm	N/A	8 min
3	1. 7µm x 7µm 2. 30µm x 15µm	1. N/A 2. 2.5	1. 20 min 2. N/A
4	6µm x 6µm	2.5	7 min
5	1. 6µm x 6µm 2. 6µm x 3µm	1. 2 2. 7 – 8	N/A
6	1. 6µm x 6µm 2. 10µm x 10µm 3. 30µm x 30µm 4. 30µm x 15µm	N/A	1. ~15 min 2. ~15 min 3. 20-30 min 4. 20-30 min

Table 4-3. SEMs of the Same Tip After Successive Taps

Tap	Top View	Side View
Tap 0	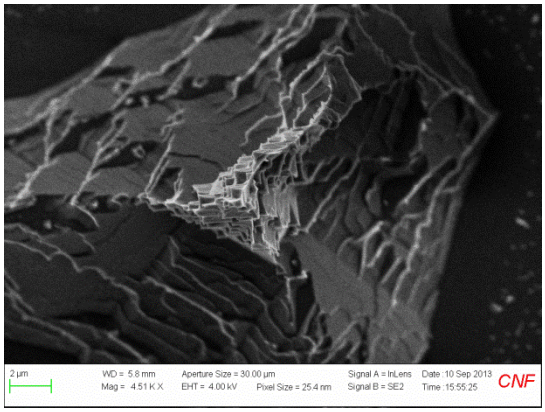	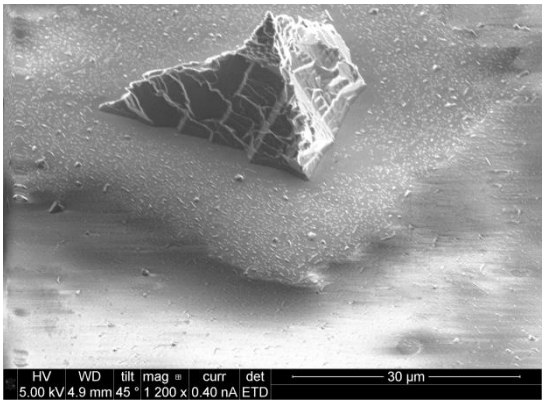
Tap 2	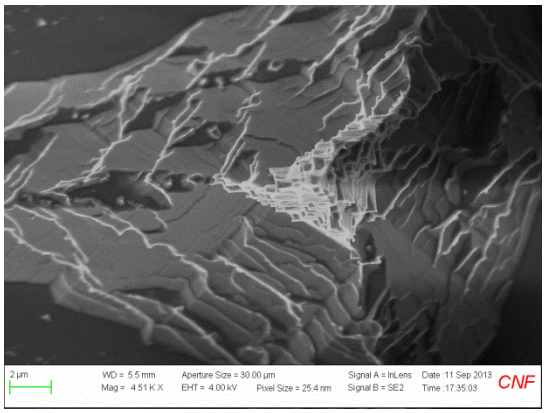	N/A
Tap 3	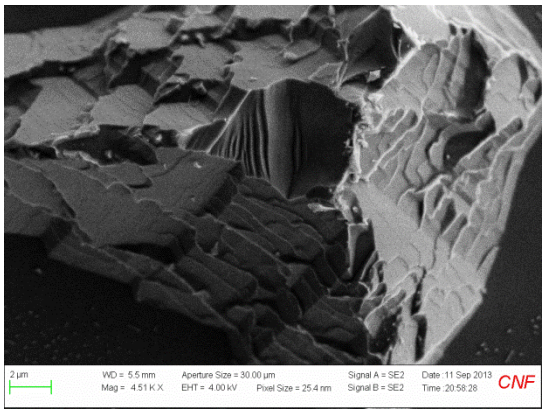	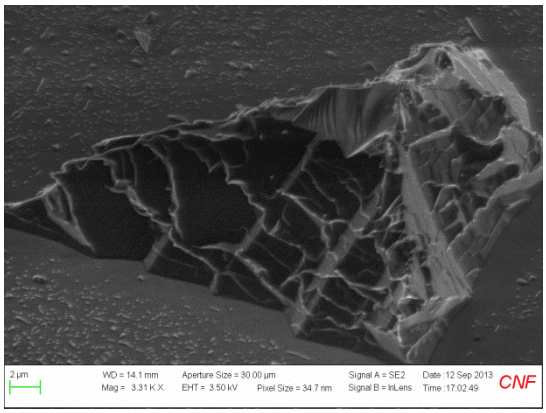

Tap 4	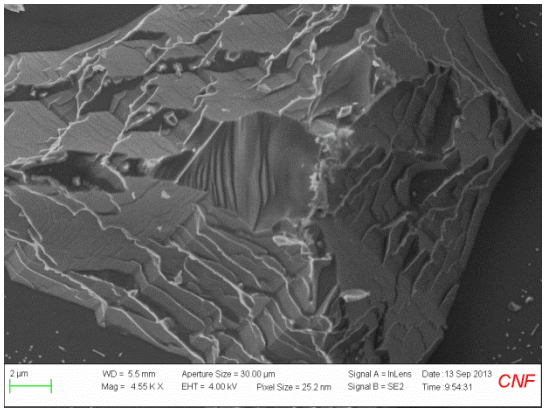	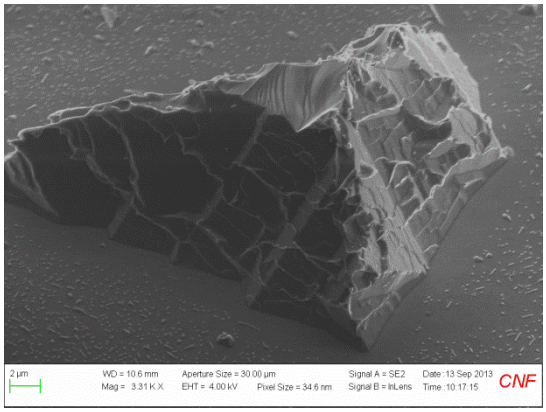
Tap 5	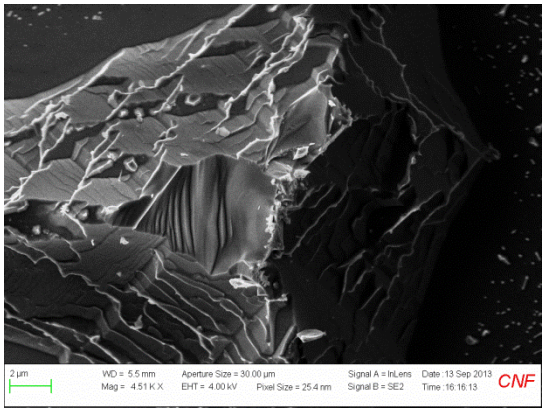	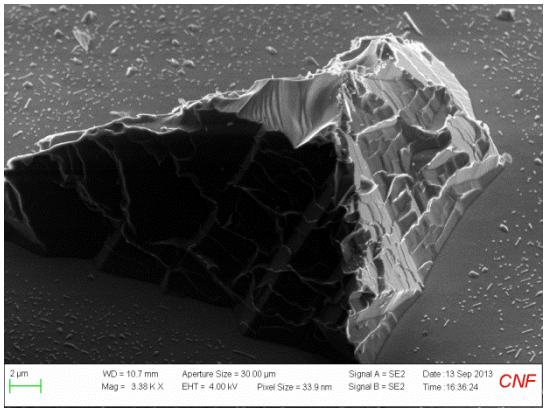
Tap 6	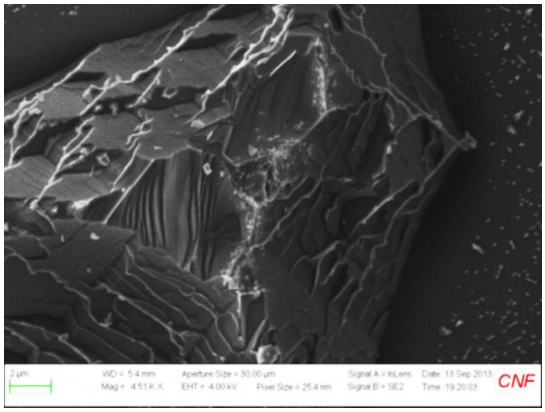	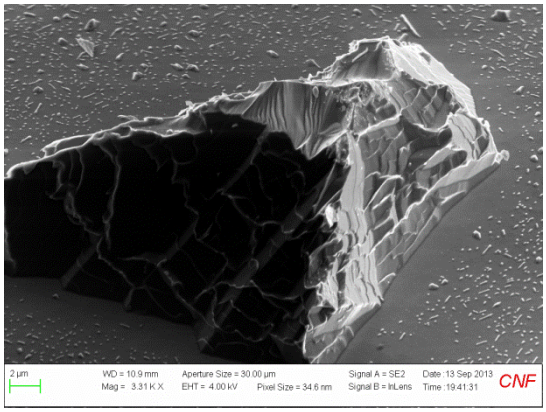

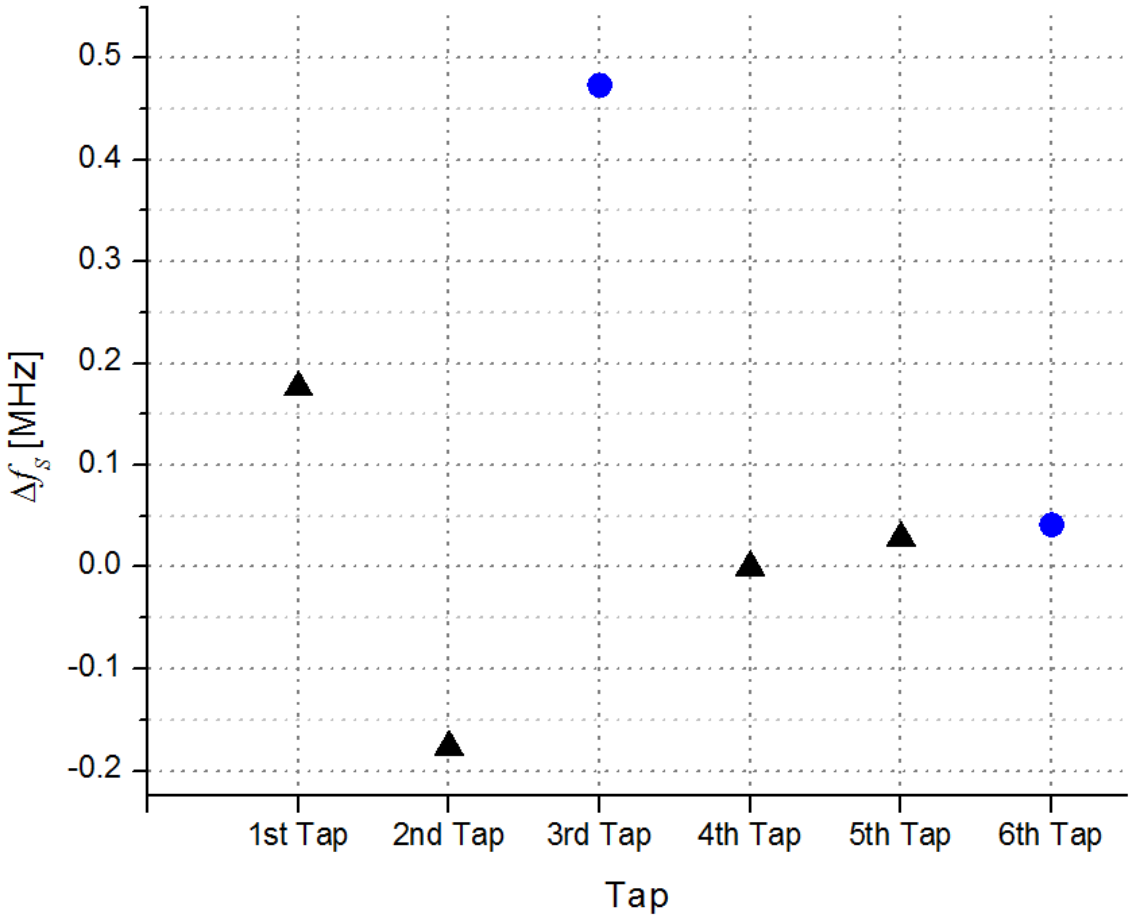

Figure 4-7. Frequency shift versus tap for the 2.71GHz resonance of the device in Table 4-3. Blue circles indicate the taps at which visible damage was observed on the tip.

4.4.3 Conclusion

Fabrication yield was improved through the process changes detailed in this chapter, and the setup of the resonator in an actual AFM measurement was successfully implemented. The measurement results of the wirebonded devices suggest the strong influence of electrical parasitics and an impedance mismatch from the presence of the wirebonds. Further design iterations on the PC board and on the die need to be performed to minimize these effects. The die was designed to have a large distance between the device and glass to provide sufficient clearance for landing RF probes. Such a large distance is no longer necessary for wirebonding. The die-to-edge distance can be shortened, thereby reducing the lateral length of the wirebonds. The main obstacle for wirebonding is the $500\mu m$ height of the glass surrounding the die. Two possible ways of reducing the glass height are: use a thinner glass wafer at the outset; and/or just prior to wirebonding, use laser rastering to thin select areas of the glass where the wirebonds cross the glass. For the PC board, the GSG trace spacing should be made similar to the device GSG spacing to facilitate shorter wirebonds. The GSG traces can then be impedance matched to the SMA side by gradually increasing the width of the traces from the die wirebond to the SMA.

CHAPTER 5

FUTURE WORK

5.1 Summary

The AFM bulk acoustic resonator was presented as a device that enables real-time monitoring of tip wear for atomic force microscopy and tip-based nanofabrication. A dual-side fabrication process was implemented that successfully integrated an aluminum nitride transducer on top of a silicon tip. Measurement results show a frequency shift of -0.4MHz at 6.4GHz due to discrete tip blunting, as well as frequency scalability up to 20GHz. Improvements upon the first generation process increased yield from 10% to >50% for the second generation of devices. The first steps were taken towards building devices that can be measured in real-time while tip damage occurs.

5.2 Process with Integrated AFM Cantilever

The fabricated devices in this thesis are not functional as scanning AFM probes due to the absence of a cantilever, which is necessary for generating an image of the sample.

Figure 5-1 shows the cross-section of a commercial AFM tip. The typical process flow for a silicon probe consists of the following steps, starting with a silicon wafer: (1) etch of tip on the front side; (2) tip sharpening by a series of oxidation steps; (3) front-side etches to define the cantilever and probe body; (4) backside etch to release the probe.

Figure 5-1. Cross-section of a commercial AFM probe

Fabricating the piezoelectric transducer on top of the tip is difficult to implement in a commercial process. If transducer processing is placed at the end of the process, the height of the probe body *h* presents a challenge both for lithography and quality control of aluminum nitride. The drastic change in topology may affect the long-range crystal ordering of AlN. Protection of

the tip during transducer processing may also be problematic. Placing the tip etch after transducer fabrication, such as in the process presented in this thesis, makes tip sharpening impossible. The metal layers in the transducer cannot withstand high temperature oxidation. Furthermore, integration of the transducer with the large step of the probe body presents the same issues previously mentioned. One possible alternative is to provide the probe body support by bonding to another wafer, rather than etching the probe body out of the same wafer as the transducer and tip.

In [16] piezoelectric layers were successfully integrated close to the tip, but not on top. Figure 5-2 shows a simplified process flow reproduced from [16], in which a zinc oxide actuator is fabricated on the same side as the tip. This process can be modified for AlN to obtain the appropriate RF operating frequencies and high piezoelectric coupling factor. However, further work must be done to determine if and how RF acoustic waves will couple into the tip when the transducer is placed in this position.

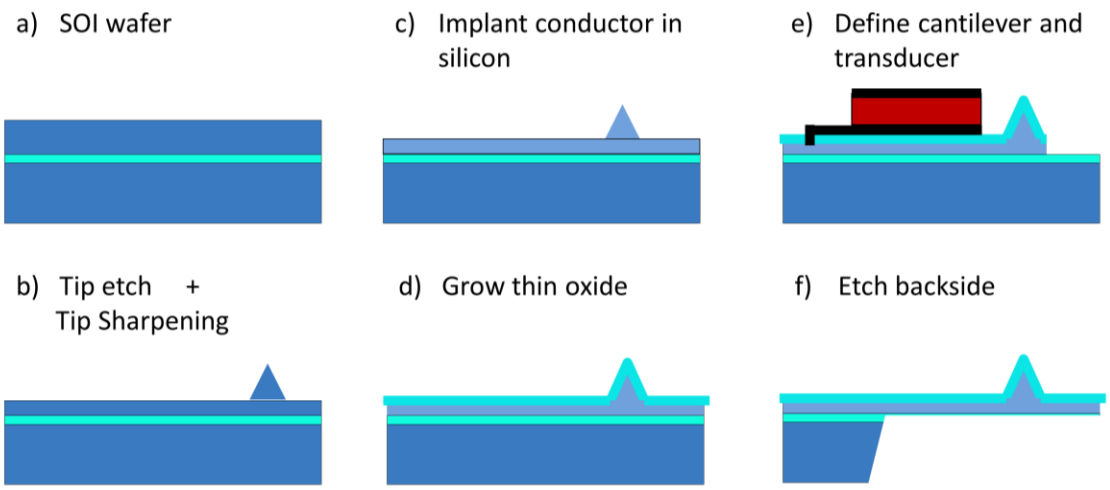

Figure 5-2. Process flow for fabricating a piezoelectric transducer on the same side as the tip. Process is reproduced from [16].

5.3 Oscillator

The open-loop measurement scheme limits the AFM resonator's effectiveness as a standalone sensor. Putting the resonator into an oscillator loop would create a stable frequency

source, enabling improvements in accuracy and resolution of frequency variations due to tip wear. To control for environmental effects, the beat frequency between the oscillator and a reference frequency source can be monitored.

The Pierce oscillator topology has been used to successfully demonstrate oscillators based on piezoelectric resonators as high as 1.01GHz. [17] The circuit simulator Cadence was used to simulate a Pierce oscillator based on the measured performance of the device in Figure 3-8. The measured k_t^2 = 0.6% was too low to achieve oscillation. Successful oscillation *was* achieved assuming k_t^2 = 4% at 6.39GHz and Q=356. The circuit (Figure 5-3) was simulated using the IBM BiCMOS 6HP 0.25µm process. The resonator is represented by C_x, L_x, R_x and C_3 (static capacitance of the resonator). V_{dd} = 2.5V and the bias current = 17.8mA. To bias the gate node, a large resistance, implemented by NMOS transistor M_{fb} operating in subthreshold, was placed between the gate and drain nodes of NMOS transistor M_1. M_{fb} is sized to be W/L = 300nm/4µm. M_1 is sized to be W/L = 328µm/240nm (composed of 82 fingers) to achieve g_m = 78mS. An explicit 800fF capacitor was placed at the drain of M_1. Including parasitics, total capacitance values are: C_1 = 300fF, C_2 = 900fF, and C_3 = 72fF. The frequency pulling of the device is 0.003 for this design, translating to an offset of about 19MHz from the resonator series frequency.

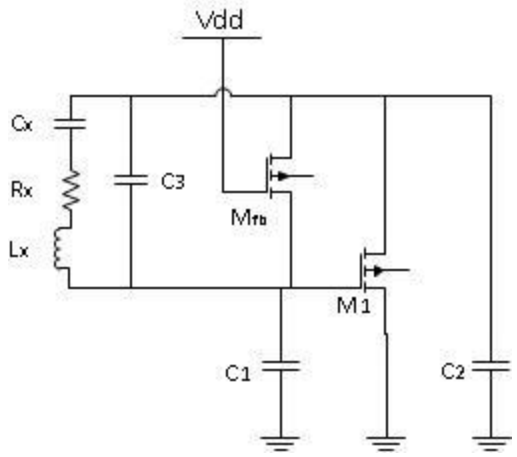

Figure 5-3. Pierce oscillator circuit

Second generation devices provided a first step towards implementing an electrically

packaged resonator that can be wirebonded out to other circuitry, such as an oscillator feedback circuit. Suggestions for improving the electrical performance of wirebonded AFM resonators were mentioned in Chapter 4.

APPENDIX A

FABRICATION PROCESSES

A.1 Process Flow for Second Generation Devices

Table A-1 shows the chronological process flow in detail for second generation devices. All steps except those marked with an asterisk were performed at the Cornell Nanofabrication Facility. Steps with an asterisk were performed in Professor Chung Hoon Lee's laboratory at Marquette University.

Section 4.2.2 gives details on the preparation of the glass carrier wafers prior to anodic bonding.

Table A-1. Process Flow for Second Generation Devices

Process Type	Mat/Mask	Tool	Process Parameters
Start	substrate		4" SOI wafer from Ultrasil Device layer: 25µm. BOX: 0.5µm Handle: 300µm.
Oxidation	SiO2	Furnace B2	Recipe 8 (Wet Ox w/HCL) Load/unload: 12"/min Temp: 1000C Thickness: 200nm
LPCVD	LSN	Furnace B4 or E4	Recipe 3 (LSN). Load/unload: 12"/min Temp: 800P. Thickness: 500nm 4 bracket wafers on each end.
Clean	Wafer	Hamatech	Wafer clean piranha OR 2 hours in Nanostrip, 25^{o}C
Bottom Electrode Deposition			
Dehyd. Bake	Wafer	Hot Plate	180C, 3 min.
Cool	wafer	Air, cooling plate	
Spin	LOR10A	Spinner	1) 500 rpm/10,000 ramp/10s 2) 3000 rpm/10,000 ramp/45s
Bake	LOR10A	Hot Plate	180 C, 5 min

Cool	wafer	Air, cooling plate	
Clean	LOR10A	Swab	Remove flakes from edge bead
Spin	SPR 220-3.0	Spinner	3000 rpm/1000 ramp/30s
Bake	SPR 220-3.0	Hot Plate	115 C, 85 s
Cool	wafer	Cooling plate	
Expose	SPR 220-3.0	ABM	8 s (365nm + 405nm)
Develop	SPR 220-3.0 + LOR10A	Base Hood	3 min in 726 MIF. Gently agitate every 30s.
Inspect		Microscope	LOR undercuts resist 0.5-0.75μm
Measure	Resist	P10	~3607nm
Descum	SPR 220-3.0 + LOR10A	Ox80	50sccm O2, 30 mTorr, 100W 1 min 45s PR etch rate: 50-70nm/min
Paint scratches	SPR 220-3.0	Swab	Dab resist over tweezer scratches. Air dry ~2 hrs until hardened.
Sputter	Ti/Pt	Clark Hall Sputterer	1) Ti in yellow angled gun DC 1K, 100W. Presputter 10 min Deposit 25nm 2) Pt in blue vertical gun DC 1.5K, 100W. Presputter 6.5-10 min Deposit 200nm
Liftoff	Ti/Pt	Basehood	All steps performed with wafer facedown, elevated from the bottom of the beaker. This lets the metal fall away from the wafer. 1) 1165 >6hrs until metal is suspended in solution. Place facedown, elevated from bottom of beaker. 2) Transfer to clean 1165 bath, preferably heated 50^{o}C. 3) Sonicate 10 min. Facedown 4) Repeat Step 2. Sit for 2 min. 5) Transfer to IPA. Sonicate 2-3 min. Sit for 2-3 min. 6) Transfer to DI wafer. Sonicate 2-3 min. Sit for 2-3min. 7) Spin Rinse Dry
AlN			
Sputter	AlN	OEMGroup Foundry	224nm - 1500nm. FWHM = 1.5-4^{o}
Dehyd. Bake		Hot Plate	115C, 5 min

Cool		Air	5 s
Spin	P20	Spinner	2000 rpm/1000 ramp/30s
Spin	S1818	Spinner	2000 rpm / 1000 ramp/ 30s (2.5 μm)
Bake	S1818	Hot Plate	115C, 90s
Expose	S1818	ABM	8 s (365nm + 405nm light)
Develop	S1818	Base Hood	Shipley Microposit CD-30, 3min 30s
Descum	S1818	Ox80	O2: 50 sccm, Pressure: 30 mTorr, RF: 100 W 1min 45s
Bake	S1818	Oven	120 C, 12 hours
Cool	wafer	Air cool	
Etch	AlN	Base Hood	Phosphoric acid, 150 C. For 700nm AlN: 40s. For 1500nm AlN: ~80s.
Strip	S1818	Base Hood	Heated 1165, 50C. Sonicate 1 hour.
Top Electrode			
Dehyd. Bake	wafer	Hot Plate	115 C, 3 min
Spin	P20	Spinner	2000 rpm/1000 ramp/30s
Spin	S1818	Spinner	2000 rpm / 1000 ramp/ 30s (2.5 μm)
Bake	S1818	Hot Plate	115 C, 90s
Expose	S1818	ABM	8 s (365nm + 405nm light)
PEB	S1818	Hot Plate	115 C, 1 min
Develop	S1818	Base Hood	Shipley Microposit CD-30 3 min 30s
Paint scratches	S1818	Swab	Dab resist over tweezer scratches. Air dry ~2 hrs until hardened.
Descum	S1818	YES Asher	100 sccm, 1000W, 30 C 1) 30-60s 2) Rotate wafer 180^o 3) 30-60s
Measure	S1818	P10	~2.4 μm
Evaporate	Cr/Au	NBTC CHA	10nm Cr / 100nm Au Rate: 0.8 – 1 angstroms/s

Liftoff	Cr/Au	Base Hood	* Note: Had difficulties with metal fencing with positive resist 1) Facedown in acetone, sit for 1 min Sonicate in 10s bursts every 1-2 minutes, several times. 2) Soak until metal is suspended in solution. 3) Sonicate 20 minutes. 4) IPA sonicate 2 min 5) DI water sonicate 2 min 6) Dry
Bond Pad			
Dehyd. Bake	Wafer	Hot Plate	180C, 3 min
Spin	LOR10A	Spinner	1) 500 rpm/10,000 ramp/10s 2) 3000rpm/10,000 ramp/45s
Bake	LOR10A	Orange Hot Plate	180 C, 5 min
Cool	wafer	Cooling plate	20s
Clean	LOR10A	Acetone swab	Remove flakes from edge bead
Spin	SPR 220-3.0	Spinner	3000 rpm/1000 ramp/30s
Bake	SPR 220-3.0	Hot Plate	115 C, 90 s
Cool	wafer	Cooling plate	20s
Expose	SPR 220-3.0	ABM	8s (365nm + 405nm light)
Develop	SPR 220-3.0 + LOR10A	Base Hood	3-4 min in 726 MIF. Gently agitate every 30s.
Descum	SPR 220-3.0 + LOR10A	YES Asher	O2 descum followed by Ar descum
Evaporate	Cr/Au	Even Hour or Odd Hour Evaporator	15nm Cr / 380nm Au
Liftoff	Cr/Au	Base Hood	Same as for Metal 1
Clean	wafer	Base Hood	1) Acetone 2 min 2) IPA 2 min 3) DI rinse 4) N2 dry
Clean BondingArea			
Dehyd. Bake	wafer	Hot Plate	115 C, 5 min.
Spin	P20	Spinner	3000 rpm/1000 ramp/30s
Spin	SPR 220-3.0	Spinner	3000/1000/30s.
Bake	SPR 220-3.0	Hot Plate	115C, 90s
Expose	SPR 220-3.0	ABM	9s (365nm + 405nm light)

Inspect	wafer	Scope	Inspect for holes in resist. Develop will attack any exposed AlN areas.
Develop	SPR 220-3.0	Hamatech	726 MIF, 90s, DP
Measure	SPR 220-3.0	P10	~2.7 μm
Descum	SPR 220-3.0	YES Asher	100 sccm, 950W-1000W, 30C 1) 60s 2) Rotate wafer 180^o 3) 60s.
Measure	SPR 220-3.0	P10	~2.5μm
Etch	Au in bonding area	Acid Hood	1) Gold Type TFA Etch, 5 min. 2) Quench in DI water 30s-1min 3) Rinse DI water 1 min. 4) Spin Rinse Dry
Etch	Cr in bonding area	Acid Hood	1) CR-14 Cr etch, 5 min. 2) Quench in DI water 30s-1min 3) Rinse DI water 1 min. 4) Spin Rinse Dry
Strip	SPR 220-3.0	Base Hood	1165 or acetone + IPA, sonicate
Strip	wafer	YES Asher	100 sccm, 950W-1000W, 30C 1) 60s 2) Rotate wafer 180^o 3) 60s.
Clean	wafer	SRD	
Expose Silicon for Anodic Bonding			
Dehyd. Bake	wafer	Hot Plate	115C, 3-5 min
Spin	P20	Spinner	3000 rpm/1000 ramp/30s
Spin	SPR 220-3.0	Spinner	2500 rpm/1000 ramp/30s (~2.8 μm)
Bake	SPR 220-3.0	Hot Plate	115C, 90s
Expose	SPR 220-3.0	ABM	14s
Inspect	SPR 220-3.0	Scope	For holes in resist. Develop will attack any exposed AlN areas.
PEB	SPR 220-3.0	Hot Plate	115C, 1 min
Develop	SPR 220-3.0	Base Hood	1min 40s in 726MIF, while agitating
Descum	SPR 220-3.0	Ox80	50 sccm O2, 30mTorr, 100W, 1min 45s
P10	SPR 220-3.0	resist height	3.41um

RIE	LSN	Ox80	1) Season with LSN dummy Recipe: 50 sccm CHF3, 5 sccm O2, 55mTorr, 150W, Time: 3 min. ER: 44.7nm/min 2) Etch LSN + 30% overetch 3) Color of underlying oxide should be dark brown or purple.
Etch	oxide	Acid Hood	BOE 6:1, 5 min
Strip	resist	Base Hood	1) 1165, heated 50C, 2 baths 15-20 min in each bath, sonicating 2) IPA 1-2 min 3) DI water 1-2 min 4) Spin Rinse Dry
Etch Alignment Marks for Tip Etch			
Dehyd. Bake	wafer	Hot Plate	115C, 3-5 min
Spin	P20	Spinner	3000 rpm/1000 ramp/30s
Spin	SPR 220-3.0	Spinner	2500/1000/30s
Bake	SPR 220-3.0	Hot Plate	115C, 90s
Expose	SPR 220-3.0	ABM	14s
Inspect	SPR 220-3.0	Scope	For holes in resist. Develop will attack any exposed AlN areas.
PEB	SPR 220-3.0	Hot Plate	115C, 1 min
Develop	SPR 220-3.0	Base Hood	726 MIF, 1min 40s, while agitating
Descum	SPR 220-3.0	Ox80	50sccm, 30 mTorr, 100W 1-2 min
P10	SPR 220-3.0	resist height	3.24um
Etch	Si	Ox80	1) Season with bare Si wafer CF4 etch (30sccm CF4, 40mTorr, 150W) 3 min 2) CF4 etch, 180nm deep
Strip	SPR 220-3.0	Base Hood	1) 1165, heated 50C, 2 baths 15-20 min in each bath, sonicating 2) IPA 1-2 min 3) DI water 1-2 min 4) Spin Rinse Dry
Clean Particles			
Clean	wafer	Base Hood	1) 1165, heated 50C, sonicating 2) IPA, sonicate 2 min 3) DI water, sonicate 2 min 4) Spin Rinse Dry
Anodic Bond			

* Bond	Glass and silicon wafer		1000V across glass and silicon Heat to 500C
Etch SOI Handle			
Spin	ProTEK B3 Primer	Spinner	500-1000 rpm
Bake		Hot Plate	205C, 60s
Spin	ProTEK B3-25	Spinner	300-400rpm
Bake		Hot Plate	140C, 120s
Spin	ProTEK B3-25	Spinner	300-400rpm
Bake		Hot Plate	205C, 60s
Spin/Bake	ProTEK B3-25		Repeat previous 2 steps several times
*Etch	SOI handle		30% wt KOH, 60C, 20+ hrs
*Etch Tip			
*Spin/ Expose			Resist mask (~1μm)
*Etch	SOI BOX		BOE 5:1, 5 min
*Etch	Si		30% wt KOH, 40-60C, ~1hr
*Strip	Resist		Acetone
Open Glass Cavities			
Laser Cut		Versalaser VLS3.50	40W CO2 Laser. 1.8% power Focused 0.1mm above glass surface

A.2 Process Details for First Generation Devices

In the process flow for first generation devices, the AlN etch and top electrode steps were performed differently from the process of the second generaetion. Those steps are outlined in Table A-2.

Table A-2. First Generation Processes for Top Electrode and ALN Layers

Process Type	Mat/Mask	Tool	Process Parameters
Top Electrode			
Dehyd. Bake		Hot Plate	115C, 5 min
Spin	XHRi-16 ARC	Spinner	5000 rpm/5000 ramp/30s ~160nm
Bake	XHRi-16 ARC	Hot Plate	175C, 60s

Spin	nLOF2020	Spinner	3000 rpm/1000 ramp/60s ~1.8μm
Bake	nLOF2020	Hot Plate	115C, 60s
Expose	nLOF2020	ABM	2s (365nm + 405nm light)
Bake	nLOF2020	Hot Plate	115C, 60s
Develop	nLOF2020	Base Hood	726MIF, 60s
Descum + Remove ARC	nLOF2020 + ARC	YES Asher	100 sccm, 1000W, 30 C 1) 120s 2) Rotate wafer 180^o 3) 120s
Evaporate	Al	NBTC CHA	200nm
Liftoff	Al	Base Hood	All steps performed with wafer facedown, elevated from the bottom of the beaker. This lets the metal fall away from the wafer. 1) 1165 >6hrs until metal is suspended in solution. Place facedown, elevated from bottom of beaker. 2) Transfer to clean 1165 bath, preferably heated 50^{o}C. Sonicate 10 min. facedown 3) Repeat Step 2. Sit for 2 min. 4) Transfer to IPA. Sonicate 2-3 min. Sit for 2-3 min. 5) Transfer to DI wafer. Sonicate 2-3 min. Sit for 2-3min. 6) Spin Rinse Dry
AlN			
Sputter	AlN	OEMGroup Foundry	224nm FWHM = 1.5-4^o
Spin	P20	Spinner	2000 rpm/1000 ramp/30s
Spin	S1818	Spinner	2000 rpm/1000 ramp/30s
Bake	S1818	Hot Plate	115C, 90s
Expose	S1818	ABM	8s (365nm + 405nm light)
Develop	S1818	Base Hood	1:1 solution of Microposit Developer Concentrate in DI water 3 min.
Bake	S1818	Hot Plate	115C, 10 min
Etch	AlN	Base Hood	726MIF, ~8 nm/min
Strip	S1818	Base Hood	1) Acetone 10 min 2) IPA 2 min 3) 1165 1.5 hours 4) DI water rinse 5) Spin Rinse dry

APPENDIX B

STUDY OF QUALITY FACTOR IN SILICON CARBIDE HBARS

The presented AFM resonators all have tips that are fabricated out of single-crystal silicon. Silicon is widely used for commercial scanning probe tips because it is a hard material, micro-machinable, and cost-effective. While using harder materials, such as diamond , can be an effective solution to increasing tip longevity, materials that can enhance sensor performance are of interest for the AFM resonator. To this end, silicon carbide is an attractive material because its material quality factor is projected to be higher than that of silicon. The quality factors of silicon carbide high-overtone bulk acoustic resonators were measured over a range of temperatures, and the results are presented in this section.

B.1 Fabrication

High resistivity, 488μm-thick 4H-SiC wafers from Cree are used as the starting substrates. 400nm of low-stress silicon nitride is put down by LPCVD as an isolation layer. 200nm of platinum with 25nm titanium adhesion layer is then sputter deposited and patterned by liftoff as the bottom electrode. The bottom electrode is patterned to reduce C_0. 1.4μm of AlN was then sputter deposited and patterned by wet etch in TMAH. The top electrode of 200nm aluminum was then deposited by evaporation and patterned by liftoff. Figure B-1 shows the top view and cross-sections of the device. Transducers were designed to be circular, with different radii: 75μm, 100μm, and 250μm.

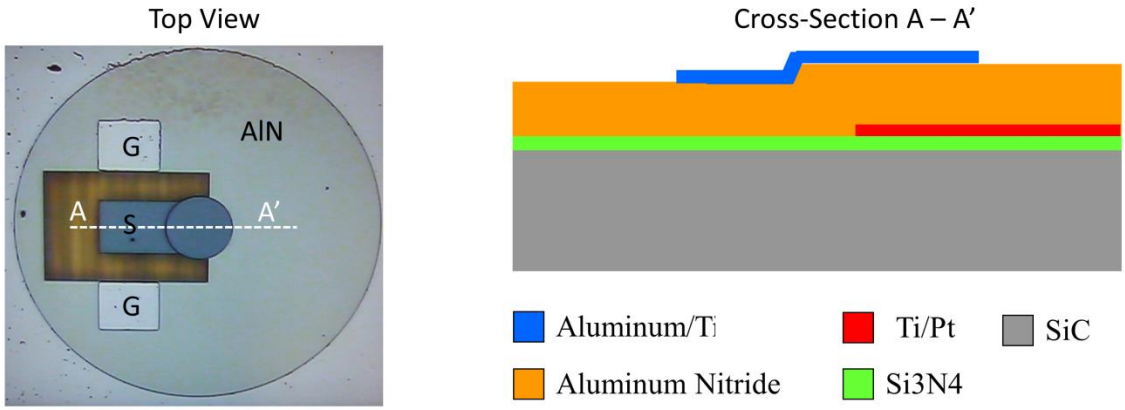

Figure B-1. Top view and cross-sectional view of AlN-transduced HBARs.

B.2 Measurements

Low temperature measurements were made in a Lakeshore cryogenic TTP4 probe station cooled with liquid nitrogen for a $75\mu m$ device (Figure B-2). For the same device, the Q was extracted for the 3.55GHz resonance by fitting the admittance curve to the BVD model (Figure B-3). The Q extraction was verified and fine-tuned by fitting the wide-band response on the Smith chart.

Measurements from room temperature to 400K were performed in a nitrogen atmosphere on a Cascade 11K Summit probe station with a temperature controlled chuck. Figure B-4 shows extracted Q versus temperature for the 1.92GHz resonance of a $100\mu m$-diameter device. The small jump in the trend from 35°C to 40°C was investigated at smaller temperature steps (Figure B-5). The small increase in Q from was not repeatable.

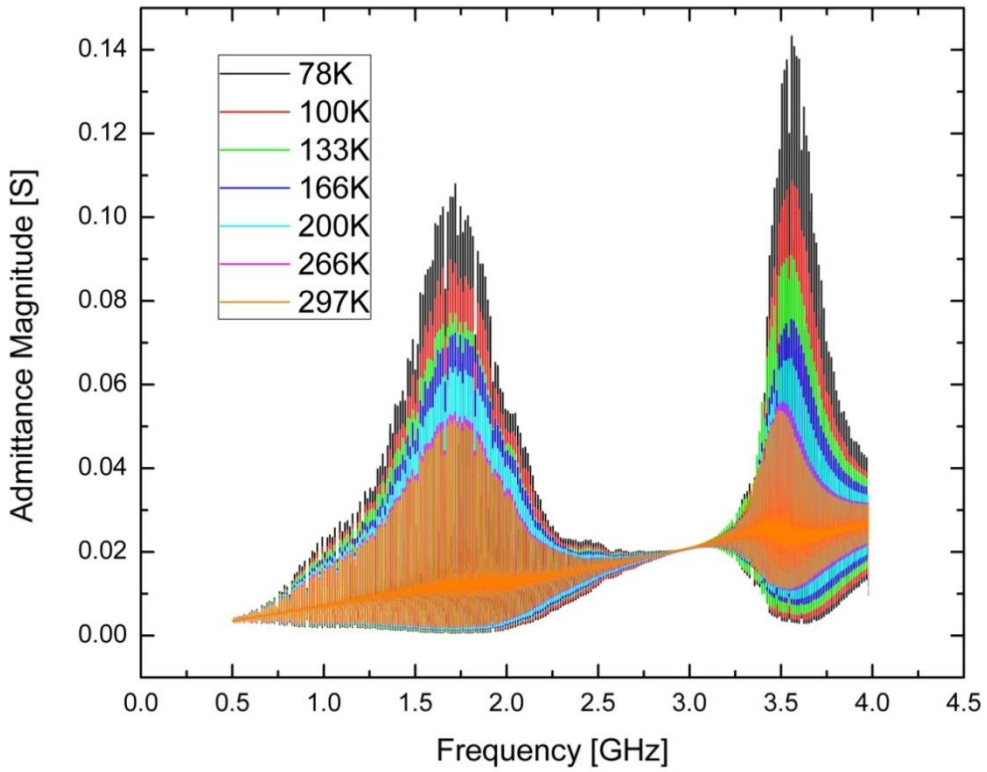

Figure B-2. Frequency response of a 1-port HBAR with a radius of of 75μm at various temperatures.

(a)

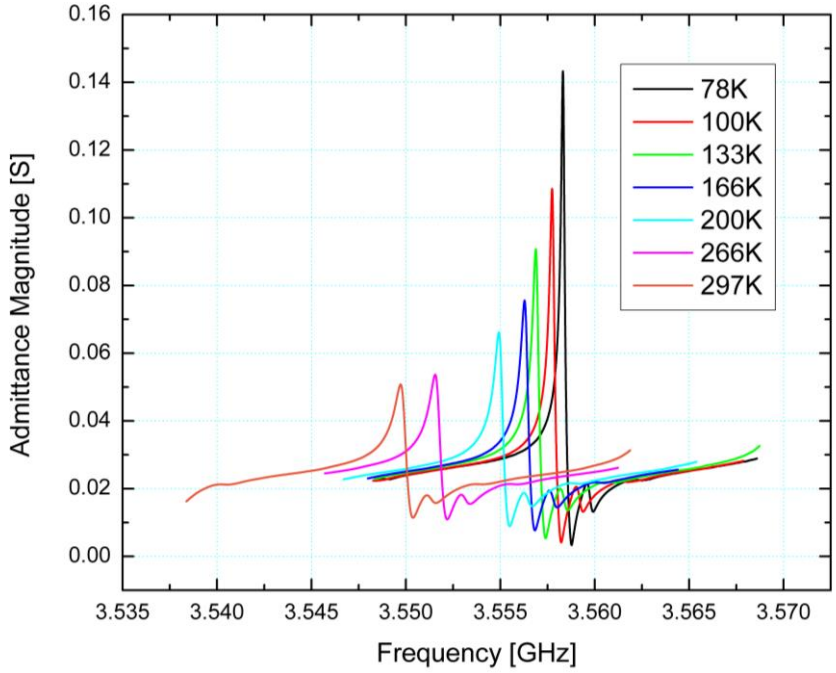

(b)

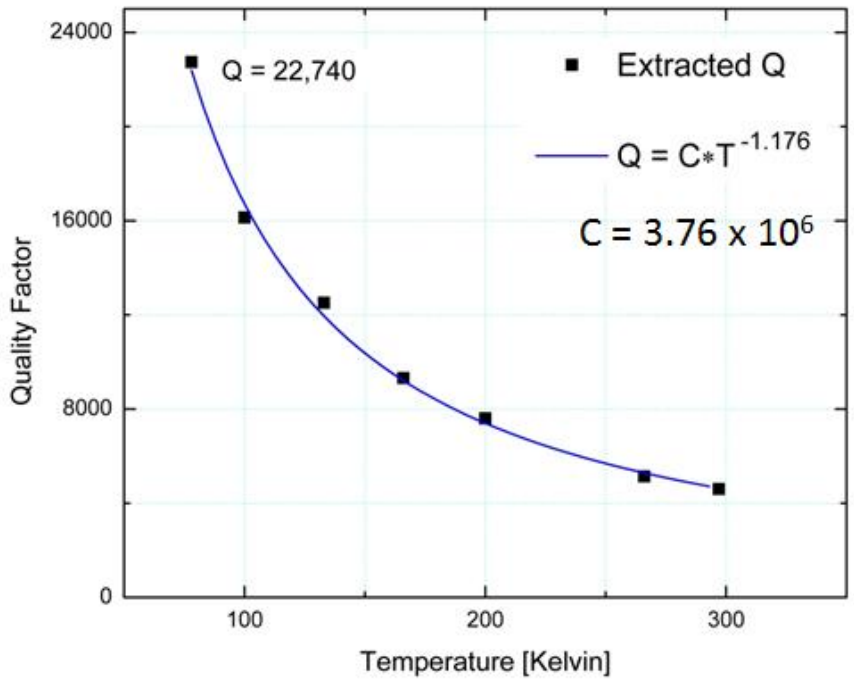

Figure B-3. Extracted Q versus temperature (b) for 3.55GHz resonance (a).

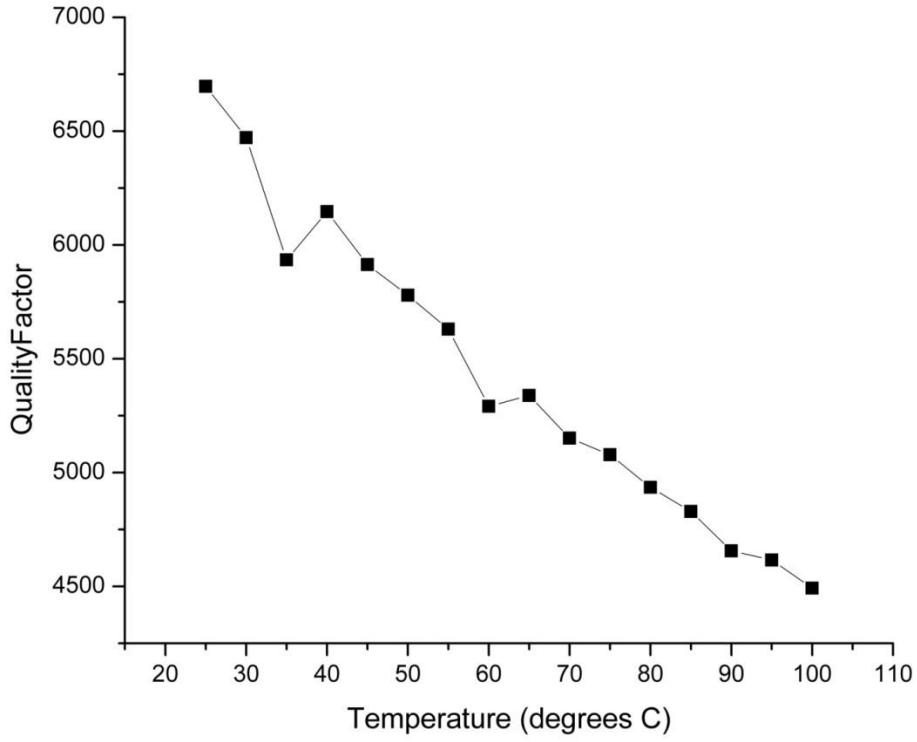

Figure B-4. Quality factor vs. temperature at 1.92GHz for a device with radius 100μm.

(a)

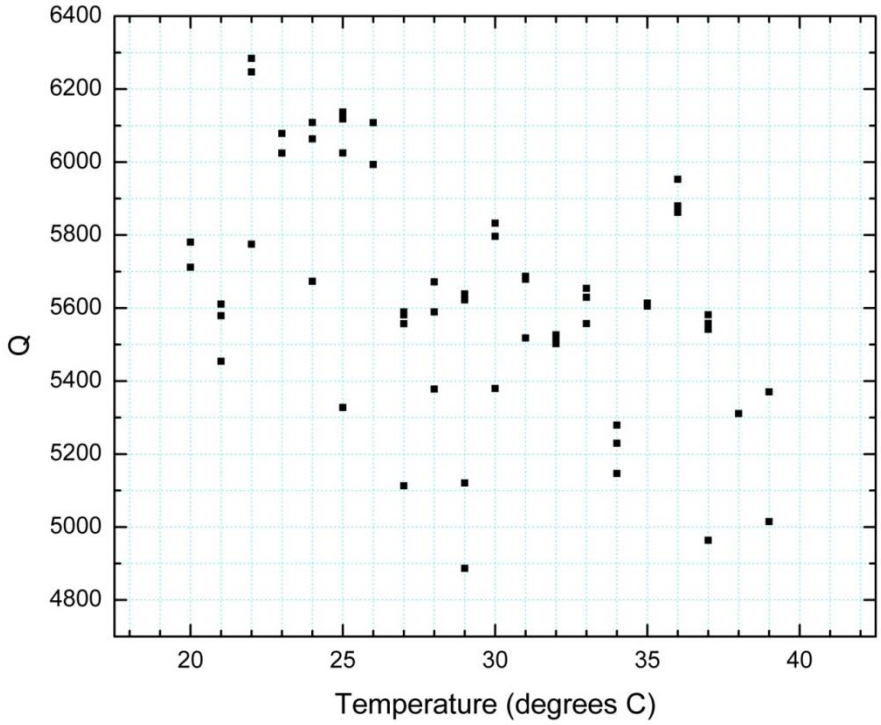

(b)

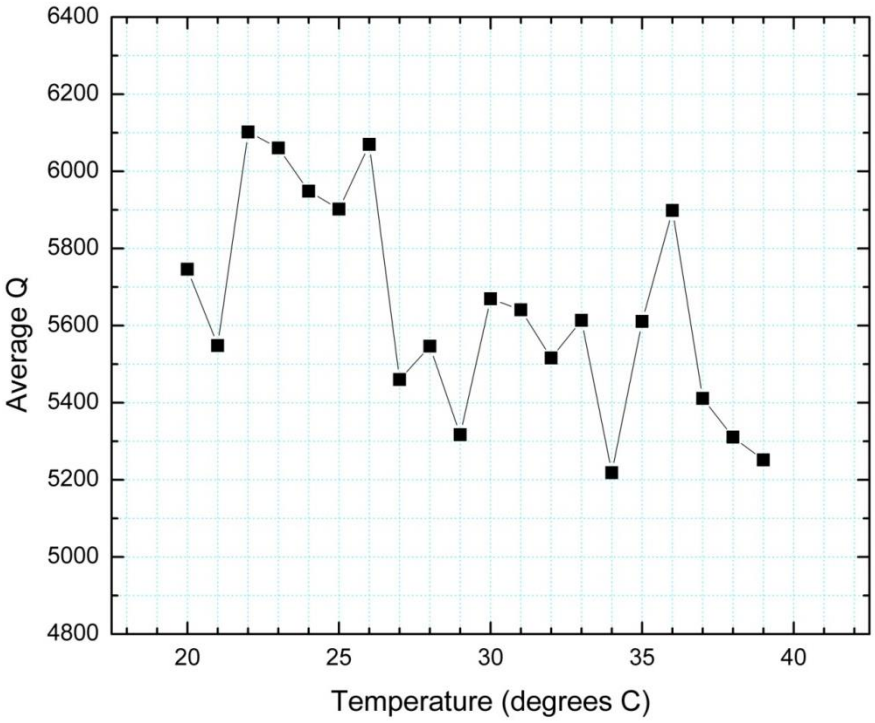

Figure B-5. Q vs temperature for the 1.22GHz resonance of a 100μm radius device. (a) shows all extracted data points and (b) shows the average Q at each temperature.

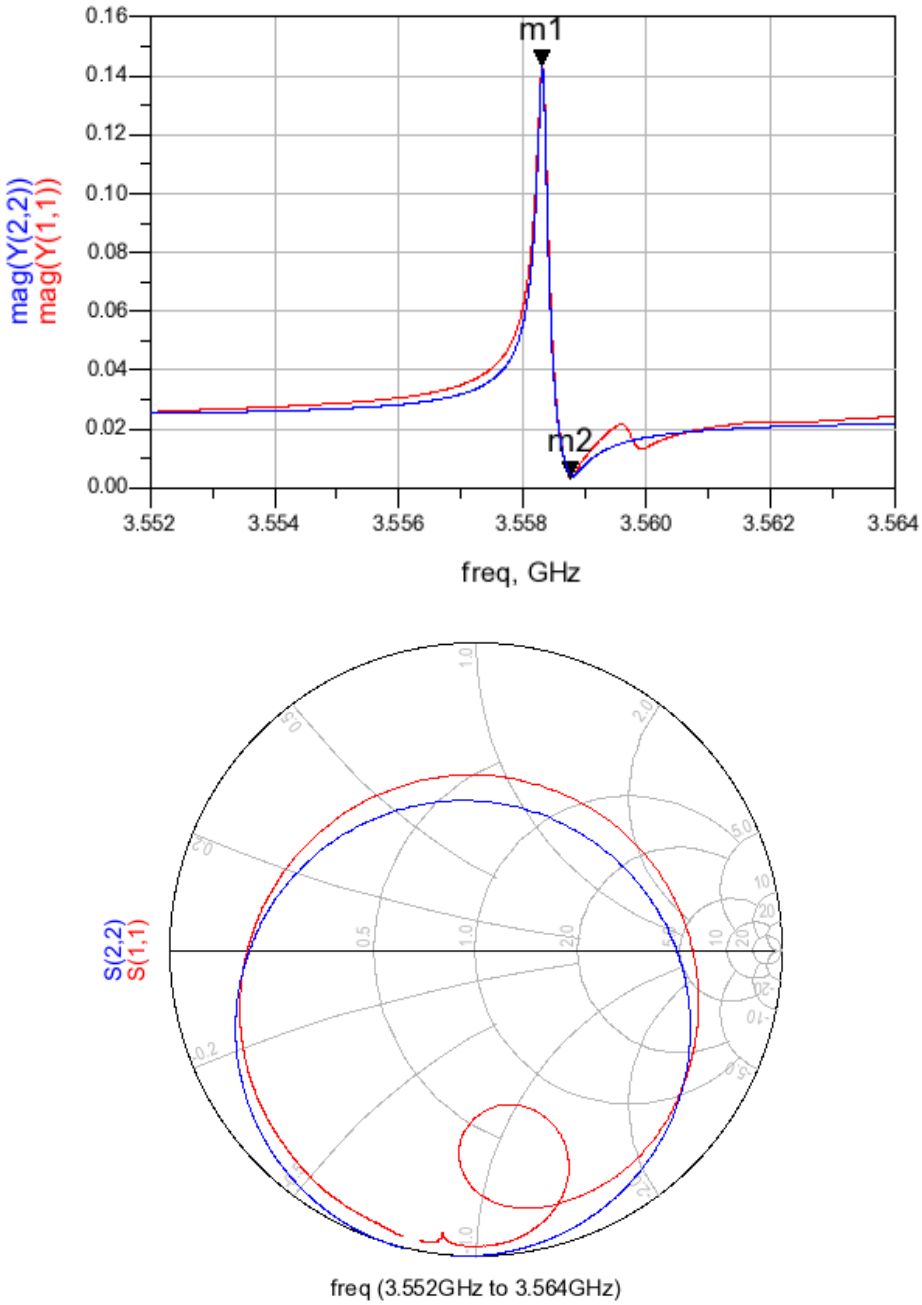

Figure B-6. Example fit of a resonance on the Smith chart. Advanced Design System (ADS) software was used to fit the curves.

APPENDIX C

PARTIAL GAP RESONATOR

This section presents a fabrication process to manufacture air-gap capacitively-transduced RF MEMS resonators. 2-port measurements show motional impedance (R_x) < 1.3kΩ and quality factor (Q) > 65,000 at 223MHz in vacuum. The fabrication process involves depositing a dual-layer spacer of 10nm of SiO_2 and 90nm of hafnia via atomic layer deposition (ALD) followed by oxide release. Nanometer air gaps are achieved, while the hafnia provides reliability against shorting of resonator and electrode. Consistent performance was achieved across multiple devices, demonstrating the robustness of the process.

C.1 Introduction

With exceptionally high quality factors, low power consumption, and CMOS compatibility, MEMS resonators provide an attractive solution to realizing fully integrated RF systems. It has recently been demonstrated that bulk resonators driven by internal dielectric transduction can achieve Q > 4,000 at 6.2GHz [18]. While the motional impedances of these devices scale favorably with frequency, the R_x versus frequency trend reported in [18] indicates impedances in excess of 200kΩ for frequencies below 1GHz. This impedance is prohibitively large for lower frequency applications, such as local oscillators used in telecommunications, which operate in the 1MHz to 1GHz frequency range. For sub-GHz applications, other methods of reducing motional impedance are necessary.

Piezoelectric resonators have achieved motional impedances as low as 24Ω at UHF, but the inherent loss of piezoelectrics limits the Q of the device to a few thousand [8]. Capacitively-driven resonators typically have much higher impedances that are on the order of a few kΩ [19][20][21]. However, capacitively-transduced silicon resonators have consistently achieved the highest Qs among MEMS resonators in the sub-GHz range. Furthermore, fabrication of these resonators involves CMOS compatible materials and micromachining techniques that can be

easily integrated into batch IC processes.

Several groups have experimented with increasing the electromechanical coupling factor η_e of capacitively driven air gap resonators by optimizing one or more of the parameters that determine η_e: transduction area, polarization voltage, and gap spacing g. Thick SiBARs with $600\mu m^2$ transduction areas have achieved an R_x of 680Ω at 85.9MHz with a Q of 22,400 in SOI [19]. There has been interest in reducing the gap in order to capitalize on the inverse relation between R_x and g^4. However, reliable fabrication of resonators transduced with thin air-gap capacitors is difficult not only because of fabrication limitations, but also because of increased risk of shorting.

Shorting can be prevented by inserting a dielectric between the resonator and electrode. Previously, devices have been made in which a high-κ dielectric was deposited into the gap of an already released structure [20][22], achieving 32nm air-gaps. However, those resonators exhibited a Q drop of >10× after hafnia coating due to losses introduced by the dielectric film on the resonator.

In contrast to the additive method of [20][22], our process utilizes a sacrificial spacer to create the air-gap, and is therefore not restricted by the starting gap of a released resonator. Hafnia is deposited only on the electrode side of the capacitive transducers, maintaining a pristine silicon resonator without any mass-loading or Q degradation. Furthermore, the process does not require an extra mask and lithography step to etch the dielectric from the bond-pads. Using this method, we fabricated resonators with transduction gaps consisting of 90nm hafnia and 10nm air, achieving R_x < 1.3kΩ and Q > 65,000 at VHF.

C.2 Theory

Figure C-1 shows the cross-section of a bar resonator driven by a capacitor composed of a dielectric layer and an air gap with permittivities of $\kappa\epsilon_0$ and ϵ_0, respectively. If $C_2 >> C_1$, the effective capacitance is roughly that of the air gap [20]. However, the C_1 of our devices is comparable to C_2 because the air gap is much narrower than the hafnia thickness, resulting in an

appreciable voltage drop across the hafnia. In our case, the 90nm hafnia (κ=27) layer drops 1/4 of the input voltage, meaning that the total capacitance is actually 3/4 of the 10nm air gap capacitance. Figure C-2 assesses the reduction in capacitive driving force with increasing hafnia thickness, assuming an air gap of 10nm. For comparison, the actuation force of a conventional air-gap transduced resonator is also shown. Starting from equal forces (point A), the force drop of the hafnia+air-gap resonator is much less dramatic compared to that of the air-gap device. Increasing the hafnia thickness to 90nm (point B) is far more favorable than increasing the air gap by the same amount (point C).

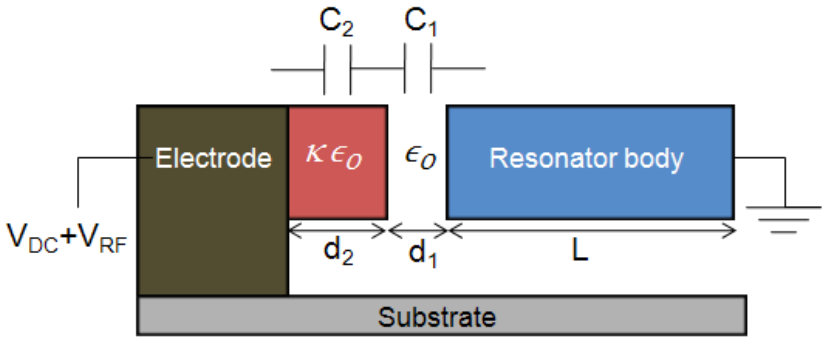

Figure C-1. Cross-sectional view of a bar resonator actuated through a dual-layer capacitor. ϵ_0 is the permittivity of free space. V_{DC} and V_{RF} are bias and RF input voltages, respectively.

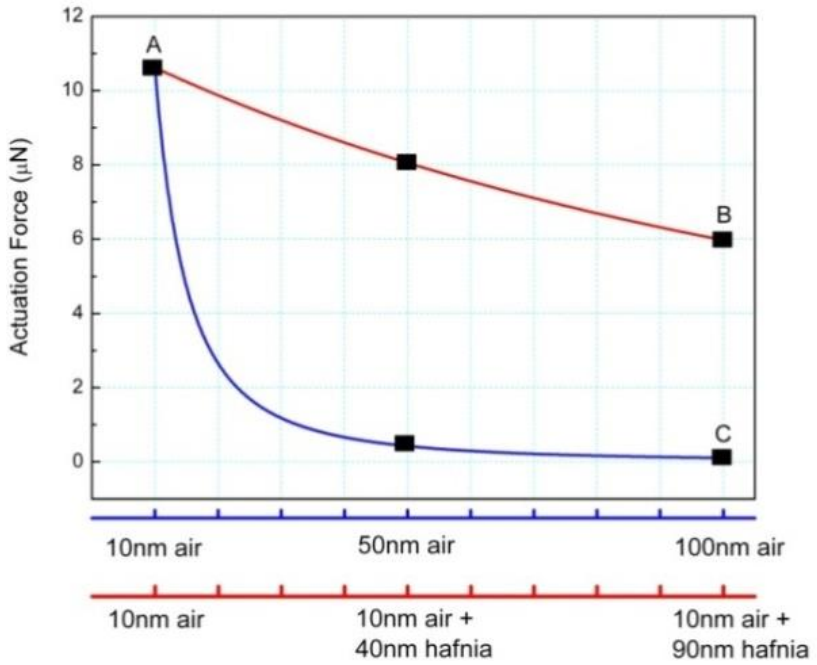

Figure C-2. Sinusoidal actuation force vs. gap thickness for a hafnia+air gap resonator and an air-gap resonator. The calculation assumes 15V DC, 100mV RF, and transduction area of $80\mu m^2$.

Equations C.1 to C.5 give ${\eta_e}^2$ and the equivalent circuit model for the resonator of Figure C-1 driven in bulk longitudinal mode at its resonant frequency $f = \frac{n}{2L}\sqrt{\frac{Y}{\rho}}$. A is the capacitor transduction area, n is the mode number, and Y and ρ are the Young's modulus and density of polysilicon, respectively.

$$ {\eta_e}^2 = \frac{A^2 {V_{DC}}^2 {\epsilon_0}^2 \kappa^4}{(d_2 + d_1\kappa)^4} \qquad \textit{Equation C.1} $$

$$ R_x = \frac{n\pi(d_2 + d_1\kappa)^4\sqrt{Y\rho}}{2AQ{V_{DC}}^2{\epsilon_0}^2\kappa^4} \qquad \textit{Equation C.2} $$

$$ C_x = \frac{2AL{V_{DC}}^2{\epsilon_0}^2\kappa^4}{n^2\pi^2 Y(d_2 + d_1\kappa)^4} \qquad \textit{Equation C.3} $$

$$L_x = \frac{L(d_2 + d_1\kappa)^4\rho}{2AV_{DC}{}^2\epsilon_0{}^2\kappa^4} \qquad \textit{Equation C.4}$$

$$C_0 = \frac{C_1 C_2}{C_1 + C_2} \qquad \textit{Equation C.5}$$

C.3 Fabrication

Fundamental mode bar resonators (Figure C-3) were fabricated using the process in Figures C-4 to C-5. Vertical polysilicon stubs placed at the displacement nodes anchor the body and bias the resonator. To create the dual layer capacitor, 10nm of SiO_2 and 90nm of hafnia were deposited in immediate succession in an Oxford ALD system. Figure C-7 is an SEM of a resonator fabricated in this process of length $18\mu m$, width $40\mu m$, and thickness $2\,\mu m$. An effective air gap of 10nm $\pm$ 2nm was calculated from impedance measurements (Agilent 4287 LCR meter) of 14 devices. Figure C-8a shows the transmission response of this device. For comparison to typical air-gap resonators and assessment of Q degradation, we then etch the hafnia (Figure C-6), opening a 100nm air-gap, and re-measure the same resonator (Figure C-8b).

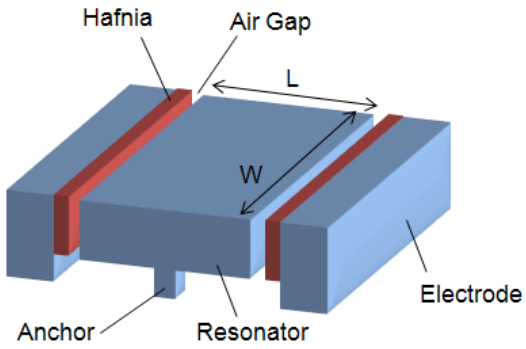

Figure C-3. Capacitively-transduced bar resonator with vertical anchors.

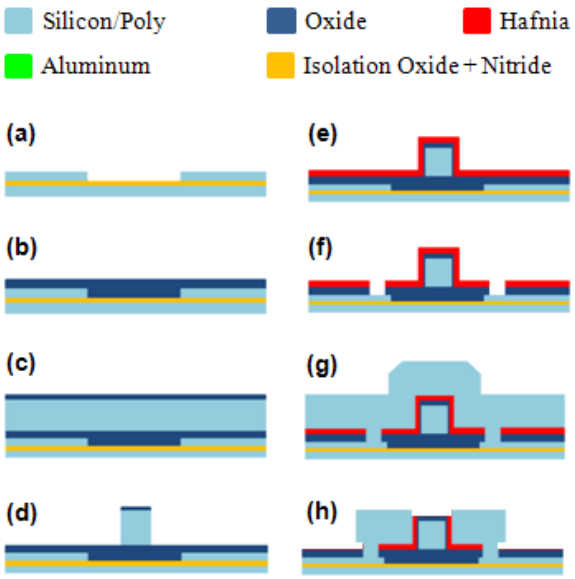

Figure C-4. Process flow for partial gap resonator. (a) Deposit and pattern poly-Si routing layer (b) Deposit sacrificial oxide (c) Deposit and pattern poly-Si and SiO_2 hard mask for dry etch (d) Dry etch poly-Si to define resonator body (e) ALD 10nm SiO_2 followed by 90nm of HfO_2 (f) Define anchors (g) Deposit poly-Si for electrodes (h) CMP and remove hafnia for metallization

Figure C-5. After C-4h and metallization, hafnia + air gap devices are vapor HF released to achieve 10nm air gap.

Figure C-6. An additional wet etch to remove hafnia after the step in Figure C-5 resulted in 100nm air gap devices.

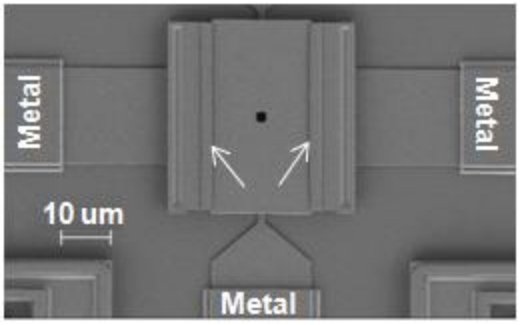

Figure C-7. SEM of a 222MHz resonator. Arrows indicate the 10nm air + 90nm hafnia gap. The gap was too small to be adequately imaged in SEM.

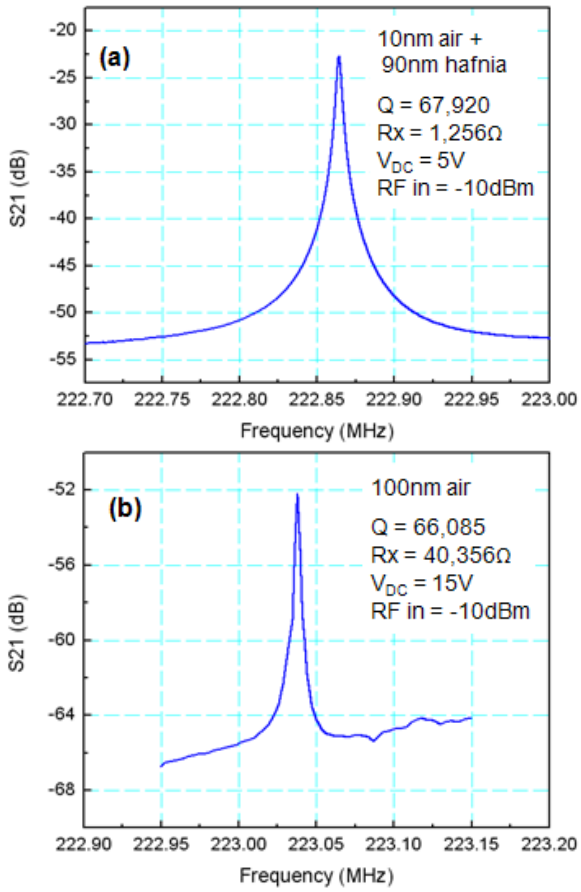

Figure C-8. The same resonator is actuated through a 10nm air + 90nm hafnia gap (a) and a 100nm air gap (b).

C.4 Results and Discussion

Standard 2-port measurements using an Agilent 8364B network analyzer were performed

on all devices in vacuum. R_x was extracted from S_{21} according to Equation C.6.

$$10^{S_{21,dB}/10} = \frac{(2Z_0)^2}{(2Z_0 + R_x)^2} \qquad \textit{Equation C. 6}$$

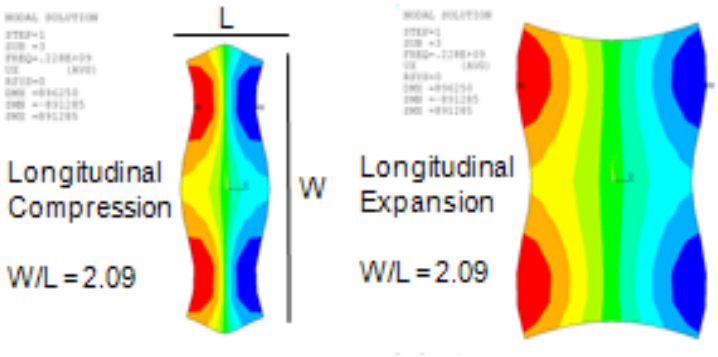

Figure C-9. Ansys simulation of the fundamental mode of a 18μm x 40μm x 2μm resonator shows distortion of the bar edges, which causes motional charge cancellation.

Comparison of device performance before and after hafnia removal shows that the device retained the original Q, while the R_x increased by 32×. This confirms that the 10nm sacrificial oxide spacer was cleanly removed without any residual mass-loading or damping effect on the resonator.

From Equation C.2, we expect a motional impedance of 90Ω for the device in Figure C-8a, which is far off from the measured $R_x$of 1,256Ω. The predicted R_x for the 100nm air gap device is 33.6kΩ. The discrepancy for the 100nm air gap device could easily be due to process variation – assuming a gap of 105nm gives a predicted R_x of 40.8kΩ. The series resistance should be very low because of metal routing, and therefore is an unlikely cause for the inconsistency between theoretical and measured impedances for the hafnia+air gap device. Ansys simulations of the device in Figure C-8a show that there is significant mode distortion of the bar edges (Figure C-9). There is a strong possibility that the large W/L aspect ratio of the resonators has caused mode-shape distortion, which can lead to charge cancellation and reduction in the electromechanical coupling efficiency [23]. Initial simulations suggest that mode distortion is

force dependent, which would explain why the 100nm air gap resonator performs as predicted, while the hafnia+air gap device does not.

Fourteen resonators selected from random locations on an 8-inch wafer display an extremely tight $f{\cdot}Q$ scatter matrix, demonstrating reliable manufacturability of these devices (Figure C-10). The process is also scalable to higher frequencies - Figure C-11 demonstrates a 523.3MHz resonator with Q of 19,563 and R_x of 3.82kΩ. Table C-1 summarizes the performance of our devices and that of 4 other low- impedance VHF resonators driven through air-gap capacitors. Our resonators compare very favorably in terms of both R_x and $f{\cdot}Q$.

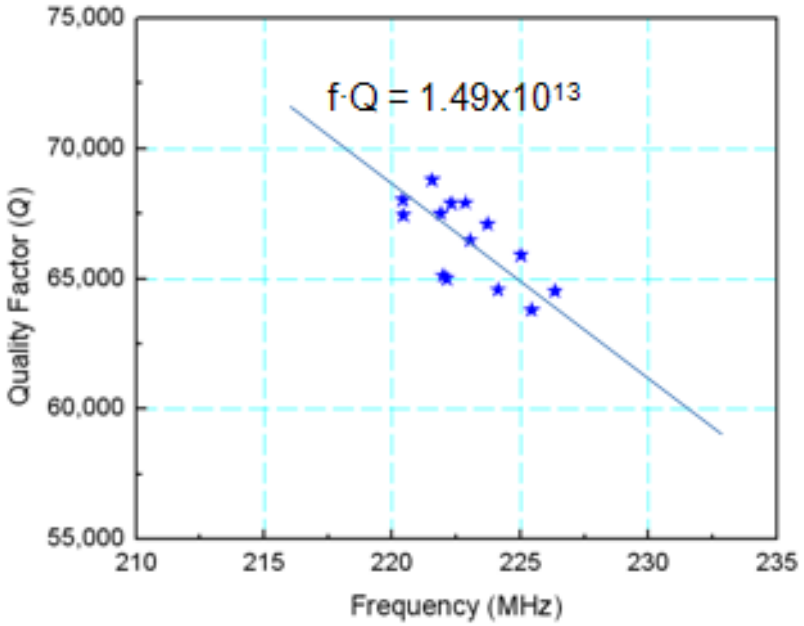

Figure C-10. The scatter data is of 14 devices from various dies on an 8-in. wafer. The data points tightly fit around $f{\cdot}Q = 1.49{\times}1013$.

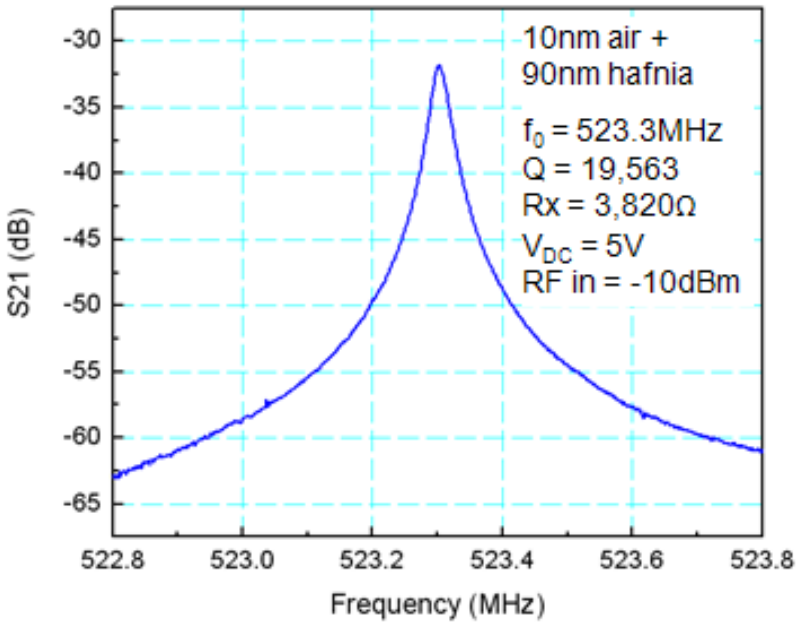

Figure C-11. 2-port capacitive measurement of a 523.3MHz resonator.

Table C-1. Performance Comparison of Partial Gap Resonator with Four Other Capacitively-Transduced Resonators (preference given to low-impedance).

Reference	Material	Rx (loaded) [Ω]	Frequency [MHz]	Q	f·Q
[19]	SCS	680	85.9	22,400	1.9×10^{12}
[24]	Poly-Si	11,300	61	161,000	9.8×10^{12}
[21]	SCS	10,000	5	103,000	5.7×10^{11}
[20]	Poly-Si	685	59.3	7,368	4.4×10^{11}
This work	Poly-Si	1,256	222.8	67,920	1.5×10^{13}

C.5 Conclusions

A fabrication process is presented that enables the manufacture of 10nm transduction gaps, while maintaining the intrinsic Q of the resonator. This is done by dual ALD deposition of 90nm hafnia and 10nm sacrificial SiO_2, which leaves hafnia only on the electrode. Our analysis shows that most of the voltage is dropped across the narrow air gap, resulting in large actuation forces and low R_x on the order of 1kΩ. In conclusion, our process provides a streamlined, reliable way of achieving high electromechanical coupling in capacitively-transduced high-Q silicon resonators targeting sub-GHz applications. The RF MEMS group at Sony Corporation is acknowledged for their help on this work.

BIBLIOGRAPHY

[1] K. P. Bloschock, A. R. Schofield, and T. W. Kenny, "Tip-based nanofabrication: an approach to true nanotechnology," in *Proc. SPIE 8031, Micro- and Nanotechnology Sensors, Systems, and Applications III*, 2011, pp. 803102–803102–10.

[2] Y. Wang and X. Chen, "Carbon nanotubes: A promising standard for quantitative evaluation of AFM tip apex geometry," *Ultramicroscopy*, vol. 107, no. 4–5, pp. 293–298, Apr. 2007.

[3] J. P. Spatz, S. S. Sheiko, and M. Möller, "Shape and quality control of modified scanning force microscopy tips," *Ultramicroscopy*, vol. 75, no. 1, pp. 1–4, Oct. 1998.

[4] Zyvex Labs, personal communication.

[5] K. Uozumi and K. Yamamuro, "A Possible Novel Scanning Ultrasonic Tip Microscope," *Jpn. J. Appl. Phys.*, vol. 28, no. Part 2, No. 7, pp. L1297–L1299, Jul. 1989.

[6] B. T. Khuri-Yakub, S. Akamine, B. Hadimioglu, H. Yamada, and C. F. Quate, "Near-field acoustic microscopy (Invited Paper)," in *Proc. SPIE, Scanning Probe Microscopy Instrumentation*, 1992, vol. 1556, pp. 30–39.

[7] J. N. Reddy, *An introduction to continuum mechanics: with applications*. New York: Cambridge University Press, 2008.

[8] G. Piazza, P. J. Stephanou, and A. P. Pisano, "One and two port piezoelectric higher order contour-mode MEMS resonators for mechanical signal processing," *Solid-State Electron.*, vol. 51, no. 11–12, pp. 1596–1608, Nov. 2007.

[9] K. F. Graff, *Wave motion in elastic solids*. New York: Dover Publications, 1991.

[10] M. Rinaldi, C. Zuniga, and G. Piazza, "5-10 GHz AlN Contour-Mode Nanoelectromechanical Resonators," 22nd IEEE International Conference on Micro Electro Mechanical Systems. (MEMS 2009). January 25-29, 2009, pp. 916–919.

[11] M. Rinaldi, C. Zuniga, C. Zuo, and G. Piazza, "AlN contour-mode resonators for narrow-band filters above 3 GHz," Frequency Control Symposium, 2009 Joint with the 22nd European Frequency and Time forum. IEEE International , vol., no., pp.70-74, 20-24 April 2009

[12] E. Hwang and S. A. Bhave, "PN-diode transduced 3.7-GHZ silicon resonator," 23rd IEEE International Conference on Micro Electro Mechanical Systems (MEMS 2010). January 24-28, 2010, pp. 208-211

[13] S. A. Chandorkar, M. Agarwal, R. Melamud, R. N. Candler, K. E. Goodson, and T. W. Kenny, "Limits of quality factor in bulk-mode micromechanical resonators," 21st IEEE International Conference on Micro Electro Mechanical Systems (MEMS 2008). January 13-17, 2008, pp.74-77

[14] R. Tabrizian, M. Rais-Zadeh, and F. Ayazi, "Effect of phonon interactions on limiting the f.Q product of micromechanical resonators," presented at the Solid-State Sensors, Actuators and Microsystems Conference, 2009. TRANSDUCERS 2009. International, 2009, pp. 2131–2134.

[15] M. Rinaldi, "Piezoelectric Aluminum Nitride Nano Plate Resonant Sensors for Next Generation Miniaturized Sensing Platforms," University of Pennsylvania, 2010.

[16] S. C. Minne, "Increasing the throughput of atomic force microscopy," Stanford University, 1996.

[17] C. Zuo, J. Van der Spiegel, and G. Piazza, "1.05 GHz MEMS oscillator based on lateral-field-excited piezoelectric AlN resonators," presented at the Frequency Control Symposium, 2009 Joint with the 22nd European Frequency and Time forum. IEEE International, 2009, pp. 381–384.

[18] D. Weinstein, S. A. Bhave, S. Morita, S. Mitarai, and K. Ikeda, "Frequency scaling and transducer efficiency in internal dielectrically transduced silicon bar resonators," presented at the Solid-State Sensors, Actuators and Microsystems Conference, 2009. TRANSDUCERS 2009. International, 2009, pp. 708–711.

[19] S. Pourkamali, G. K. Ho, and F. Ayazi, "Low-Impedance VHF and UHF Capacitive Silicon Bulk Acoustic-Wave Resonators Part II: Measurement and Characterization," *IEEE Trans. Electron Devices*, vol. 54, no. 8, pp. 2024–2030, Aug. 2007.

[20] L.-W. Hung, Z. A. Jacobson, Z. Ren, A. Javey, and Clark T-C. Nguyen, "Capacitive transducer strengthening via ALD-enabled partial-gap filling," presented at the Hilton Head Solid-State Sensors, Actuators and Microsystems Workshop, 2008, vol. 8, pp. 208–211.

[21] K. Sundaresan, G. K. Ho, S. Pourkamali, and F. Ayazi, "Electronically Temperature Compensated Silicon Bulk Acoustic Resonator Reference Oscillators," *IEEE J. Solid-State Circuits*, vol. 42, no. 6, pp. 1425–1434, Jun. 2007.

[22] M. Akgul, B. Kim, L.-W. Hung, Y. Lin, W.-C. Li, W.-L. Huang, I. Gurin, A. Borna, and C. T.-C. Nguyen, "Oscillator far-from-carrier phase noise reduction via nano-scale gap tuning of micromechanical resonators," presented at the Solid-State Sensors, Actuators and Microsystems Conference, 2009. TRANSDUCERS 2009. International, 2009, pp. 798–801.

[23] Siavash Pourkamali, "High frequency capacitive single crystal silicon resonators and coupled resonator systems," Georgia Institute of Technology, 2006.

[24] Yu-Wei Lin, Sheng-Shian Li, Zeying Ren, and C. T.-C. Nguyen, "Low phase noise array-composite micromechanical wine-glass disk oscillator," in *Electron Devices Meeting, 2005. IEDM Technical Digest. IEEE International*, 2005, pp. 278–281.